Max-Planck-Institut für Astrophysik

The Ignition of Thermonuclear Flames in Type Ia Supernovae

Luigi Iapichino

Vollständiger Abdruck der von der Fakultät für Physik der Technischen Universität München zur Erlangung des akademischen Grades eines

Doktors der Naturwissenschaften

genehmigten Dissertation.

Vorsitzender:	Univ.-Prof. Dr. O. Zimmer
Prüfer der Dissertation:	
	1. Hon.-Prof. Dr. W. Hillebrandt
	2. Univ.-Prof. Dr. W. Weise

Die Dissertation wurde am 15. 6. 2005 bei der Technischen Universität München eingereicht und durch die Fakultät für Physik am 21. 7. 2005 angenommen.

A Giovanna, compagna e sposa,
al dono della vita insieme,
al dono di una vita che cresce…

Contents

1. Introduction

1.1. Historical overview and classification

The history of the observation of supernovae (SNe, in the following), together with other transient phenomena in the sky (for example novae, comets, eclipses, meteors) is as old as mankind. The developments in such study, especially in ancient times, came together with, and sometimes were pushed by philosophical and scientific evolution of our conception of the Universe.

The naked eye observations of *stellae novae* were collected along the centuries, especially by Chinese sources: according to Mitton (1978), 75 events - local novae and supernovae, excluding comets - were recorded by Chinese astronomers between 532 B.C. and 1064 A.D. . Stephenson & Clark (1976) list seven galactic supernova events, recorded over a 1500-year interval (from 185 to 1604) in Chinese, Japanese, Arabic and European chronicles. In the Middle Age appeared, for example, the remarkable SN 1006, probably the brightest supernova ever observed in the historical age, with an estimated magnitude −9, and SN 1054, whose remnant is the well known Crab Nebula in Taurus.

Particularly important are the two galactic supernovae which occurred in the Modern Age: SN 1572, observed by Tycho Brahe and with a recent claim for identification of the companion star (Ruiz-Lapuente et al. 2004), and SN 1604 observed, among others, by Kepler in Prague and by Galileo in Padua. A case apart is represented by Cas A, the youngest known SN remnant in our Milky Way and the strongest extra-solar radio source in the sky (Baade & Minkowski 1954): calculating the expansion of the ejecta, it has been found that the supernova must have blown up around the year 1671 (Thorstensen et al. 2001), but the only observation of a new star in Cassiopeia in those years, made by Flamsteed in 1680, is still debated (Flamsteed himself did not recognized it as a “new star”; see also Stephenson & Green 2002).

Only two SNe have been discovered in other galaxies of the Local Group: SN 1987A[1], in the Large Magellanic Cloud, and SN 1885 (originally named S Andromedae, from the usual cataloguing system of variable stars), in the Andromeda Galaxy M31 (Hartwig 1885). This observation was then linked with the first evidence of the huge energy output of SN

[1] Zwicky et al. (1963) proposed the modern cataloguing system of supernovae, assigning a year corresponding to the time of their maximum light and one (e.g. 1987A, 1991T) or two letters (e.g. 1991bg, 2002bo), reflecting the order of discovery of that year.

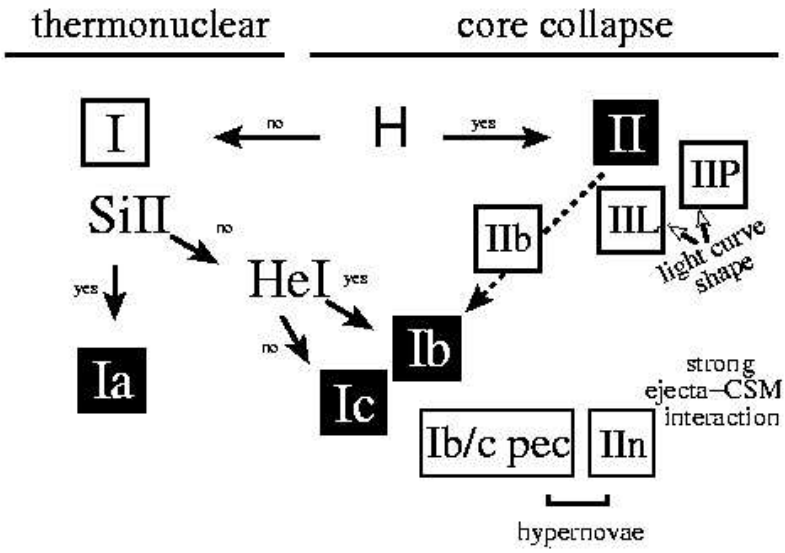

Figure 1.1.: Classification scheme for supernovae, from Turatto (2003). The objects in the classes Ib/c and IIN with explosion energies $E > 10^{52}$ erg are often called *hypernovae*.

explosions: Lundmark (1920) first estimated the distance of M31 to be about 7×10^5 light years, and it clearly showed that S And was about three orders of magnitude brighter than classical galactic novae. Further discoveries led Baade & Zwicky (1934) to distinguish between classical novae and a new class of objects, called by these authors for the first time *super-novae*.

Further, extensive searches were carried out by Zwicky in the following years (see e.g. Zwicky 1965), allowing a first understanding of these objects. Especially the spectral analysis, though limited, at that time, to the brightest supernovae (e.g. SN 1937C, Popper 1937), gave evidence of observational differences between various events.

The classification of SNe started with the aim of ordering different observational features; this approach entered the present-day astronomical usage although, as it is shown below, it is not straightforward in reflecting physical differences between different explosion mechanisms.

Minkowski (1940) introduced two main classes of supernovae, I and II, based on the presence of absence of Balmer lines of hydrogen in spectra at maximum light. In Type I another important feature is the absorption at 6150 Å, attributed to SiII, not present in the spectra of some peculiar objects. Zwicky (1965) later introduced the classes III, IV and V, neglected in the modern classification. Fig. 1.1 shows the current classification, also based mainly on the spectral features at maximum light. The "peculiar" objects in Type I are further divided into the subclasses Ib and Ic, and other subclasses are defined in Type II, based on the light curve shape (IIP, where "P" stands for a plateau in the light curve decline, and IIL, where "L" stands for a linear decrease of the luminosity) or on the overall shape

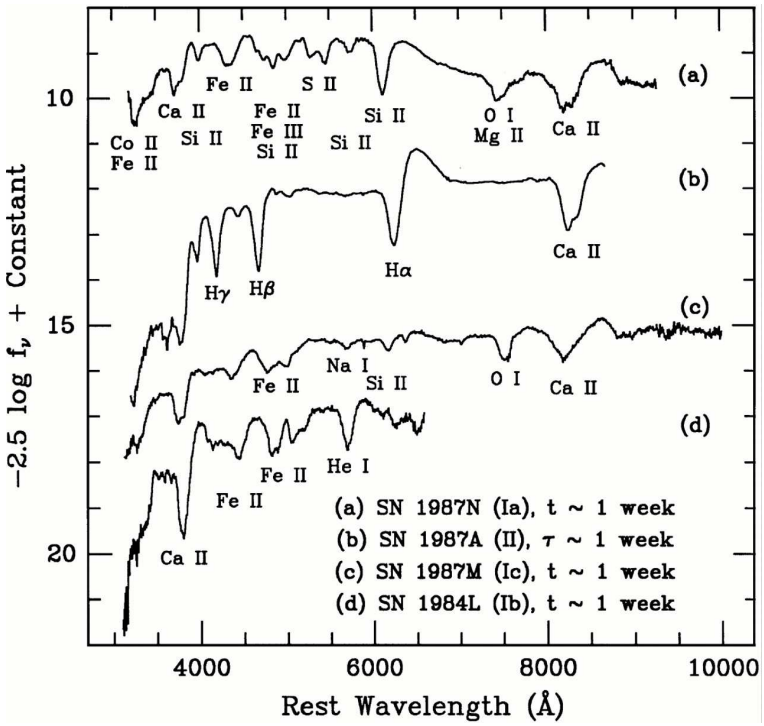

Figure 1.2.: Comparison of early time spectra of supernovae belonging to different types, from Filippenko (1997a). The most prominent features are clearly visible: SiII absorption with P Cygni profile, and no hydrogen, in **(a)**; H lines in **(b)**; no strong silicon absorption in **(c)** and **(d)**, but the He absorption distinguishing Type Ib from Ic.

---

of the absorption lines (IIn, where "n" means "narrow"). The class IIb is defined for few supernovae with early time spectra of type II and late time spectra similar to type Ib/c. In fig. 1.2 some spectra of supernovae of different types are compared.

1.2. Supernova types and physical differentiation

The physical interpretation of the observations started with the first hypotheses on the explosion mechanism: Zwicky (1938) suggested, as source for the explosion energy, the gravitational energy liberated by the collapse of an ordinary star that turns into a neutron star. It is remarkable that Zwicky introduced one of the basic ideas of stellar explosions (specifically, of core-collapse supernovae) only on the basis of about a dozen of observed SNe and, if seen from a modern point of view, with a very limited set of well-founded theoretical supports (for example, he wrote before the seminal work of Oppenheimer & Volkoff (1939) on neutron stars).

1.2.1. Core-collapse supernovae

Nowadays there is a general agreement that all the supernova types, with the exception of Type Ia, are the outcome of the evolution of massive ($M \gtrapprox 8\,M_\odot$) stars. The differences between type II and type Ib/c can be explained in terms of mass loss of the progenitor: SNe Ib do not show H lines because they have lost their envelope before exploding. The lack of He lines in SNe Ic is debated: it may be related to the deficiency of helium (due to the loss of the He layer) or to an insufficient mixing of radioactivity to excite energetic transitions in helium[2] (Woosley & Eastman 1997).

1.2.2. Type Ia supernovae

On the progenitors of Type Ia supernovae some constraints can be put, in very basic lines, from the following observational hints (Woosley 1990, Hillebrandt & Niemeyer 2000, Livio 2000):

1. the lack of hydrogen and helium lines in spectra;

2. the homogeneity: about 85% of the observed SNe Ia form an homogeneous class, as far as spectra, light curves and peak absolute magnitudes are concerned (see sect. 1.3.3);

3. different than core-collapse supernovae, SNe Ia may occur also in elliptical galaxies (e.g. Turatto et al. 1994); in spirals, they show some preference of association with young populations in spiral arms (Della Valle & Livio 1994), but also relatively old populations ($\tau \gtrapprox 4 \times 10^9$ years) can produce them.

From argument **3**, it follows that SNe Ia cannot be produced by progenitors which are more massive than about $8\,M_\odot$, otherwise they would show a clear correlation with spiral arms. An evolved progenitor, which has already lost its envelope, is then preferred also by argument **1**, that furthermore implies a small amount of circumstellar material; the lack of radio or X-ray observations of the progenitors rules out neutron stars and black holes, so the strongest candidates are the white dwarfs (WDs). On the other hand, in a WD an explosion cannot be triggered without accreting mass from a companion star, as it will be discussed in sect. 1.4.1.

From this very general analysis, whose details will be presented in the next sections, it turns out that the preferred candidate is a binary system, where at least one of the components is a white dwarf. Not only the progenitor, but also the explosion mechanism is different from core-collapse supernovae: the ignition of degenerate nuclear fuel was first explored by Hoyle & Fowler (1960) and the idea of thermonuclear explosion in WDs is

[2] The tail of the light curve of core-collapse supernovae is powered by the decay of ^{56}Ni; this energy source is crucial also for SNe Ia (cf. sect. 1.3.3).

now commonly accepted, in particular because it is potentially able to fulfill argument **2** (see sect. 1.4.1). In order to stress the difference of mechanisms, and to give a physically (and not observationally) based classification, SNe Ia are also called *thermonuclear supernovae*.

1.3. Observational features of thermonuclear supernovae

Before going deeper into the theoretical models of SNe Ia, in this section the most important observational features will be presented; these topics are more extensively reviewed by Filippenko (1997a) and by Leibundgut (2000).

1.3.1. Rates

It is very difficult to have good estimates of supernova rates: the relative rarity of SNe hinders the collection of statistically significant samples of data. Moreover, the correction of biases for different galaxy types, dust extinction and inclination of spirals is crucial for the results (Cappellaro et al. 1999). The unit of measurement for the supernova rate is normally defined as the number of supernovae per century, per B-band unit luminosity (that is, typically, in units of $10^{10}\,L_{B_\odot}$). Since the derivation of the luminosity of a galaxy depends on its distance, the rate depends in turn on the square of the Hubble constant H_0.

The local rate of type Ia supernovae is about 0.2 SN per century, per $10^{10}\,L_{B_\odot}$, with $H_0 = 75$ km s^{-1} Mpc^{-1} (Cappellaro et al. 1999). Other authors (e.g. van den Bergh 1990, Della Valle & Livio 1994) have normalized the results to the near-infrared H and K bands, which are better tracers of the stellar mass. Recent results for the SN rate per unit mass (Mannucci et al. 2005) say that the rate depends on galaxy type: it is higher in late type galaxies (spirals and irregulars) than in elliptical and S0.

1.3.2. Spectra

As already stated, the defining feature of SNe Ia is the deep, P-Cygni Si II line in the spectrum, due to the doublet at $\lambda\lambda$ 6347 and 6371 Å, with the blue-shifted absorption centered at about 6150 Å. The optical spectra at maximum light is dominated by lines of intermediate-mass elements (Si, O, Ca, Mg), neutral or singly ionized. The expansion velocities measured from these lines are up to a few times 10^9 cm s^{-1}. These absorptions are consistent with a structure of outer layers mainly composed by intermediate-mass elements (Filippenko 1997b).

About two weeks after the maximum light the spectrum is dominated by Fe II lines, which is indicative of an iron-rich core, where the photoshere begins to penetrate at that epoch. In the later ($\tau > 1$ month) nebular phase, emission lines of Fe and Co are observed.

UV spectra are available only for a few supernovae; in these wavelengths the flux is strongly blocked by a complex structure of overlapping P-Cygni profiles of Fe II and Co II lines (Pauldrach et al. 1996). Near IR spectra are relatively poor of significant details. No detection of γ-rays from SNe Ia has been achieved.

In contrast with several observations of core-collapse supernovae with polarized ejecta, no detectable polarization has been measured in SNe Ia, with the exceptions of SN 1996X (degree of polarization at about 0.2%, Wang et al. 1997), SN 1999bg (subluminous and somewhat peculiar event, Howell et al. 2001) and SN 2001el (Wang et al. 2003). This last work shows that an early discovery is crucial for these observations, because the polarization in SN 2001el is nearly undetectable a week after optical maximum. The detection of polarization can help to put constraints on the ejecta geometry and hence on progenitors and explosion mechanism (Kasen et al. 2003).

1.3.3. Luminosity and light curves

As far as photometry is concerned, SNe Ia show their most striking feature, the homogeneity, that permits to use them as standard candles for cosmological applications (see sect. 1.6).

The maximum light is reached in about 20 days (Riess et al. 1999); the best values of absolute magnitudes are derived for samples of local SNe Ia, whose distance is determined independently by Cepheids observations. According to Saha et al. (1999), the magnitude reached at maximum is $M_B \approx M_V \approx -19.5 \pm 0.1$. In the I-band, about two weeks after the first maximum, SNe Ia have a secondary peak (Leibundgut 1998). Apart from the exact value of the absolute magnitude, which is subject to some systematic differences in literature, it is noteworthy that the overall scatter is less than 0.5 magnitudes in the B and V-band (Gibson et al. 2000). Such scatter, though relatively small, in principle would hinder the use of SNe Ia as standard candles. Moreover, SNe Ia in early type galaxies are fainter ($\approx 0.2 - 0.3$ magn.) than events in spirals (Branch et al. 1996, and references therein). Despite of it, it is possible to reduce the overall scatter, thus standardizing the maximum luminosity of SNe Ia, by means of the well known empirical "Phillips relation" (Pskovskii 1977, Phillips 1993) between light curve decline and luminosity: less luminous supernovae have a faster declining light curve (see Branch 1998 also for other correlations between observables, which reduce the dispersion at less than 0.2 magn.).

About 85%, according to the definition of Branch et al. 1993, of all observed SNe Ia form a homogeneous (also called "Branch-normal") class in terms of spectra, light curves and peak luminosities; some objects show peculiarities. The prototype of overluminous events is SN 1991T, while SN 1991bg and SN 1992K are the best studied underluminous examples; see Leibundgut (2000) for their specific features.

Observations in different wavelengths can be used for deriving the bolometric luminosity of SNe Ia: typical values are around 10^{43} erg s^{-1}, but may vary from $\sim 2 \times 10^{42}$ erg s^{-1} for underluminous events to more than 2×10^{43} erg s^{-1} for SN 1991T (Contardo et al. 2000).

Both observational and theoretical hints suggest, as it was first pointed out by Truran et al. (1967) and Colgate & McKee (1969), that Type Ia supernovae are powered by the decay of

radioactive ^{56}Ni, produced by the explosion. ^{56}Ni decays to ^{56}Co through electron capture, with a half-life of 6.1 days. On turn, ^{56}Co is unstable and decays to the stable nucleus ^{56}Fe by electron capture (81%) or β^+ decay (19%), with a half-life of 77 days.

The amount of ^{56}Ni that is synthesized by the explosion can be derived from the bolometric luminosity applying the "Arnett's law" (Arnett 1982, Arnett et al. 1985), which states the equality between the energy injected by nuclear decay in the ejecta and the energy released on the surface at maximum light. This relation holds because the SN atmosphere is becoming optically thin at that time, but implies the symmetry of the ejecta, which seems a relatively reasonable hypothesis from polarization observations (see sect. 1.3.2). A typical SN Ia produces 0.6 $M_\odot$ of ^{56}Ni, with a range from 0.10 $M_\odot$ for SN 1991bg to 1.14 $M_\odot$ for SN 1991T (Contardo et al. 2000).

1.4. Progenitor models

In sect. 1.2.2, a first general background for the progenitor model has been extracted from the most basic facts; a successful detailed model of SNe Ia should also be able to accomplish finer requirements and constraints, arising from the listed observational features.

From the homogeneity of observed SNe, it turns out that the model has to be robust: its results do not have to depend strongly on the range of variation of the initial setup.

On the other hand, the model should account for the observed variability and the parameter correlations, possibly linking the observed relations with the variation of one or more physical parameters; also the dependence on the progenitor features has to be explored, in order to reproduce some observed trends (for example, the connection between luminosity and galaxy type; cf. sect. 1.3.3).

Another obvious requirement is the agreement with light curves and spectra, that implies constraints on the explosion energy, the amount of ^{56}Ni produced, the overall nucleosynthesis for the ejecta composition and the velocity of the expelled material.

For the sake of ease, it is possible to outline a scheme of a consistent theoretical model for SNe Ia in four fundamental parts:

- a progenitor model that provides hypothesis on the features and the evolution of the system, which is going to explode as a Type Ia supernova;
- an explosion model that describes the development of the explosion and its products;
- an ignition model that explains how the explosion is initiated and provides the initial conditions for the previous item, establishing the necessary link between progenitor evolution and explosion;
- any other theoretical tool which uses the quantities derived from the explosion model as input for subsequent studies.

The first two items will be addressed in this section (progenitor models) and in the next one (explosion models). The third item is the main topic of this work, and will be analyzed deeply in the next chapters. The fourth item will be briefly reviewed in sect. 1.7. For a broader discussion of the theory of SN Ia explosion see Hillebrandt & Niemeyer (2000). Progenitor models can be mainly grouped in two families: single-degenerate and double-degenerate scenarios.

1.4.1. Single-degenerate scenario

As discussed, in the progenitor binary system at least one of the two objects must be a white dwarf; in the single-degenerate scenario, it is assumed that the white dwarf accretes matter from a companion, which is non-degenerate.

It is known that WDs can be composed of He, of C and O, or of O, Ne and Mg (e.g. Livio 2000). In the first case, Iben & Tutukov (1985) find that the initial WD mass is smaller than $\sim 0.45 M_{\odot}$. With this composition, no scenario has been found consistent with the explosion of SN Ia: such system would explode during the accretion, at $M_{\rm WD} \sim 0.7 M_{\odot}$ (Nomoto & Sugimoto 1977), leaving ejecta composed only of He and ^{56}Ni, in contrast to the observed spectral signatures of intermediate-mass elements.

As far as O-Ne-Mg WDs are concerned, calculations show that they end more likely in an accretion-induced collapse to a neutron star rather than in a SN Ia explosion (Nomoto & Kondo 1991, Gutierrez et al. 1996). The only viable channel is therefore represented by carbon-oxygen (in the following, CO) WDs. There are two ways for leading to an explosion of CO WDs, discussed in the next two subsections.

Chandrasekhar-mass models

In this model, the WD accretes from the companion star (a Main Sequence star or a giant) until it approaches the Chandrasekhar mass, defined as the limiting mass for the degeneracy pressure to support the WD against gravitational force; $M_{\rm Ch} \simeq 5.8\,(Z/A)^2\ M_{\odot} \simeq 1.4 M_{\odot}$ for a CO WD. Carbon ignition occurs at, or very near the center (chapter 3) and the burning front incinerates the WD. Besides the specifics of the explosion models, which will be presented in sect. 1.5, the Chandrasekhar-mass scenario is considered the most promising in meeting the theoretical and observational constraints of, at least, the bulk of SNe Ia. Indeed, in this model, the CO WD explodes when its mass is close to the limiting Chandrasekhar mass, and this could explain the observed homogeneity. The main weakness of this model is to define the parameter space for a WD to accrete to $M_{\rm Ch}$ and, at the same time, to account for the observed SNe Ia rates.

The problem is discussed by Nomoto & Kondo (1991); fig. 1.3 shows, for different value of initial WD mass and accretion rate $\dot{M}$, the outcome of the evolution of the binary system. In a complementary approach one can study the parameter space of initial orbital period against secondary mass for different WD masses (Han & Podsiadlowski 2004); the birth rates for SNe Ia which are inferred from this work are lower than the observed ones, but

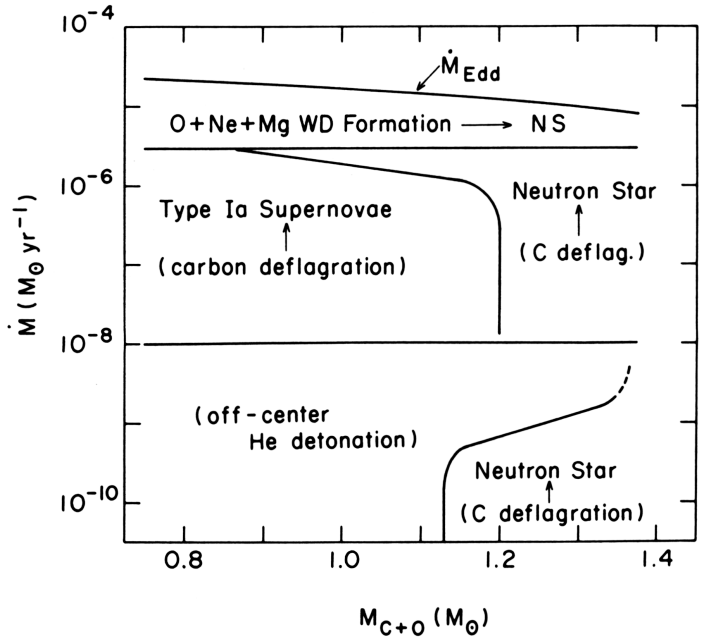

Figure 1.3.: Parameter study of the evolution of a single-degenerate binary system with an accreting CO WD, depending on the initial WD mass ($M_{\mathrm{C+O}}$) and on the accretion rate from the companion ($\dot{M}$). White dwarfs less massive than about $0.7 M_\odot$ cannot reach M_{Ch} before the companion star stops providing matter to accrete. From Nomoto & Kondo (1991).

still comparable. The physical problem with the accretion is to guarantee that the accreted hydrogen and helium burn steadily on the WD surface, without triggering a nova explosion (at $\dot{M} \lesssim 10^{-8}\ M_\odot\ \mathrm{yr}^{-1}$) or generating a common envelope (at $\dot{M} \gtrsim 10^{-6} - 10^{-5}\ M_\odot\ \mathrm{yr}^{-1}$). Encouraging results by Yoon et al. (2004) show recently that such conditions of helium burning can be more steady than previously supposed. Moreover, super-soft X-ray sources have been identified as accreting WD with steady H and He burning (Kahabka & van den Heuvel 1997, Hachisu & Kato 2003), corroborating the viability of this scenario.

Where not differently stated, the single-degenerate, Chandrasekhar-mass scenario will be assumed as the reference model in this thesis work.

Sub-Chandrasekhar-mass models

In this model the CO WD accretes a helium envelope ($0.1 - 0.3\, M_\odot$) on its surface, until a He detonation occurs there; the detonation propagates downwards and triggers the explosive carbon burning in the CO core, before the total WD mass has grown to M_{Ch} (Nomoto 1980, Woosley & Weaver 1994b, Livne & Arnett 1995, Höflich & Khokhlov 1996). Although this scenario has some appeal (statistically, it would better match the observed rates for SNe

Ia; Livio 2000), the spectral signatures of such explosions, especially the composition of high velocity ejecta (^{56}Ni and He, without intermediate-mass elements), strongly disfavor the model as explanation for "normal" SNe Ia. It has been claimed (Ruiz-Lapuente et al. 1997) that sub-Chandrasekhar-mass models might better represent the subluminous SNe Ia; the scenario has also been proposed, under certain conditions, as a viable alternative astrophysical site for the p-process nucleosynthesis (Goriely et al. 2002).

1.4.2. Double-degenerate scenario

The merging of two CO WDs is the endpoint of the evolution of a binary system, in which the two degenerate objects are bound to coalescence by emission of gravitational waves. If the sum of the masses is larger than $M_{\rm Ch}$, a possible outcome is the explosion as a SN Ia (Webbink 1984, Iben & Tutukov 1984). The existence of this evolutionary channel has been confirmed by the observations of double WD systems in the ESO SPY survey (Napiwotzki et al. 2004). 3D simulations of WD mergers (Benz et al. 1990, Rasio & Shapiro 1995) show that the less massive object is disrupted and its matter forms an accreting disk around the other WD.

Statistically, this model provides a good rate of events (Livio 2000); its main weakness is that the merger configuration does not trivially lead to a supernova explosion at $M \sim M_{\rm Ch}$, since an accretion-induced collapse is also predicted by Nomoto & Iben (1985) and Bravo & García-Senz (1999).

1.5. Explosion theory and modeling

In a thermonuclear supernova the explosion is triggered by explosive carbon burning. Due to the extreme density of the WD core, of the order of some 10^9 g cm^{-3} (Woosley 1990), the burning proceeds as a thermal runaway. Postponing the details of the ignition physics to chapter 3, in this section the main features of the explosion will be presented.

Because of the high sensitivity of the ^{12}C + ^{12}C reaction rate on temperature ($\propto T^{12}$ at $T \sim 10^{10}$ K, Hansen & Kawaler 1994) at the conditions of explosive C burning the burning length scale is microscopic (Niemeyer et al. 1996). There are two mechanisms for the propagation of these burning fronts (Landau & Lifshitz 1995):

- the front propagates by shock compression, at a sonic or supersonic speed: it is called a detonation.
- the front propagation is mediated by thermal conduction: this is a deflagration.

In principle, both modes are allowed in the supernova, and which mode is realized depends on details of the ignition process. From this point of view, there is no *a priori* reason for preferring one over the other of these mechanisms in the explosion models; again, the comparison with theoretical and observational constraints will help to make the choice.

1.5.1. Prompt detonation model

This model was proposed by Arnett (1969). Although it predicts the correct energy output for SNe Ia explosions, further analyses (Arnett et al. 1971) show that the nucleosynthesis of such a model is in contradiction with observations, because it would produce only iron-group elements and no intermediate-mass nuclei.

The problem is essentially related to burning timescales and densities. A detonation propagates in the WD at the speed of sound, thence the whole progenitor is burnt in a fraction of second. When the carbon is ignited explosively the burning proceeds to nuclear statistical equilibrium (NSE) and the composition of products depends, among other quantities, on density: above $\sim 10^8\,\mathrm{g\,cm^{-3}}$ the equilibrium moves towards iron-group elements, whereas at lower densities intermediate-mass elements are produced (see e.g. Nomoto et al. 1984). If the burning front starts propagating as a detonation, most of the nucleosynthesis occurs on a very short timescale, leaving no time for an expansion of the exploding WD. As a consequence, the burning occurs at too high density and the composition of the products is clearly inconsistent. It shows the failure of the prompt detonation model.

1.5.2. Pure deflagration model

A solution to the previous shortcoming is possible if the explosion starts as a subsonic deflagration, which propagates more slowly than a detonation, giving time to the unburnt material to expand to smaller density values.

In a fluid at rest, a deflagration propagates with the laminar velocity u_l, determined by the equilibrium of the timescales for nuclear burning $\tau_\mathrm{n} \approx e_\mathrm{int}/\dot{S}$ and for heat diffusion $\tau_\mathrm{d} \approx l_\mathrm{f}^2/D_\mathrm{th}$ (Landau & Lifshitz 1995):

$$u_\mathrm{l} \approx \frac{l_\mathrm{f}}{\tau_\mathrm{n}} \approx \left(\frac{D_\mathrm{th}\,\dot{S}}{e_\mathrm{int}}\right)^{1/2} \tag{1.1}$$

where e_int is the specific internal energy, $\dot{S}$ is the energy generation rate, l_f is the flame width and $D_\mathrm{th} = \kappa/(\rho\,C_\mathrm{p})$ is the thermal diffusion coefficient. Typical values for u_l in a WD are $\sim 0.001\,c_\mathrm{s}$, being c_s the sound speed: for a composition with $X(\mathrm{C}) = X(\mathrm{O}) = 0.5$, in the density range $10^9...10^7\,\mathrm{g\,cm^{-3}}$, $u_\mathrm{l} \sim 10^7...10^4\,\mathrm{cm\,s^{-1}}$, with $l_\mathrm{f} \sim 10^{-4}...1\,\mathrm{cm}$ (Timmes & Woosley 1992).

Such a flame velocity would be too low for giving, as result, a successful SN explosion: 1D calculations performed by keeping the front velocity as a parameter (Nomoto et al. 1984) show that the flame has to accelerate to velocities up to some relevant fraction of the sound speed in order to match results with observations. These large velocities are indeed reached by means of the flame interaction with turbulent motions in the WD matter: as it will be described in sect. 2.2.1, the velocity fluctuations wrinkle the flame. The flame propagation speed is increased to a value u_t, according to the intuitive formula (Damköhler 1939):

$$u_\mathrm{t} \approx u_\mathrm{l}\,\frac{A_\mathrm{t}}{A_\mathrm{l}} \tag{1.2}$$

where A_t and A_l are the turbulent and the laminar flame areas, respectively. A consistent determination of u_t makes use of a sub-grid scale model for turbulence; the details of the implementation are discussed elsewhere (e.g. Niemeyer & Hillebrandt 1995, Reinecke et al. 1999, 2002a).

After the 1D works on SNe Ia (Nomoto et al. 1976, Nomoto et al. 1984, Woosley & Weaver 1986, Woosley 1990), thanks to the increasing computational resources, 2D and 3D simulations have become available. An overview of these works and the related numerical techniques will be given in sect. 1.7; however, it is useful to list here the most valuable results of some of the latest 3D pure-deflagration models (Reinecke et al. 2002b, Gamezo et al. 2003, Röpke & Hillebrandt 2005b):

The outcome is a successful explosion, though the energetic output is rather on the weak side of the range observed for SNe Ia;

the derived maximum velocities of the ejecta are in the range of spectral observations ($1.0 - 1.5 \times 10^9$ cm s^{-1});

a possible shortcoming is the presence of unburned C and O at low velocity, albeit it cannot be completely ruled out by observations (Baron et al. 2003); see also sect. 3.5.

Beyond the different numerical implementations in works from different groups, it is particularly positive to have some convergence on the results, and some room for future technical improvements.

1.5.3. Delayed detonation model

In order to obtain a better agreement with observations, and in particular to solve the problem related to the last listed issue, it has been proposed (Khokhlov 1991b, Woosley & Weaver 1994a) that the flame, after starting as a deflagration, could have a transition to detonation (deflagration to detonation transition, or DDT). In this way, the preexpansion of the star occurs during the deflagration phase, avoiding the problems of pure detonation models, and the subsequent detonation phase leads to larger explosion energy, larger production of ^{56}Ni, and burning of the low-velocity unburned material with respect to pure deflagration models (Höflich & Khokhlov 1996, Gamezo et al. 2004). Also comparisons with nucleosynthesis (Iwamoto et al. 1999) and spectra and light curves (Höflich 2004) seem to be better.

Despite these advantages, the physical conditions for the transition to detonation are still unclear (Niemeyer 1999, Bell et al. 2004b) and the transition density for the DDT is accounted as a free tunable parameter in the simulations with a value of about 10^7 g cm^{-3} (Höflich & Khokhlov 1996). Moreover, the recent improvements in 3D deflagration models indicate, at least as a trend for the future, that a DDT could be an unnecessary ingredient for SN Ia models.

1.5.4. Pulsational delayed detonation and gravitationally confined detonation

These models have in common the failure of the first deflagration phase to unbind the WD and produce an explosion.

In the pulsational delayed detonation model, after a failed deflagration, the WD recollapses, triggering in this way a detonation (Nomoto et al. 1976, Khokhlov 1991a). In a recent version of this mechanism, García-Senz & Bravo (2005) propose the so-called pulsating reverse detonation. In their model an accretion shock is formed over the central region of the WD, mostly unburned, and could give rise to a detonation.

A somewhat similar mechanism is the gravitationally confined detonation, studied in 2D by Plewa et al. (2004). This model is based on the failed SN explosion simulated by Calder et al. (2004); as a follow-up of this calculation, the rise of the large, buoyant bubble to the surface of the WD focuses the material at the opposite side of the star, where the conditions for a subsequent detonation are reached. Further analysis are under study, in order to test the robustness of this model (Kasen & Plewa 2005).

It has to be noted that most of the latest simulations of the deflagration phase in SNe Ia (with the exceptions of Calder et al. 2004 and some models computed by García-Senz & Bravo 2005) end with a successful explosion, leaving no no need for these mechanisms.

1.6. Importance of Type Ia Supernovae in other fields of astrophysics

The interest in SNe Ia comes mostly from their noticeable feature of quasi-homogeneity. By means of the Phillips relation or similar empirical corrections one can use SNe Ia as "standardizable candles" in order to probe cosmological models. This is possible also because SNe Ia are the brightest standard candles available and are visible even at high redshift; an analogous use for SNe IIP (Baron et al. 2004) and gamma-ray bursts (Ghirlanda et al. 2004) is currently under study.

In the last years two groups (the High-z Supernova Search Team, Riess et al. 1998 and the Supernova Cosmology Project, Perlmutter et al. 1999), deriving the density parameters for matter and cosmological constant, Ω_M and Ω_Λ, have come to the conclusion that the universe is accelerating its expansion. These results are based on observations of distant SNe Ia ($0.1 \lesssim z \lesssim 1$); they are compatible with a flat cosmology with $\Omega_M \simeq 0.28$, $\Omega_\Lambda \simeq 0.72$, as it comes out also from an analysis of the cosmic microwave background data (Garnavich et al. 1998; fig. 1.4). More recently, there are several surveys (in progress or planned) aiming at the discovery of large numbers of low or high-z supernovae in order to use them for precision cosmology: a list of them is provided by Ruiz-Lapuente (2004).

The cosmological use of SNe Ia is based on the hypothesis of homogeneity of the local and distant samples of thermonuclear supernovae, which is none trivial (Leibundgut 2001). The evidence for the accelerating expansion of the universe is given by the fact that distant

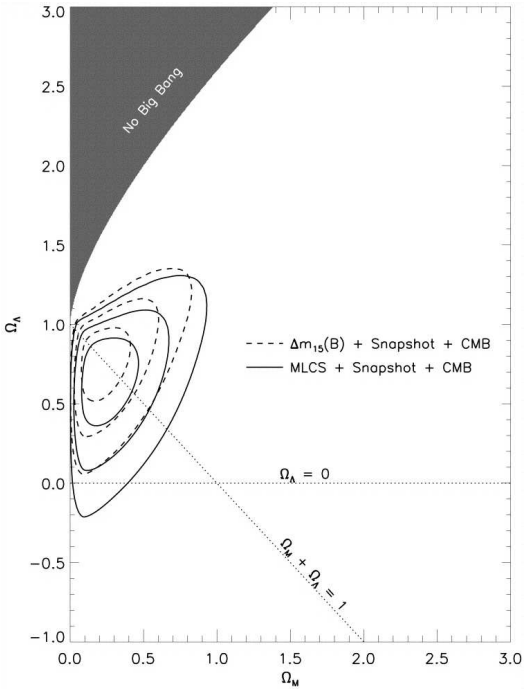

Figure 1.4.: Combined constraints on density parameters, from SNe Ia and the position of the first Doppler peak of the cosmic microwave background angular power spectrum (from Garnavich et al. 1998). The contours mark the 68%, 95.4% and 99.7% probability regions. The two different line styles refer to different techniques for data reduction.

SNe Ia appear about ≈ 0.20 mag. fainter than local SNe; it must be noted that this value is comparable to the scatter in peak luminosities of SNe Ia. Besides considerations on the extinction and the effect of gravitational lensing, especially interesting is the evaluation of possible intrinsic causes for the diversity of local and distant SNe Ia samples. For an effective use of SNe Ia in precision cosmology (for example, in studies about dark matter features) is then mandatory to reduce the systematic uncertainties on the theoretical side, refining the models and improving their predictive power.

Other reasons of interest involve the nucleosynthesis (they are the main source of iron-group elements), the role in galactic metal enrichment, and their contribution to the mass loss in early galactic evolution (see Leibundgut 2000 for an overview).

1.7. State of the art of SN Ia modeling and relevance of the present work

In the last decade, the availability of increasing computational resources has allowed the use of the presented theoretical framework for the development of multi-dimensional sim-

ulations of SN Ia explosions. Besides the open controversial issues on the theoretical side, the new tools themselves pose challenging demands to the researchers in order to take into account and implement into simulations the complex physics of the explosion.

One of the pivotal problems is the range of scales in SNe Ia physics: the relevant phenomena involve length scales from 10^{-4} cm (flame width) to 10^{7} cm (convective motions in the WD). Following directly all these scales is currently out of reach of the computational resources; one has to find a model for the physics on unresolved length scales, especially for the representation of the propagating flame surface (in large-scale simulations the flame is modeled as a discontinuity, neglecting its internal structure). Different approaches have been studied for it (see, for example, Livne 1993, Niemeyer & Hillebrandt 1995, Niemeyer et al. 1996). Currently, mostly two ways are used:

- The reaction-diffusion flame model, introduced by Khokhlov (1993) and used by Khokhlov (2000), Gamezo et al. (2003, 2004), Calder et al. (2004). In this scheme, the transition region between fuel and ashes is artificially smeared out over a number of cells, allowing the numerical resolution of the flame.

- The level-set method, introduced by Osher & Sethian (1988) and applied to the SN Ia problem by Reinecke et al. (1999), Reinecke et al. (1999) and used for example by Reinecke et al. (2002a,b), Röpke & Hillebrandt (2004, 2005b). In this scheme, a $(n-1)$-dimensional front is represented by the zero level set of a $n-$dimensional scalar function, providing the equations for its time evolution by passive advection (Sussman et al. 1994) and for tracking its normal propagation (Smiljanovski et al. 1997).

In both schemes, the velocity of the front is given by evaluating the turbulent flame speed (cf. sect. 1.5.2 and references therein), with some implementation of a sub-grid scale model.

The necessary pieces of information about microscopic processes which are involved in the large-scale simulations of SN explosion are provided by a number of small-scale investigations. The detailed description of such works is beyond the scope of this thesis; briefly, they are aimed for example to study flame instabilities (Röpke et al. 2004a,b, Bell et al. 2004a,b), turbulence modeling (Schmidt et al. 2004) and nuclear burning (Röpke & Hillebrandt 2005a).

As outlined in sect. 1.4, there is a wide family of theoretical tools, which use the explosion data as a starting point for their investigations. Light curve and spectra modeling is reviewed by Hillebrandt & Niemeyer (2000); one should note that a current effort is to provide multi-dimensional data from the explosion models as input for such calculations (Röpke 2005, Blinnikov & Sorokina 2004). The detailed nucleosynthesis of SNe Ia has been studied via post-processing techniques, taking 1D data as input (mostly from the explosion model of Nomoto et al. 1984), by for example Thielemann et al. (1986) and Iwamoto et al. (1999). Only recently, data from 2D and 3D hydrodynamical simulations have been used by Travaglio et al. (2004) and Kozma et al. (2005).

The main results of the most recent pure deflagration (sect. 1.5.2) and delayed detonation (sect. 1.5.3) SN Ia simulations have been outlined in this chapter. To end up, it is noteworthy to point out the general trend towards *parameter-free* calculations in which every ingredient has to be based on first physical principles, and not on tunable empirical parameters. For example, the cited well known phenomenological W7 model (Nomoto et al. 1984), though still useful as input for some one-dimensional calculations (as far as spectra, light curves and nucleosynthesis are concerned), has been followed by the already cited multi-dimensional simulations in which the burning speed is modeled on physical basis and not tuned in order to meet observational requirements.

Keeping in mind such trend, this thesis work is meant to inscribe the study of the initial conditions for SNe Ia simulations in the same framework. Sometimes cited as the last free parameter in SNe Ia models, the ignition process links the late stages of the progenitor evolution with the initial setup of explosion simulations. Actually, a large set of initial conditions has been used in simulations, with results ranging from mildly energetic (e.g. Reinecke et al. 2002b) to failed (Calder et al. 2004) explosions. Comparative studies of different initial flame shapes will be shown in sect. 3.5.

As it will be discussed in detail in chapter 3, the ignition process in SNe Ia is still a controversial issue. This work presents a new approach to this problem, based on 2D simulations performed using the FLASH code (Fryxell et al. 2000). The intention is to use these simulations to build an *ignition model* for SNe Ia (cf. sect. 1.4), a model able to answer the key questions:

- What is the initial flame shape in the WD, and what about the time evolution of the ignition process?
- What is the thermodynamic state of the WD core prior to runaway?
- Is there a range of feasible different ignition conditions and, if so, could it be able to explain (part of) the observed diversity of SNe Ia?
- Such ignition model should also obey to an important requirement, that is to guarantee the robustness of the explosion.

This thesis work is structured as follows: next chapter is devoted to the presentation of some theoretical tools, necessary for the further discussion. Chapter 3 is focused on the theory of SNe Ia ignition; chap. 4 describes the FLASH code, used for the simulations. The setup of the simulations is introduced in chap. 5, together with some preliminary tests. Finally, in chap. 6 the results are presented and discussed. Further numerical and technical issues are examined in appendix A.

2. Theoretical basics

2.1. Hydrodynamics

In order to describe the classical motion of a fluid, the basic equations of hydrodynamics are introduced here. The discussion will start from the simplest assumption, that is an ideal fluid. This leads to the Euler equations. In this section these assumptions will be then relaxed, discussing diffusive processes and source terms.

An underlying hypothesis in the following is the continuity assumption. It states that the fluid can be described as a continuum, considering its properties such as density, pressure, temperature and velocity as smoothly varying from one point to another. The length scales related to the physical problems of this work will be always much larger than the relevant mean free path. So the hypothesis holds.

2.1.1. The Euler equations

Ignoring dissipative effects (such as molecular diffusion, heat conduction or fluid viscosity), the dynamics of the fluid is governed by the Euler equations which express the conservation laws for mass, momentum and energy in the fluid.

Under the previous hypotheses, the conservation law of a generic extensive quantity $q(\mathbf{x}, t)$ over a volume V states that the rate of change of q equals its flux over the surface of V (let the source terms be ignored at this stage):

$$\int_V \frac{\partial q}{\partial t} dV = -\oint_{\partial V} q\mathbf{u}\, d\mathbf{A} \tag{2.1}$$

where $\mathbf{u}(\mathbf{x}, t)$ is the fluid velocity. This is the integral form of the conservation law of q. Using the divergence theorem, the last statement is equal to

$$\int_V \left(\frac{\partial q}{\partial t} + \nabla(q\mathbf{u}) \right) dV = 0 \tag{2.2}$$

Since it must hold for every choice of V, it is equivalent to

$$\frac{\partial q}{\partial t} + \nabla(q\mathbf{u}) = 0 \tag{2.3}$$

The last equation is the conservation law of q in differential form. One can write such relations for each conserved quantity of the hydrodynamical system.

In the non-relativistic case, mass and total energy are separately conserved; the conservation of mass, also known as the continuity equation, can be easily found with the same derivation as eq. (2.3):

$$\frac{\partial \rho}{\partial t} + \nabla(\rho \mathbf{u}) = 0 \tag{2.4}$$

where $\rho(\mathbf{x}, t)$ is the fluid density. Similarly, the conservation of momentum reads

$$\frac{\partial \rho \mathbf{u}}{\partial t} + \nabla(\rho \mathbf{u})\mathbf{u} + \nabla p = 0 \tag{2.5}$$

where p is the pressure. The conservation of energy is expressed by

$$\frac{\partial \rho e_{\text{tot}}}{\partial t} + \nabla(\rho e_{\text{tot}} \mathbf{u}) + \nabla(p\mathbf{u}) = 0 \tag{2.6}$$

where e_{tot} is the specific total energy. The set of the three previous equations is defined as *Euler equations*. Combining the equations (2.4) and (2.5) one finds the so-called Euler equation (not to be confused with the whole defined set)

$$\frac{\partial \mathbf{u}}{\partial t} + (\mathbf{u}\nabla)\mathbf{u} = -\frac{\nabla p}{\rho} \tag{2.7}$$

Note that these equations involve another quantity, the pressure p, which must be specified as a given function of density and specific internal energy $e_{\text{int}} = e_{\text{tot}} - \mathbf{u}^2/2$ and linked to the fluid temperature T. The additional relation is then provided by the equation of state (EOS)

$$p = p(\rho, e_{int}, \mathbf{X}); \qquad T = T(\rho, e_{int}, \mathbf{X}) \tag{2.8}$$

where $\mathbf{X}$ represents the fluid composition.

2.1.2. Dissipative effects and the Navier-Stokes equation

In the framework of SN Ia supernova explosions, in principle diffusive phenomena play an important role (for example, the flame propagation is based on heat diffusion). Several diffusive processes can be built into the Euler equations; the generic diffusion of a quantity X takes a form like

$$\frac{\partial X}{\partial t} = \nabla(D \nabla X) \tag{2.9}$$

where D is a diffusion coefficient.

If viscosity is taken into account, the momentum is the quantity that is diffused. It may be proved in this case (see e.g. Chorin & Marsden 1979) that the balance of momenta involves the divergence of the tensor σ, defined by

$$\sigma_{ij} = \mu\left(\frac{\partial u_i}{\partial x_j} + \frac{\partial u_j}{\partial x_i}\right) + \lambda\delta_{ij}(\nabla\mathbf{u}) \tag{2.10}$$

which can be rewritten grouping the traceless part in one term

$$\sigma_{ij} = \mu\left(\frac{\partial u_i}{\partial x_j} + \frac{\partial u_j}{\partial x_i} - \frac{2}{3}\delta_{ij}(\nabla\mathbf{u})\right) + \zeta\delta_{ij}(\nabla\mathbf{u}) \tag{2.11}$$

where μ and ζ are the coefficients of shear and bulk viscosity. With this expression of the tensor σ the Euler equation has to be rewritten accordingly, leading to the Navier-Stokes equation

$$\rho\left(\frac{\partial\mathbf{u}}{\partial t} + (\mathbf{u}\nabla)\mathbf{u}\right) = -\nabla p + \mu\nabla^2\mathbf{u} \tag{2.12}$$

This name is often used also for indicating the whole set of conservation laws: the eqs. (2.12), (2.4), that is not modified by the inclusion of viscosity, and (2.6), where a term of the form $\partial(u_b\sigma^{ab})/\partial x^a$ must be included to the right-hand side to take into account the energy flux due to internal friction.

Heat conduction is included adding to the right-hand side of the eq. (2.6) the term $\nabla(\kappa\nabla T)$, where κ is the thermal conductivity.

2.1.3. Source terms

The previous discussion is valid if no sources or sinks of the conserved quantities are present in the system. In the opposite case, the appropriate source terms must be included. LeVeque (1998) provides some examples of effects which can be described by such terms:

- Geometric source terms, which arise when a multi-dimensional problem is reduced to a lower number of dimensions, for example using cylindrical or spherical symmetry.
- External forces: here the analysis will be limited to gravity. In this case, if the gravitational force is only due to the mass density of the fluid (without external gravity fields), the potential ϕ is expressed by the Poisson equation

  $$\nabla^2\phi = 4\pi G\rho \tag{2.13}$$

  where G is the gravity constant. The gravity force modifies the equations (2.5) and (2.6), introducing respectively the terms $-\nabla\phi$ and $-\rho\mathbf{u}\nabla\phi$ at the right-hand sides.
- Reactive flows, which will be examined in the remaining part of this section.

Besides being described by its thermodynamical quantities a fluid is characterized by the composition (cf. eq. 2.8). The species i in the fluid is featured by the atomic number Z_i, the mass number A_i and the number density n_i. Its abundance is expressed by the mass fraction X_i, defined as

$$X_i = \frac{n_i A_i}{\sum_{i=1}^{N} n_i A_i} = \frac{n_i A_i}{\rho N_A} \tag{2.14}$$

where N_A is Avogadro's number and N is the number of species in the fluid. From the last formula arises the normalization condition for the mass fractions:

$$\sum_{i=1}^{N} X_i = 1 \tag{2.15}$$

The molar abundance of i is then defined as $Y_i = X_i/A_i$.

Because of nuclear reactions, the fluid composition changes with time. Following Arnett (1996), the rate of change of Y_i is

$$\frac{\partial Y_i}{\partial t} + \mathbf{u}(\nabla Y_i) = \dot{R}_i \tag{2.16}$$

where $\dot{R}_i$ is the total reaction rate of i, which takes into account every rate of nuclear reactions that produce or destroy the isotope i. The most general form for $\dot{R}_i$ is (Wagoner 1969)

$$\dot{R}_i = -\sum_j \left(\frac{Y_i^{N_i} Y_j^{N_j}}{N_i! N_j!} [ij] N_{i,j} \right) + \sum_{l,k} \left(\frac{Y_l^{N_l} Y_k^{N_k}}{N_l! N_k!} [lk] N_{i,lk} \right) \tag{2.17}$$

where the first term of the right-hand side accounts for the destruction of i, and the second for the production. In this formalism, $[ij]$ is the reaction rate for the generic reaction $i(j,\ldots)\ldots$ that destroys i; $[lk]$ is the rate for the generic reaction $l(k,i)\ldots$ that produces i; N_x, with $x = i, j, k$ or l is the stoichiometric coefficient, which indicates how many times the isotope x is involved in the considered reaction; $N_{i,j}$ and $N_{i,lk}$ are the values of N_i in the terms with sum index, respectively, j and l, k. This formalism can usefully describe different classes of reaction, such as β-decays, reactions with leptons or photons, two and three-body interactions, by using the appropriate form for the reaction rates .

A further term $-D_{\mathrm{sp}} \nabla Y_i$ can be added to the right-hand side of eq. (2.16) in order to take into account the microscopic species diffusion (where D_{sp} is the diffusion coefficient). This effect is negligible on macroscopic scales. Hence it will be not examined in the following.

Because of the nuclear reactions, an energy production term $\rho\dot{S}$ must be included at the right-hand side of eq. (2.6); $\dot{S}$ is the energy generation rate, defined by

$$\dot{S} = N_A \sum_{i=1}^{N} \dot{R}_i B_i \tag{2.18}$$

where B_i is the binding energy of the nucleus i. The specifics of the implementation will be shown in chapter 4.

2.2. Turbulence

Although a formal solution of the hydrodynamical equations for a viscous fluid (sect. 2.1.2) can in principle be found, there are physical situations in which the flow is unstable, i.e. any small perturbation can arbitrarily grow in time. The stability of a steady flow depends on the value of the dimensionless Reynolds number, defined by

$$Re(l) = \frac{l\,U(l)}{\nu} \tag{2.19}$$

where l is a characteristic length scale of the flow, $U(l)$ the characteristic velocity associated to this length scale, and $\nu = \mu/\rho$ is the kinematic viscosity. Experiments indicate the existence of critical value of Re, generally in the range $10 - 100$: flows with smaller Reynolds number are called laminar, while flows with $Re > Re_{\rm crit}$ show chaotic behaviors and are called turbulent.

The fluid equations introduced in the last section cannot describe quantitatively a turbulent flow; the energy balance of the fluid, together with some assumptions on the flow features, can help to characterize turbulence. The approach to the problem is described in many textbooks (e.g. Padmanabhan 2000).

Let the turbulent fluid velocities be considered homogeneous and isotropic: the flow can be idealized in terms of coexisting eddies of different sizes. The integral length scale L is defined as the length scale at which the turbulence is driven. Energy is injected in the system at this scale and is then transferred to eddies of smaller length scale. The rate ϵ of turbulent energy transfer for an eddie of length scale l, is given by

$$\epsilon \propto \left(U^2(l)\right)\left(\frac{U(l)}{l}\right) \sim \frac{U^3(l)}{l} \tag{2.20}$$

which can be understood as being composed of two parts, the first one proportional to the typical kinetic energy per unit mass carried by the eddies of size l, the second one playing the role of the inverse of the energy transfer timescale of the eddie. In the previous derivation is has been assumed that viscosity is negligible in dissipating turbulent energy to heat, which is valid at relatively large length scales. The length scale at which $Re \approx 1$ is called Kolmogorov scale $l_{\rm K}$. At $l \approx l_{\rm K}$ the flow is essentially laminar. The turbulent energy is hence dissipated by viscosity into heat at the length scales which are barely larger than $l_{\rm K}$. The scale range between L and $l_{\rm K}$ is called inertial range. Since the energy cannot be accumulated at any

length scale in the inertial range, ϵ must be constant in the range. Thence, the characteristic turbulent velocity $U(l)$ can be expressed as

$$U(l) \approx U(L) \left(\frac{l}{L}\right)^{1/3} \tag{2.21}$$

The energy spectrum $E(k)$, derived under the above listed hypotheses of homogeneity, isotropy and incompressibility, is called Kolmogorov spectrum. The expression for $E(k)$ is derived from the correlation function of the velocity $\mathbf{U}(\mathbf{x})$:

$$\xi(\mathbf{x}) = \langle \mathbf{U}(\mathbf{x} + \mathbf{y}) \cdot \mathbf{U}(\mathbf{y}) \rangle \tag{2.22}$$

The power spectrum $S(\mathbf{k})$, with $\mathbf{k} \simeq \mathbf{x}^{-1}$, is the Fourier transform of $\xi(\mathbf{x})$, and the power spectrum $E(k)$ is obtained by $S(\mathbf{k})$ ($S(k)$ in the isotropic case) by averaging over all the directions in the k-space. From a detailed dimensional analysis it results

$$E(k) = S(k)\, k^2 \propto \epsilon^{2/3}\, k^{-5/3} \tag{2.23}$$

2.2.1. The role of turbulence in the physics of SNe Ia

In the WD interior, at the conditions introduced in chapter 3, the estimated Reynolds number is about 10^{14} (Woosley et al. 2004), thus the fluid flow is turbulent; the related implications will be discussed in sect. 3.4.

Also in the context of the explosion physics (sect. 1.5.2) the importance of turbulence for flame acceleration has been cited; though the flame propagation is not a topic of this thesis work, this section will give a few ideas about the interaction of the flame front with the turbulent motion. In this concern it is helpful to define the Gibson scale l_g, defined as the length scale at which the characteristic turbulent velocity fluctuation is equal to the laminar flame velocity:

$$U(l_\mathrm{g}) = u_\mathrm{l} \tag{2.24}$$

For a deflagration propagating in matter at density $\rho > \rho_\mathrm{crit} \approx 10^7\,\mathrm{g\,cm^{-3}}$ it can be inferred that the flame width is smaller than the Gibson scale: the relation $l_\mathrm{f} < l_\mathrm{g}$ defines the so-called flamelet regime for turbulent burning (Peters 1999). In this regime, the turbulence wrinkles the flame on large scales (hence, the flame accelerates), but velocity fluctuations at scales $l < l_\mathrm{g}$ are smaller than u_l (cf. 2.21) and thus they are overwhelmed by the flame propagation velocity without disturbing the flame internal structure.

At matter densities $\rho \lesssim 10^7\,\mathrm{g\,cm^{-3}}$ it results $l_\mathrm{f} > l_\mathrm{g}$. The burning takes place in the distributed reaction regime, whose description goes beyond the scope of this work (see Bell et al. 2004b, Röpke & Hillebrandt 2005a).

2.3. Hydrodynamical instabilities

The previous discussion about turbulence is closely related to the features of fluid instabilities. These phenomena play an important role for the study of SNe Ia; in this section, the overview will be limited to the ideas which are significant in the context of the ignition theory. The study of the instabilities can be performed using a linear stability analysis. Assuming that the perturbations are small, the relevant equations are linearized in terms of the perturbed quantities. Then solutions of the form $\exp(\omega t + i\mathbf{kx})$ are tried, where $\mathbf{k}$ is the wavenumber and ω the growth rate of the perturbation. If in the dispersion relation between ω and $\mathbf{k}$ there is a real part for ω, the perturbation grows exponentially and the flow is unstable.

2.3.1. The Rayleigh-Taylor instability

(...) Imagine a ceiling of a room plastered uniformly with water to a depth of 1 meter. The layer of water will fall. However, it is not through lack of support from the air that the water will fall. The pressure of the atmosphere is equivalent to that of a column of water 10 meters thick, quite sufficient to hold the water against the ceiling. But in one respect the atmosphere fails as a supporting medium. It fails to constrain the air-water interface to flatness. No matter how carefully the water layer was prepared to begin with, it will deviate from planarity by some small amount (...). This example by Sharp (1984), so simple and, at the same time, so hard for the common sense, is particularly enlightening for the description of the Rayleigh-Taylor instability.

For the derivation of the properties of this instability in the simplest case (cf. Chandrasekhar 1961, Smith 2004), consider two inviscid, incompressible fluids in a region with a constant gravitational field $\mathbf{g}$ along the z axis, pointing downwards. In this case, with $\nabla\mathbf{u} = 0$ for an incompressible fluid from eq. (2.4), eqs. (2.4) and (2.5) can be written as

$$\frac{\partial\rho}{\partial t} + \mathbf{u}\nabla\rho = 0 \tag{2.25}$$

$$\rho\frac{\partial\mathbf{u}}{\partial t} = -\nabla p + \rho\mathbf{g} \tag{2.26}$$

with the gravitational acceleration $\mathbf{g} = -g\hat{\mathbf{z}}$. The fluids are supposed to be stratified, so $p = p(z)$ and $\rho = \rho(z)$. Moreover, before being perturbed, the system is assumed to be in static equilibrium, that is $\mathbf{u} = 0$. As a further hypothesis, the density is supposed to have the constant value ρ_1 for $z < 0$ and ρ_2 elsewhere, so that the xy plane is the equilibrium surface between the fluids with different densities. The calculations will be restricted for sake of ease to the plane xz, x and y being perfectly analogous.

A small perturbation is applied to pressure and density, so that

$$p \to p + \delta p; \qquad \rho \to \rho + \delta\rho \tag{2.27}$$

and $\mathbf{u} \neq 0$. This quantities are then substituted in the previous equation, keeping only the first-order perturbation terms and subtracting the equilibrium solutions. Then from eq. (2.25) one obtains

$$\frac{\partial(\delta\rho)}{\partial t} + \mathbf{u}\frac{\partial\rho}{\partial z} = 0 \tag{2.28}$$

and, from eq. (2.26),

$$\rho\frac{\partial u_x}{\partial t} = -\frac{\partial(\delta p)}{\partial x} \tag{2.29}$$

$$\rho\frac{\partial u_z}{\partial t} = -\frac{\partial(\delta p)}{\partial z} - g\delta\rho \tag{2.30}$$

for the x and z component respectively. In order to study stability, the explored solutions have the form

$$\mathbf{u} = \mathbf{u_0}\exp(ikx + \omega t) \tag{2.31}$$

$$\delta\rho = \delta\rho_0\exp(ikx + \omega t) \tag{2.32}$$

$$\delta p = \delta p_0\exp(ikx + \omega t)\ . \tag{2.33}$$

The substitution in equations (2.28)-(2.30), with some handling, leads to the general equation describing the evolution of the fluid after the perturbation and to the jump condition along the interface at $z = 0$:

$$\frac{\partial(\rho\partial u_z/\partial z)}{\partial z} = k^2 u_z\left(\rho - \frac{g}{\omega^2}\frac{\partial\rho}{\partial z}\right) \tag{2.34}$$

$$\rho_2\frac{\partial u_{2,z}}{\partial z} - \rho_1\frac{\partial u_{1,z}}{\partial z} = \frac{gk^2}{\omega^2}(\rho_2 u_{2,z} - \rho_1 u_{1,z})\ . \tag{2.35}$$

Recalling that ρ_1 and ρ_2 are constant and substituting again the z component of eq. (2.31), from eq. (2.34) one has

$$\frac{\partial^2 u_z}{\partial z^2} = k^2\frac{\partial u_z}{\partial z} \tag{2.36}$$

which accepts as solution

$$u_z = Ae^{kz} + Be^{-kz}\ . \tag{2.37}$$

Requiring $u_z = 0$ at infinity and the continuity at $z = 0$, the previous formula reads

$$\begin{aligned} u_{1,z} &= Ae^{kz} \quad \text{for} \quad z < 0 \\ u_{2,z} &= Ae^{-kz} \quad \text{for} \quad z > 0\ . \end{aligned} \tag{2.38}$$

Putting it in eq. (2.35), one finally finds

$$-k\rho_2 - k\rho_1 = -\frac{gk^2}{\omega^2}(\rho_2 - \rho_1) \tag{2.39}$$

which, rearranged, leads to

$$\omega^2 = \frac{gk(\rho_2 - \rho_1)}{(\rho_2 + \rho_1)} \,. \tag{2.40}$$

Recalling eqs. (2.31)-(2.33), the condition for the equilibrium to be stable is $\omega^2 < 0$. It turns out that for $\rho_2 > \rho_1$, like in the example shown at the beginning of this section, the equilibrium is unstable. The heavier fluid cannot reside on top of the lighter one. The Rayleigh-Taylor instability is a buoyancy effect: in general, it arises whenever $\partial\rho/\partial z > 0$ in presence of gravity acting downwards. Concerning the theory of SN Ia explosion, the Rayleigh-Taylor instability plays an important role, acting on the lighter ashes and folding the flame during its propagation (e.g. Reinecke et al. 1999, 2002b, Gamezo et al. 2003, Röpke & Hillebrandt 2005b). In this work the importance of this instability (and of the Kelvin-Helmholtz instability, presented in the next section) in the framework of the ignition theory will be rather emphasized and discussed in more detail in sect. 6.3.3.

2.3.2. The Kelvin-Helmholtz instability

This instability occurs, like the Rayleigh-Taylor instability, because of the presence of fluids of different density. Different than in the previous case, however, it does not need the action of a gravitational field, but it arises whenever there is a velocity gradient in the flow along the direction of separation of the two fluids. Following Padmanabhan (2000), one can apply a derivation similar to the last section, looking for perturbed solutions of the form $\exp(ikx - \omega t)$. In this case, the dispersion relation between ω and k reads

$$\omega = ku\frac{i\rho_1 \pm \sqrt{\rho_1\rho_2}}{\rho_1 + \rho_2} \,, \tag{2.41}$$

where v is the relative velocity of the two fluids: ω has always a real part, hence the perturbations may grow, in this idealized case, for every value of the wavenumber k. This instability shows itself at the sides of structures which are unstable to the Rayleigh-Taylor instability (cf. sect. 6.3.3).

2.4. General issues of convection theory

In this section, some key facts about convection are presented; the topic will be reprised in the context of the physical conditions in the WD core in chapter 3.

2.4.1. Hydrostatic equilibrium

Let the following situation be taken under consideration. A self-gravitating and non-rotating system, spherically symmetric, with values of ρ and p locally depending only on the radial coordinate r. The system is defined to be in hydrostatic equilibrium when $\mathbf{u} = 0$. In this case, the equation of momentum conservation (2.5) expresses the requirement:

$$\frac{dp(r)}{dr} = -g(r)\rho(r) = -\frac{GM(r)}{r^2}\rho(r) \,, \tag{2.42}$$

where $M(r)$ is the mass enclosed in a sphere of radius r.

2.4.2. The Schwarzschild criterion for convection

It has to be noted that in the previous derivation no hypothesis on the thermal equilibrium was given. It is well known from the basics of stellar structure (cf. Kippenhahn & Weigert 1994) that a fluid can be in hydrostatic equilibrium without being in thermal equilibrium. For example, this is the case in those stellar interiors, where the energy is transported by radiation. It may be explored under which conditions this mechanical equilibrium is conserved by means of the following thought experiment (Wilson & Mayle 1988).

Consider a blob of matter in a fluid. The gravitational force is pointing downwards. The blob is then displaced adiabatically from its initial position upwards a distance λ in pressure equilibrium with the surrounding fluid. If the blob in its new position is less dense than the surrounding material, it will move further upward by buoyancy. The region is then defined to be convectively unstable.

Define p and S as the pressure and entropy at the initial position of the bubble, and p' and S' in the position where it is displaced. Then the condition for convective instability is expressed by

$$\rho(p', S') - \rho(p', S) \geq 0 \,. \tag{2.43}$$

Expanding the previous formula in a Taylor series,

$$\rho(p', S') - \rho(p', S) = \left.\frac{\partial\rho}{\partial S}\right|_p \lambda\frac{dS}{dr} \geq 0 \,, \tag{2.44}$$

in which the derivative can be written, according to Landau & Lifshitz (1995), as

$$\left.\frac{\partial\rho}{\partial S}\right|_p = \frac{T}{C_p}\left.\frac{\partial\rho}{\partial T}\right|_p \,, \tag{2.45}$$

where C_p is the specific heat at constant pressure. Since for most equations of state one has $\partial\rho/\partial T|_p \leq 0$, the Schwarzschild criterion for the presence of convective instability is expressed simply by

$$\frac{dS}{dr} \leq 0 \,. \tag{2.46}$$

A region with a negative entropy gradient is then convectively unstable by the Schwarzschild criterion. In this derivation, no composition change has been assumed. The role of composition is taken into account by the Ledoux criterion, which will not be discussed here.

2.4.3. The mixing-length theory

A useful, albeit oversimplified, convection model is the mixing-length theory. The theoretical application limits of this theory in the progenitor evolution will be outlined in sect. 3.3. Nevertheless, even in that framework it is profitably used for some estimates (Woosley et al. 2004).

The mixing-length theory, reviewed in many textbooks, is a one-dimensional approach for convection. It models the convective energy flux assuming that a rising blob in the convective zone travels over a distance l before releasing the heat to the surrounding matter. This "mixing length" is defined as $l = \alpha H_\mathrm{p}$, where α is a numerical parameter and H_p is the pressure scale height,

$$H_\mathrm{p} = -\left(\frac{\partial \ln p}{\partial r}\right)^{-1} . \tag{2.47}$$

The convective heat flux transferred from the blob to the surroundings is (Clayton 1983)

$$F_c = \overline{v}_\mathrm{c}\, \rho\, C_p\, l\, \Delta\nabla T , \tag{2.48}$$

where $\overline{v}_\mathrm{c}$ is the average blob velocity and $\Delta\nabla T$ is defined by

$$\Delta T = l\, \Delta\nabla T = \left(\left|\frac{dT}{dr}\right| - \left|\frac{dT}{dr}\right|_{ad}\right) l . \tag{2.49}$$

$\left(\frac{dT}{dr}\right)_{ad}$ is the thermal gradient of the blob in the adiabatic rise, and $\frac{dT}{dr}$ is the thermal gradient of the surrounding fluid. The velocity $\overline{v}_\mathrm{c}$ can be calculated by equating the average kinetic energy of the blob with the work done along the distance l by the buoyancy force acting on the blob. The average buoyant force is

$$\overline{f} = g\, \overline{\Delta\rho} \tag{2.50}$$

with the meaning of Δ taken from eq. (2.49). The average sign on $\Delta\rho$ comes from the observation that it varies from $\Delta\rho \approx 0$, when the blob starts its motion, to some maximum value. An approximation to the average work from eq. (2.50) is then

$$l\, \overline{f} = -\frac{1}{2}\, l\, g\, \Delta\rho . \tag{2.51}$$

The kinetic energy of the blob is $\rho\langle v^2\rangle/2$, where $\langle v^2\rangle$ is the square of the average convective

velocity. Assuming $\overline{v}_\mathrm{c}^2 \approx \langle v^2 \rangle$, an estimate of $\overline{v}_\mathrm{c}$ can be obtained by equating the average kinetic energy with eq. (2.51):

$$\overline{v}_\mathrm{c} \approx \left(\frac{g}{\rho} \Delta\rho \right)^{1/2} l^{1/2} \,. \tag{2.52}$$

It has to be noted that different approximations may lead to slight differences with other values in literature. For example, our value of $\overline{v}_\mathrm{c}$ is smaller by a factor $\sqrt{2}$ with respect to eq. (19) in Woosley et al. (2004) which is, however, perfectly acceptable because the authors use the mixing-length theory only for an order-of-magnitude analysis.

3. The current status of the ignition theory

3.1. General features of the progenitor

According to stellar evolution models, CO WDs are the endpoint of the evolution of main sequence stars in the mass range $M \approx 3 - 9 M_\odot$ (Umeda et al. 1999). By mass accretion from a companion star the central density of the progenitor reaches values of the order of $10^9\,\mathrm{g\,cm^{-3}}$. In this conditions electrons in the matter are degenerate. This is a key detail for understanding the explosion mechanism of thermonuclear supernovae, because the degenerate matter does not permit any self-regulation for nuclear burning, as it happens in the hydrostatic evolution of ordinary stars (see e.g. Padmanabhan 2001).

At $\rho \approx 10^8 - 10^9\,\mathrm{g\,cm^{-3}}$ the degenerate electrons in the WD matter are also relativistic. This may be shown by the comparison between the Fermi momentum and $m_\mathrm{e}c$, where m_e is the electron mass. The critical density for which a relativistic treatment has to be taken into account is then

$$\rho_\mathrm{c} = \frac{8\pi}{3} m_\mathrm{p}\,\mu_\mathrm{e} \left(\frac{m_\mathrm{e}c}{h}\right)^3 \approx 10^6 \mu_\mathrm{e}\,\mathrm{g\,cm^{-3}}\,, \tag{3.1}$$

where m_p is the proton mass, h is Planck's constant and $\mu_\mathrm{e} = \rho/(n_\mathrm{e} m_\mathrm{p})$, with n_e indicating the electron density, is the mass per electron. $\mu_\mathrm{e} = 2$ for a pure composition of ^{12}C and ^{16}O in which proton and neutron numbers are equal.

As far as the WD's composition is concerned, $X(^{12}\mathrm{C}) = X(^{16}\mathrm{O}) = 0.5$ is adopted throughout this thesis work, although several one-dimensional simulations (for example Couch & Arnett 1975, Umeda et al. 1999, Höflich & Stein 2002) indicate that in the WD's interior the ratio $X(\mathrm{C})/X(\mathrm{O})$ is less than 1.

Again differently from normal stars, WDs are supported against gravity by the degenerate pressure, while in non-degenerate objects the pressure gradient in equation (2.42) is provided by the energy released by nuclear burning. It is important to note this, because in the following the nuclear reactions occurring in the WD core will be introduced and discussed. Though they are crucial for the onset of the explosion, they are not necessary for guaranteeing the hydrostatic equilibrium of the WD.

3.2. Physics of the ignition process

A noteworthy result of WD physics, useful for the understanding of the accretion phase, is the derivation of a relation between the WD mass M and the radius R (Chandrasekhar 1957). The relation is fitted by the formulae (Padmanabhan 2001)

$$R(M) \simeq 0.0406\,\mu_{\rm e}^{-1} R_{\odot} \left(\frac{M\mu_{\rm e}^2}{M_{\rm Ch}}\right)^{-1/3} , \tag{3.2}$$

$$R(M) \simeq 0.022\,\mu_{\rm e}^{-1} R_{\odot} \left(\frac{M}{M_{\rm Ch}}\right)^{-1/3} \left[1 - \left(\frac{M}{M_{\rm Ch}}\right)^{4/3}\right]^{1/2} , \tag{3.3}$$

in the non-relativistic and relativistic regimes, respectively. A related finding, anticipated elsewhere in this work for sake of clarity, is the existence of an upper limit for the WD mass, the Chandrasekhar mass $M_{\rm Ch} = 5.84/\mu_{\rm e}^2\ M_{\odot}$.

These formulae show that the WD radius scales as $R \propto M^{-1/3}$ in the non-relativistic regime, and the decrease of R with increasing M is even faster in the relativistic one. It may be understood in simple terms, treating the WD matter as a polytrope with the EOS given by $p = K\rho^{\gamma}$ (Chandrasekhar 1957), with the polytrope index ranging from $\gamma = 5/3$ for non-relativistic degenerate matter to $\gamma = 4/3$ in the relativistic case. The degenerate electron pressure must support the WD structure against gravity, hence the WD density must increase steeply with increasing mass for the needed pressure to be achieved. In the context of SN Ia progenitors it indicates that during the accretion phase in the binary system the WD density increases.

The energetics of the WD's interior during the accretion phase is determined by the following acting processes:

Compressional heating caused by accretion. Because of accretion onto the WD, as described by Iben (1982), there is a gravitational energy release with a local rate $\epsilon_{\rm g}$. This rate may be expressed as the sum of two contributions, a compression term $\epsilon_{\rm work}$ and an internal energy term $\epsilon_{\rm int}$:

$$\epsilon_{\rm g} = \epsilon_{\rm work} - \epsilon_{\rm int} = -p\frac{d(1/\rho)}{dt} + \frac{d\,e_{\rm int}}{dt} , \tag{3.4}$$

where $e_{\rm int}$ is the specific internal energy. Numerically, both terms at the right-hand side are up to three orders of magnitude larger than $\epsilon_{\rm g}$. According to eq. (3.4), the compressional energy release goes mostly into the internal energy term, which in turn is the sum of two parts. The dominating one is the kinetic energy of degenerate electrons, which increases with the increasing WD density, and only a small part contributes to the thermal energy of non-degenerate nucleons.

Nuclear burning. The compression and the heating cause the onset of hydrostatic carbon burning in the WD core; according to Nomoto (1982), the burning starts in the pycnonuclear regime and turns to the thermonuclear regime for $T > 5\times10^7$ K. The value

of the reaction rate at $T < 10^8$ K and the treatment of electron screening in this conditions (Ogata et al. 1991, Cussons et al. 2002, Itoh et al. 2003) are sources of relevant uncertainties at the beginning of the C-burning.

Some works (for example, Nomoto et al. 1984 and Nomoto & Iben 1985) take into account also the surface burning of the accreted matter, evaluating the timescale for the heat to flow inwards by conduction; this additional element is not included in more recent studies (Bravo et al. 1996, Yoon & Langer 2003) and, though interesting, is not necessary for the ignition of hydrostatic carbon burning.

Neutrino emission. The energy loss by neutrino emission is active at densities lower than about 2×10^9 g cm^{-3} (Arnett 1971, Nomoto et al. 1984, Woosley & Weaver 1986); in this condition, the dominating contribution to neutrino losses comes from the production of plasmon neutrinos, a mechanism described here following Clayton (1983) and Winget et al. (2004).

It is well known that a free photon, even with an energy $\hbar\omega > 2m_e c$, cannot produce an electron-positron pair: if the photon could spontaneously convert to $e^- e^+$, a Lorentz frame could be found in which the electron and positron would have equal and opposite momenta, and the photon would be at rest, contradicting the invariance of its propagation velocity in all frames. Therefore the pair production requires the presence of a "spectator" particle which ensures energy and momentum conservation. Analogously, a free photon cannot produce a pair of neutrino and anti-neutrino unless it is coupled to the plasma. Such a coupled photon is called a plasmon. Considering the stellar plasma as a dielectric for photon propagation, the dispersion relation between the photon angular frequency ω and the wavenumber k can be written as

$$\omega^2 = k^2 c^2 + \omega_0^2 \,, \tag{3.5}$$

where ω_0 defines the plasma frequency. The previous formula can be rewritten substituting for the photon the energy $E = \hbar\omega$ and the momentum $p = \hbar k$:

$$E^2 = p^2 c^2 + m_{\rm pl}^2 c^4 \tag{3.6}$$

with $m_{\rm pl} = \hbar\omega_0 / c^2$. The formula can be interpreted as an energy-momentum relation for a particle with non-zero rest mass $m_{\rm pl}$, called plasmon. The plasmons are hence defined as collective excitations of the electron plasma coupled with photons. This discussion implies that in an environment in thermal equilibrium the plasmons can be significantly excited only if the typical thermal energy $k_{\rm B}T$ is larger than $\hbar\omega_0$. The energy produced by the plasmon decay $\gamma^* \rightarrow \nu + \overline{\nu}$ is related to the plasmon mass. The plasma frequency ω_0 is expressed by the two formulae

$$\omega_0^2 = \frac{4\pi n_e e^2}{m_e} \,, \tag{3.7}$$

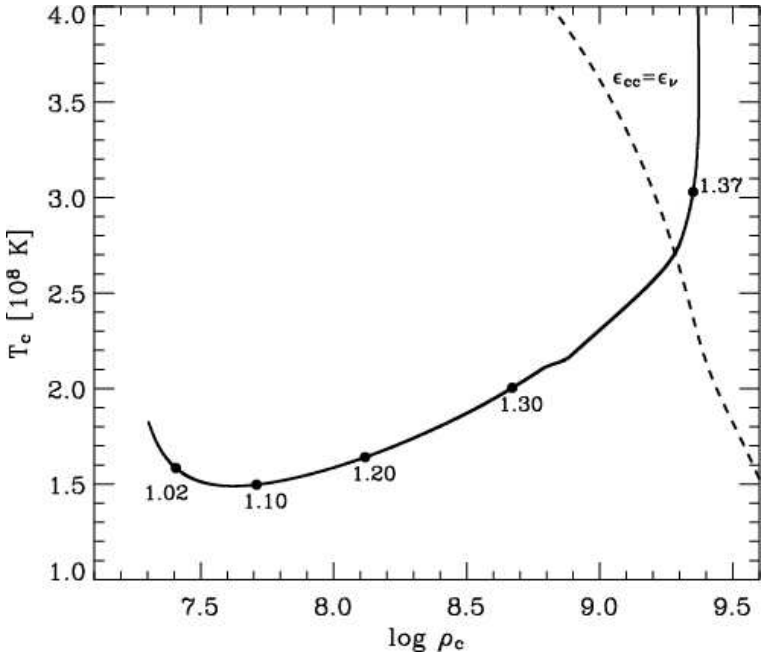

Figure 3.1.: Evolution of the central density and temperature in a WD model during binary evolution, from Yoon & Langer (2003). The numbers at the filled circles indicate the WD mass (in $M_\odot$), and the dashed line denote the locus where the energy generation rate of the carbon burning equals the neutrino losses.

---

where $n_e = \rho/(\mu_e\, m_p)$ is the electron density and e is the electron charge, and

$$\omega_0^2 = \frac{4\pi n_e e^2}{m_e}\left[1 + \left(\frac{\hbar}{m_e c}\right)^2 \left(3\pi^2 n_e\right)^{\frac{2}{3}}\right]^{-\frac{1}{2}} \tag{3.8}$$

in non-degenerate and degenerate limit, respectively. In the non-degenerate case we have $k_B T \gg \hbar\omega_0$, hence in principle the plasmons are excited, but their energy contribution in most astrophysical sites is negligible with respect to the energy of thermal photons. In the degenerate case the plasmon energy is relatively large ($\hbar\omega_0 \sim 0.7$ MeV at $\rho = 2 \times 10^9$ g cm^{-3}) and the energy losses are significant but, as density increases because of accretion, ω_0 increases too. The thermal photons have not enough energy for the plasmon excitation and the neutrino production is strongly suppressed.

The locus in the $(\rho_c\,;T_c)$ plane where the energy release due to carbon burning is equal to the energy loss by neutrino emission is referred, in all the studies on the ignition cited in this section, as the "ignition line" for the SN Ia explosion (fig. 3.1). Actually it is a questionable approximation because it only marks the start of the last phase of the progenitor evolution. In order to get rid of the energy output of the C-burning, the WD develops a convective core whose evolution is crucial for the knowledge of the ignition properties. The duration

of the convective phase is of the order of 10^3 years (Hillebrandt & Niemeyer 2000, Yoon & Langer 2003) which is however very short compared to the overall length of the accretion phase ($10^5 - 10^6$ years, cf. Han & Podsiadlowski 2004).

3.3. Final stage of the progenitor evolution

When the core temperature reaches $6 - 7 \times 10^8$ K, the convective zone encompasses most of the WD mass. Convection enters a reactive regime: it may be seen from the comparison between the convective turnover timescale τ_c and the nuclear timescale τ_n, defined as the time required to significantly reduce the carbon abundance in an isolated region of the fluid. It can be written as

$$\tau_c \simeq L / \bar{v}_c \ , \tag{3.9}$$

where L is the size of the convective zone and $\bar{v}_c$ is defined by eq. (2.52), and (cf. Woosley et al. 2004 for the case in analysis)

$$\tau_n = \left(\frac{1}{\dot{S}} \frac{d\dot{S}}{dt} \right)^{-1} \approx \left(\frac{1}{\dot{S}} \frac{\partial \dot{S}}{\partial T} \frac{\partial T}{\partial t} \right)^{-1} = \frac{C_p T}{23 \dot{S}} \approx 15 \left(\frac{7}{T_8} \right)^{22} \left(\frac{2}{\rho_9} \right)^{3.3} \text{s} \ , \tag{3.10}$$

where $T_8 = T/(10^8\,\text{K})$ and $\rho_9 = \rho/(10^9\,\text{g cm}^{-3})$. For $T_8 = 7$, $\rho_9 = 2$ (with $L \approx 10^8$ cm, estimated from the WD model and $\bar{v}_c \approx 4 \times 10^6\,\text{cm s}^{-1}$, derived from the mixing-length theory) it turns out that $\tau_c \simeq \tau_n$. In these conditions it makes clearly no sense to talk about blobs in convective cycles. The mixing-length theory cannot be applied successfully for modeling the last phases of the WD evolution. Nevertheless, some order-of-magnitude estimates may be derived using this theory.

At $T \simeq 10^9$ K the critical temperature (Timmes & Woosley 1992) for carbon burning is reached, i.e. the temperature where the energy generation rate equates the heat conduction rate:

$$\nabla(\kappa \nabla T) = \rho \dot{S} \ . \tag{3.11}$$

This point defines the start of the SN Ia explosion, the ignition of the thermonuclear runaway. The burning then proceeds as a subsonic flame, with a speed determined by the equilibrium between nuclear burning and heat conduction (see sect. 1.5.2).

It is clear that eq. (3.11) represents only a theoretical definition. As already described in sect. 1.7, a consistent ignition model is required to answer more detailed questions. In order to accomplish this aim, the analysis of the progenitor evolution must focus on the spatial and temporal development of the ignition process, tightly linked with the features of the last convective stage.

A suitable approach able to catch the multi-dimensional features of the reactive convection could be given by a direct simulation of this phase, but unfortunately it is hampered by the particular physical conditions of the WD. Convection develops on relatively long

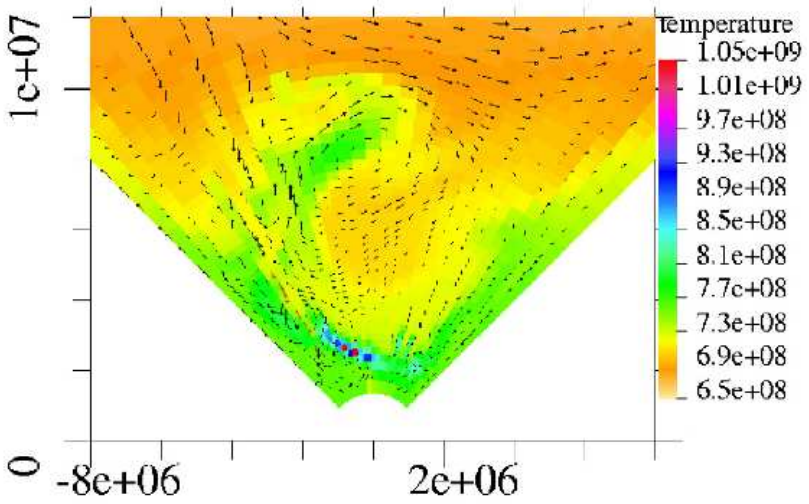

Figure 3.2.: Temperature at the runaway in a WD simulation in 2D, from Höflich & Stein (2002). On the axes, the length scales are expressed in centimeters. The vectors represent the convective velocities, typically in the range $30 - 60\,\mathrm{km\,s^{-1}}$. The runaway occurs in the red cells, at a central distance of 27 km, that is virtually at the WD center.

timescales, and simulations performed by explicit hydrocodes would be computationally too expensive, because of the constraint on the timestep (cf. sec. 4.2). The highly subsonic regime of the convective motions is also matter of concern (see appendix A). A 2D simulation, performed with an implicit code and limited to the last few hours before the runaway has been performed by Höflich & Stein (2002). To date, this is the only multi-dimensional simulation of the final evolution of a Chandrasekhar-mass CO WD to the thermonuclear runaway. According to the results of this work, the ignition occurs at the center of the WD, and it is induced by the compressional heating caused by the convective flow (fig. 3.2).

These conclusions can be challenged by the same arguments as in Woosley et al. (2004). The central ignition could be an artifact caused by the forced symmetry of the 2D simulation or by an insufficient spatial resolution. In the same work, the authors review some experiments on Rayleigh-Bénard convection cells, introducing the Rayleigh number as

$$Ra = \frac{g\, l^3\, \rho^2\, C_\mathrm{P}\, \delta_\mathrm{p}\, \Delta T}{T\, \eta\, \kappa} \tag{3.12}$$

where $\delta_\mathrm{p} = -(\partial \ln \rho / \partial \ln T)_\mathrm{p}$, ΔT is defined by eq. (2.49), η is the viscosity and κ is the thermal conductivity. In the WD core, $Ra \sim 10^{25}$.

Following the suggestions by Kadanoff (2001) about the flow features at very large Rayleigh numbers and the analogy with terrestrial experiments, Woosley et al. (2004) suppose that the flow pattern in WD convection can be different from the "canonical" (and one-dimensional) view of a centrally symmetric model with the convective velocity vanishing

at the WD center. A dipolar model for convection is thus proposed in which matter flows from one side to another of the WD passing through the center. The dipole flow introduces a privileged direction in the WD, breaking the central symmetry. The implications of this model for the SN ignition will be discussed, among other possibilities, in the sections 3.4.2 and 3.5.

3.3.1. Thermal profile of the progenitor and convective URCA process

Up to this point, the discussion has been focused on the maximum temperature reached inside the WD, without investigating the general thermal state of the progenitor before the runaway or, going back to a one-dimensional idea, its thermal profile as a function of the central distance.

It may be seen that this issue has no importance when the SN Ia *explosion* is simulated. Actually all the multi-dimensional studies implement the initial conditions of a "cold" WD, with a locally constant value of $10^5 - 10^6$ K. Though these values are far from being realistic, the buoyancy of a burned fluid element does not depend significantly on the background state because the ashes are however much hotter and lighter than the surrounding material. A numerical experiment performed using the FLASH code (Fryxell et al. 2000, cf. cap. 4), with the setup described in chapter 5, shows indeed that the value of the density contrast $\Delta\rho/\rho$, proportional to the buoyant velocity (eq. 3.21), decreases only of about 5% when the WD temperature is increased from 10^6 to 7×10^8 K.

The situation is different when one has to determine the ignition conditions. In that case, as it will be shown in sect. 6.5.1, the knowledge of the temperature profile before the runaway seems crucial for a detailed analysis because it strongly influence the buoyancy. As a working hypothesis, several progenitor models implement an adiabatic profile (e.g. Woosley et al. 2004, Wunsch & Woosley 2004) as a consequence of the convection. The fluctuations ("bubbles") occurring over this profile are the main subject of this thesis work and will be presented in detail in the next section of this chapter. The rest of this section will be devoted to review the convective URCA process whose effect on the convection and the temperature profile is potentially important and still debated.

The URCA process (Gamow & Schoenberg 1941) is the cycle of electron captures and beta decays involving the nuclei $(Z+1, A)$ and (Z, A):

$$e^- + (Z+1, A) \longrightarrow (Z, A) + \nu_e \;\; ; \;\; (Z, A) \longrightarrow (Z+1, A) + e^- + \bar{\nu}_e \; .$$

The net effect of this cycle is a production of neutrinos and hence an energy loss. In degenerate matter electron captures dominate when the Fermi energy is larger than their threshold energy, while beta decays are more effective in the opposite case. Recalling that the Fermi energy depends on the matter density, if the density profile in the WD is considered it turns out that in a shell with $\rho \approx \rho_{threshold}$ both reactions are significant. This defines an Urca shell for the pair of nuclei under consideration. An important URCA pair in CO WDs is ^{23}Na /

^{23}Ne (Bruenn 1973), with an electron capture threshold on ^{23}Na of 4.38 MeV, corresponding to a density of 1.7×10^9 g cm^{-3}, slightly lower than the estimated density at ignition. During the last phase of the progenitor evolution the URCA shell is encompassed in the convective zone. The effect of this convective URCA process on the energy balance is unclear, though it has been addressed in several works (e.g. Paczyński 1972, Mochkovitch 1996, Stein et al. 1999) taking into account step by step more pieces of physics. A formalism for the description of the convection as a two-stream flow has been derived by Lesaffre et al. (2005). The application to the convective URCA process is under way, and early results show that even a small abundance[1] ($X \approx 10^{-8}$) of URCA pair nuclei can have a significant impact on the convective velocities, because the electron captures can alter the electron abundance, linked to the mass density and thus to the buoyancy effects. The knowledge of the electron abundance Y_e and its dependence on the convective URCA process are also very important for SN Ia nucleosynthesis (Travaglio et al. 2004), for Y_e determines which isotopes are mostly produced in the NSE burning regime.

3.3.2. Rotating WDs and ignition

Another issue in the ignition theory is rotation; to date, it has not been included in multi-D simulations of SN Ia explosions, and its role is unexplored. On the other hand, the effects of rotation on the accretion phase of the binary system have been studied in 1D (e.g. Piersanti et al. 2003, Yoon & Langer 2004) and recently in 2D (Yoon & Langer 2005). The details of these rotating models are beyond the scope of this work. However, it would be interesting to investigate if rotation could introduce some anisotropy on the ignition process and the further impact on the explosion features. Also the possibility of super-Chandrasekhar WDs supported by rotation is worth being studied further.

3.4. Temperature fluctuations in the WD core

The formation of temperature fluctuations (often called simply “bubbles” in the following) in the WD’s convective core is deeply connected with the turbulent behavior of the matter in this astrophysical site. The formation of such bubbles can be explained in terms of velocity fluctuations. Considering the high sensitivity of the C-burning rate on temperature ($\dot{S} \propto T^{23}$ at $T \sim 7 \times 10^8$ K), it may be proved (Woosley et al. 2004) that one half of the energy is produced in a small (estimated mass of $0.01\,M_\odot$, corresponding to about 130 km for the WD model examined by those authors) central part of the convective core. Deriving their heuristic convection model, Wunsch & Woosley (2004) estimate the temperature gain δT

[1] It is obvious that the hypothesis on the WD composition, $X(^{12}\mathrm{C}) = X(^{16}\mathrm{O}) = 0.5$, must be slightly relaxed in this framework.

experienced by a fluid element, passing through this energy generation core for a residence time t_b:

$$\frac{\delta T}{T_0} \simeq \frac{t_b}{\tau_n} \tag{3.13}$$

where T_0 is the adiabatic background temperature and τ_n is the nuclear timescale, defined by eq. (3.10). When a fluid element, during the convective motion, approaches the energy generation core with a velocity smaller than the average convective velocity, it resides there for a slightly longer time than the average, and thus it becomes hotter than the surrounding material.

As this section will show, the bubbles have a key role in the ignition theory because they are considered the "seeds" for the subsequent flame propagation in the explosion; the study of the bubble features is therefore a powerful tool for investigating the ignition process. Some physical properties of these objects are introduced below.

3.4.1. Features of the bubbles

Temperature and density

Considering a bubble as an isobaric perturbation, its thermal excess with respect to the background temperature is accompanied by a density deficiency. At constant pressure, Woosley et al. (2004) estimate the logarithmic derivative of density with respect to temperature:

$$\delta_p = -\frac{\partial \ln \rho}{\partial \ln T} = \frac{T}{\rho}\frac{\Delta \rho}{\Delta T} \approx 1.9 \times 10^{-2}\,\frac{T}{\rho} \tag{3.14}$$

for a range near $T_8 = 7$ and $\rho_9 = 2$. This numerical result refers to the EOS implemented in the code used by those authors, but its meaning has general validity for the degenerate matter: the density dependence on temperature is very small. Woosley (2001) provides some significant calculations about it: the convective velocity estimated from the mixing-length theory, when $T_8 = 7$, is $40\,\mathrm{km\,s^{-1}}$. From eq. (2.52), one can see that this velocity corresponds to a density contrast $\Delta\rho/\rho \simeq 2 \times 10^{-5}$ and, by eq. (3.14), to a $\Delta T/T \simeq 3 \times 10^{-3}$. At $T_8 = 8$, a similar calculation leads to $\Delta T/T = 3\%$.

Maximum diameter

The maximum diameter of the bubbles can be roughly evaluated (Woosley et al. 2004) considering that a turbulent flow is characterized by eddies of different sizes, which can generate or disrupt the temperature fluctuations. A length scale for the fluctuations can be defined by λ_{turb}, the distance over which the adiabatic T profile in the WD varies of a temperature excess ΔT (cf. 2.49):

$$\lambda_{turb} = \frac{\Delta T}{\nabla T_{ad}} \sim 1\,\mathrm{km}\,, \tag{3.15}$$

where $\nabla T_{\rm ad}$ is the adiabatic temperature gradient. In principle, from this estimate one can infer that the number of bubbles hosted in WD interior can be very large. In a sphere of 100 km of diameter there can be of the order of 10^6.

Energy balance and minimum diameter

In order to estimate the minimum diameter, one has to take into account the relevant terms for the energy balance of a reactive bubble:

- Nuclear reactions. The C-burning in the bubble leads to a temperature increase, which causes the thermonuclear runaway when $T \approx 10^9$ K. The timescale for a bubble to reach the runaway is calculated from eq. 3.10. Actually this equation provides the nuclear timescale $\tau_{\rm n}$, i.e. the timescale for fuel consumption, but it is equal to the required timescale for the temperature increase, observing that at $T = 10^9$ K the C-burning is almost instantaneous.

- Heat diffusion. This term leads to a temperature decrease, on a timescale (Landau & Lifshitz 1995)

$$\tau_{\rm cond} = \frac{\rho\, C_{\rm P}\, l^2}{\kappa}\ , \tag{3.16}$$

  where l is the characteristic size of the bubble.

- The bubble is less dense than the surrounding material, so it is subject to buoyancy. The specifics of the bubble motion will be introduced below. In this framework one should however note that a moving bubble experiences an adiabatic expansion during its rise in the WD. According to Woosley et al. (2004) the adiabatic temperature gradient in the central region of the WD is expressed by

$$\left(\frac{dT}{dr}\right)_{\rm exp} \approx -0.037 T_{\rm c} \left(\frac{\rho_9}{2}\right)^{2/3} r_7\ , \tag{3.17}$$

  where $r_7 = r/(10^7$ cm), being r the distance from the WD center.

Let a bubble be at rest. Then the last contribution can be neglected. The heat diffusion term is proportional to the bubble area. One can define the minimum size for the bubble, as the diameter of the bubble in which the heat generated by nuclear burning is balanced by heat diffusion. By equating the timescales of the two processes (eqs. 3.10 and 3.16) one finds in the WD conditions

$$\lambda_{\rm min} = \left(\frac{T\,\kappa}{23\,\rho\,\dot{S}}\right)^{1/2} \tag{3.18}$$

For a numerical estimate of $\lambda_{\rm min}$ the numerical values of $\kappa \approx 3 \times 10^{18}\,{\rm erg\,cm^{-1}\,K^{-1}\,s^{-1}}$ and

$$\dot{S} \approx 2.8 \times 10^{13} \left(\frac{T_8}{7}\right)^{23} \left(\frac{\rho_9}{2}\right)^{3.3} \,{\rm erg\,g^{-1}\,s^{-1}} \tag{3.19}$$

are used (Woosley et al. 2004). Taking $T_8 = 7$ and $\rho_9 = 2$, this derivation leads to $\lambda_{\rm min} \approx 40\,{\rm cm}$; with $T_8 = 8$ and $\rho_9 = 2$, $\lambda_{\rm min} \approx 10\,{\rm cm}$. This original derivation gives results that are similar to other scale analyses performed by Woosley et al. (2004) and García-Senz & Bravo (2005).

Bubble dynamics

The acceleration $g_{\rm eff}$ exerted by the buoyancy force on a rising bubble is proportional to its density contrast:

$$g_{\rm eff}(r) = g(r)\,\frac{\Delta\rho}{\rho} = \frac{G\,M(r)}{r^2}\,\delta_{\rm p}\,\frac{\Delta T}{T}\ . \tag{3.20}$$

The bubble is subject to the Rayleigh-Taylor instability and rises. Its velocity tends to a value $v_{\rm b}$, determined by the equilibrium between buoyancy and drag forces. The problem has been studied theoretically (Davies & Taylor 1950, Taylor 1950, Layzer 1955), numerically (Glimm & Li 1988, Li 1996) and experimentally (Read 1984). A general expression for $v_{\rm b}$ is

$$v_{\rm b} = c_1 \sqrt{\frac{g_{\rm eff}\,D}{4}}\ , \tag{3.21}$$

where D is the bubble diameter and c_1 is a dimensionless constant whose value is about 0.5. The interpretation of the previous formula and its validity range will be discussed in sect. 6.3.3.

It is very instructive to compare eq. (3.21) with the average convective velocity $\overline{v}_{\rm c}$ (eq. 2.52):

$$\frac{v_{\rm b}}{\overline{v}_{\rm c}} \sim \left(\frac{D}{l}\right)^{1/2}\ . \tag{3.22}$$

Since the mixing length l can be considered to be a length scale for the extent of the convective zone, it is clearly $l \gg D$; it shows that in the WD core the large-scale convective velocities are much larger than the buoyant bubble velocities (cf. Wunsch & Woosley 2004).

Other features of the bubble motion related to the fluid instabilities (for example, the dispersion) will be presented directly in the discussion of the performed simulations (chap. 6).

3.4.2. Analytic models of floating bubbles in WDs

The idea of the ignition of SN Ia explosion driven by floating bubbles has been proposed first by García-Senz & Woosley (1995). In this work, the authors develop an analytic model for

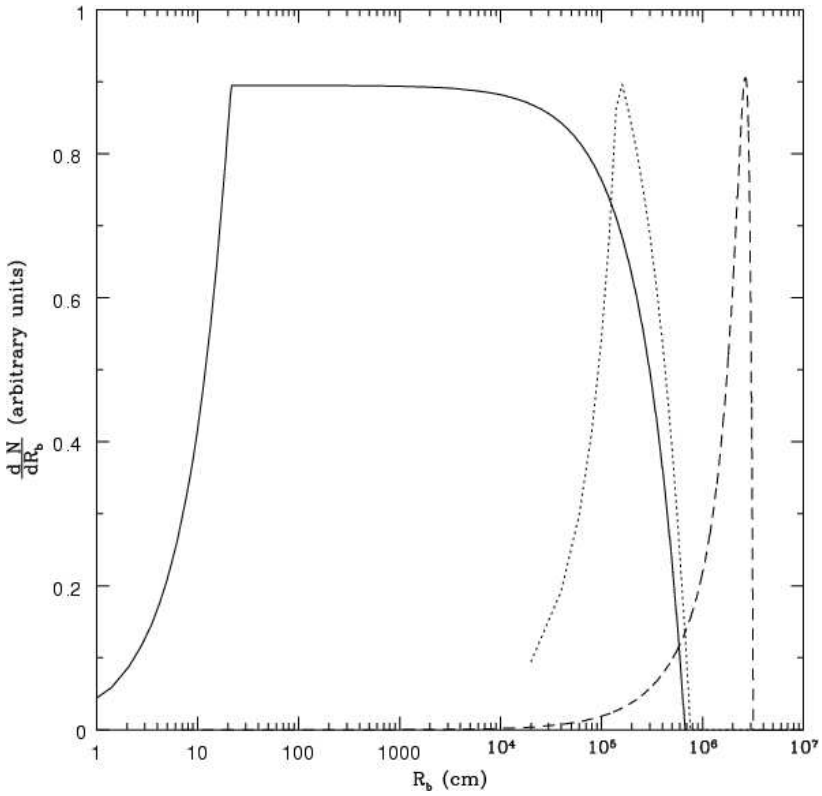

Figure 3.3.: Distribution function of bubble radii R_b for different values of R_0. Solid line: $R_0 = 10^4$ cm; dotted line: $R_0 = 10^6$ cm; dashed line: $R_0 = 10^7$ cm. From García-Senz & Bravo (2005).

the buoyant evolution the burning bubbles. They perform a parameter study, investigating the response of the motion to variations of the initial bubble position, the diameter, and the temperature excess. The conclusion is that the bubbles reach the runaway temperature when they are at a central distance in the range 100 – 250 km, moving with a speed of about 100 km s^{-1}.

The topic has been resumed by Woosley et al. (2004), coupled with results from the mixing-length theory and suggestions from Rayleigh-Bénard convection. Some ideas of this treatment were already inserted in this chapter. About the ignition these authors conclude that it is initiated by the bubbles at a central distance up to about 150 – 200 km, when the central WD temperature is about $7.7 - 7.9 \times 10^8$ K. Another claim is that a multi-point ignition is, in principle, possible. This results is obtained by evaluating that the e-folding timescale for the bubble number is comparable with the time for the expansion in the SN Ia explosion to shut off the ignition (0.1 s).

The ignition process has been addressed in a more general, heuristic model of turbulent convection also by Wunsch & Woosley (2004). Two convective flow patterns are considered, an isotropic turbulent flow and a dipolar jet flow (cf. sect. 3.3). The conclusions for

the SN ignition are similar to the previous work as far as the central WD temperature is concerned. On the location of the hottest points in the WDs the authors consider the competition between nuclear heating and adiabatic cooling, estimating that the ignition points should be concentrated at about 100 km from the WD center. For an isotropic flow it means that the ignition points should occur likely in a *shell* of 100 km of diameter, while for a dipole flow these points would be clustered rather along the flow axes.

Recently García-Senz & Bravo (2005) have studied the distribution function of bubble sizes for different values of the characteristic length scale of the bubble thermal profile R_0 (fig. 3.3). The actual value of this parameter has not been evaluated by those authors but, considering the turbulent state of the WD core, it is claimed to tend towards the lower end of the explored range.

3.5. Initial conditions of SN Ia simulations

The initial flame displacement in multi-dimensional simulations of SN Ia explosions is considered basically a free parameter, though constrained by the cited works on the ignition. Because of this, most simulation schemes are tested against different sets of initial flame shapes, allowing a comparison of the results for various setups.

Several possible initial conditions have been implemented in the recent supernova literature. The most obvious one, also for its use in 1D simulations, is the centrally ignited flame (fig. 3.4).

In some works a sinusoidal perturbation is superimposed to the flame front in order to provide structures for the growth of the Rayleigh-Taylor instability (e.g. Niemeyer & Hillebrandt 1995, Reinecke et al. 1999, 2002a) and to avoid the slower growth of the instability from numerical noise. In this context the initial setup of Calder et al. (2004), which follows a different choice, is particularly interesting. It consists of a spherical flame seed without perturbations, enclosing the WD center but with the seed center not overlapping with the WD center (12 km off-center). In their 3D simulation the flame rises by buoyancy to the WD surface without triggering a successful explosion. This outcome, presented by the authors as a proof against the centrally ignited scenarios, deserves further tests.

A different ignition condition is provided by a number of spherical flame kernels displaced in the innermost part of the WD and detached from the center. It should be noted that these flame seeds *are not* the “same” bubbles presented in the previous sections. The bubbles belong to an earlier, pre-explosive stage before a flame forms, while the latter (in order to stress the difference) will not be called *bubbles* in this thesis work but with other names, like for example *flame seeds*, *blobs* or *flame kernels*, and consist of burned ashes surrounded by the propagating flame.

Early works in 2D (Niemeyer et al. 1996, Reinecke et al. 1999) implemented only a few blobs per octant (as shown for example, in 3D, in fig. 3.5, left), while newer simulations have a finer spatial resolution and allow the displacement of more seeds (fig. 3.5, right). Nevertheless, the maximum number of blobs which can be set is bound to their size, and in

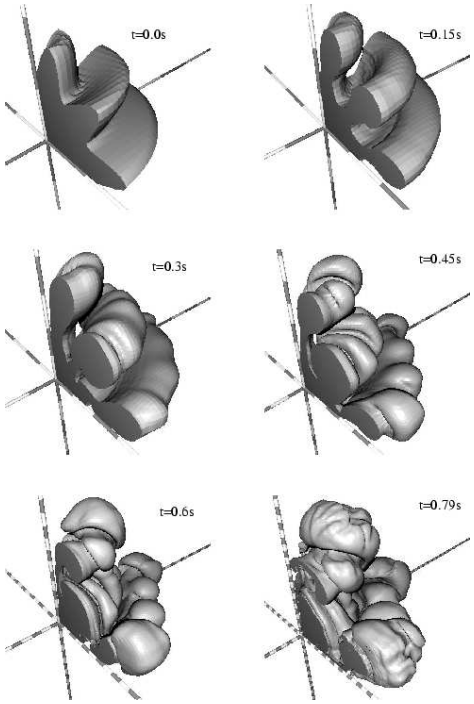

Figure 3.4.: Initial flame shape and flame evolution in a 3D simulation of one WD octant (from Reinecke et al. 2002a). One ring on the axes corresponds to 100 km. In the initial setup, the volume enclosed by the flame is filled with burned ashes.

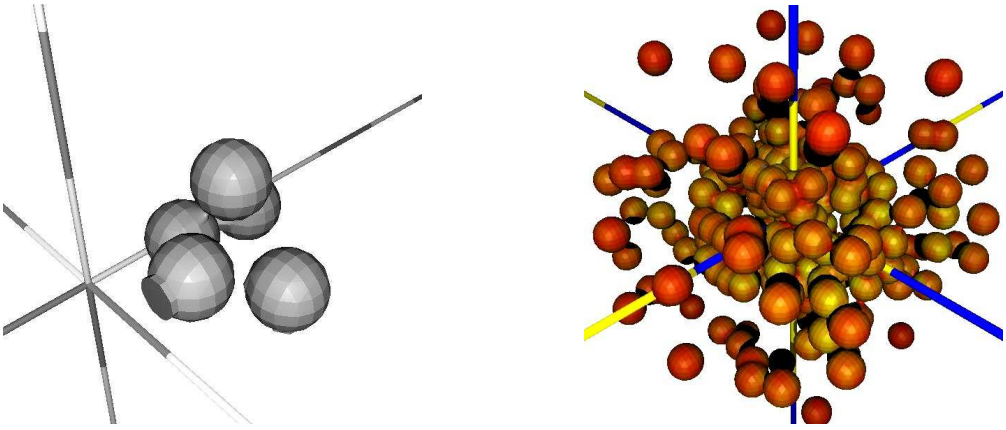

Figure 3.5.: Multi-spot ignition setups. Left (from Reinecke et al. 2002b): the initial conditions for a 3D simulation of one WD octant. Five blobs with 20 km of radius, displaced within 160 km from the WD center. Right (from Travaglio et al. 2004): 30 bubbles per octant, radius of 10 km. In both figures, a ring on the axes corresponds to 100 km.

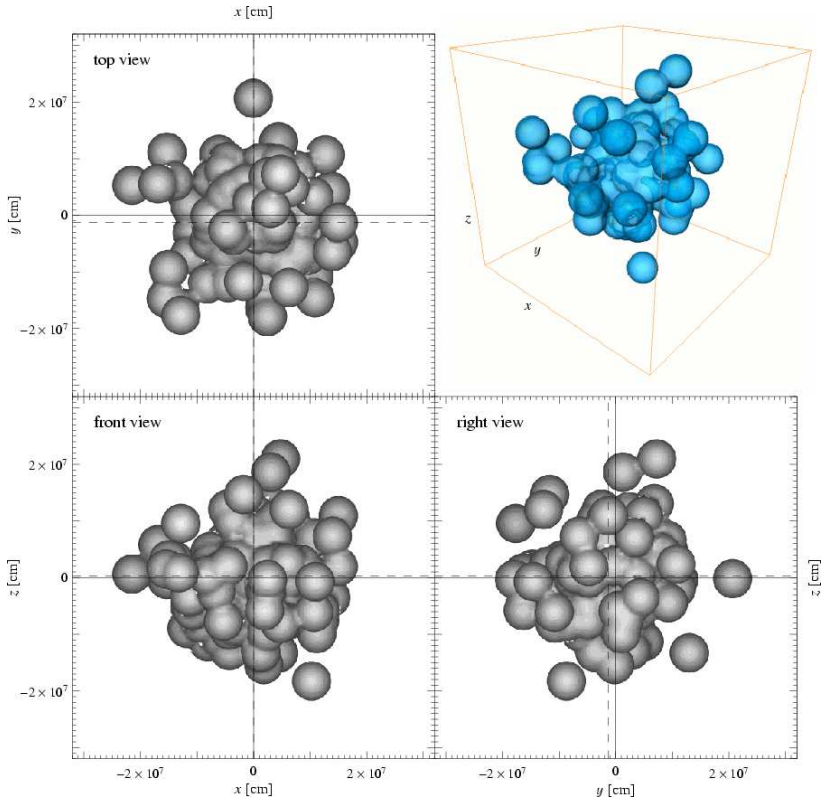

Figure 3.6.: Initial flame displacement from Röpke & Hillebrandt (2005b). In the projections, the solid lines denote the WD center, while the dashed lines denote the center of the flame configuration.

turn this is still constrained by the resolution, more than by physical grounds. The spatial resolution of state-of-the-art 3D calculations is still not good enough for a more realistic number of kernels to be allocated (cf. also with the inferred bubble sizes and number, sect. 3.4.1). This situation can probably be cured by the use of co-expanding computational grids (Röpke 2005).

An hybrid approach between centrally ignited flame and multi-spot scenario is presented by Röpke & Hillebrandt (2005b). Their initial flame configuration is realized by placing flame kernels with radius of 3.5 km in a Gaussian distribution, centrally centered, and with a dispersion of 100 km. The setup allows blob overlapping. The result is shown in fig. 3.6. A few blobs are detached, up to a central distance of about 200 km, but most of them are gathered together around the WD center. Because of the random process of blob displacement the resulting configuration is 13.4 km off-center. This setup leads to a successful explosion though, in principle, the slightly off-center ignition scenario is somewhat analogous to that of Calder et al. (2004). Clearly, the initial presence of a highly perturbed flame shape plays an important role for the subsequent propagation.

The availability of full-star explosion simulations can address another interesting class of

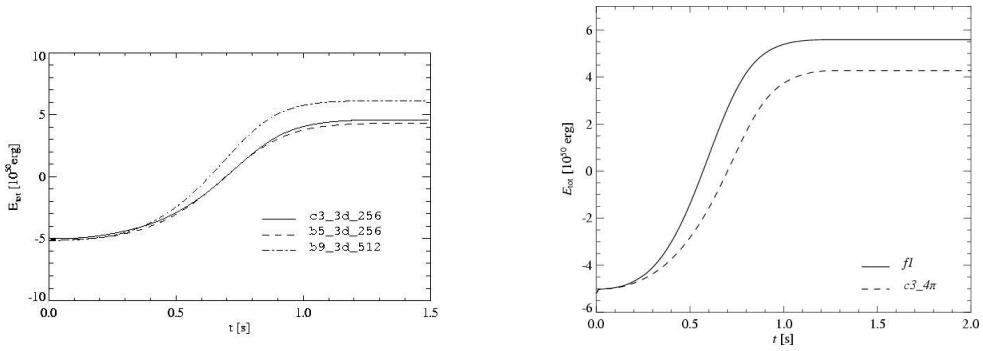

Figure 3.7.: Comparison of the evolution of explosion energy in different 3D simulations. Left: Results of 3D simulations of one WD octant, from Reinecke et al. (2002b). Solid line: the central ignition scenario presented in fig. 3.4, in a simulation carried out on a grid with 256^3 cells. Dashed line: the same initial conditions as fig. 3.5, left, grid with 256^3 cells. Dashed-dotted line: a setup with nine ignition points and resolution of 512^3 cells. Right: Results of 3D full-star simulations, from Röpke & Hillebrandt (2005b). Solid line: the initial flame configuration of fig. 3.6. Dashed line: central ignition analogous to fig. 3.4, but performed in the whole solid angle.

initial conditions, the strongly asymmetric ones, which could arise from dipole convection as supposed by Woosley et al. (2004). No clear indication of the outcome from such conditions can be found in literature. This is also true for the "shell-like" ignition conditions speculated by Wunsch & Woosley (2004). Woosley et al. (2004) notice also that, analogously to the work of Kuhlen et al. (2003), rotation could break the dipolar flow and bring back the convective pattern to isotropy. Once more, it is evident the importance of studying in detail the progenitor evolution.

The influence of different initial conditions on the outcome of the explosion have been remarked in several works. A first change in differently ignited models is in the total energy. Reinecke et al. (2002b) have compared three 3D simulations of one WD octant: a centrally ignited explosion and two multi-point ignited, with 5 and 9 blobs respectively. The differences in total energy are relatively small (fig. 3.7, left), and it leads the authors to conclude that it could be difficult to explain the observed energy range of "normal" SNe Ia only on the basis of different ignition conditions. However, an initially larger number of blobs produces more vigorous explosions, because the initial flame surface is relatively larger and it can provide more flame acceleration. Also the comparison of different initial conditions in Röpke & Hillebrandt (2005b) (fig. 3.7, right) shows that the "foamy" initialization provides more seeds for the development of instabilities and gives a larger total energy.

A common problem in pure deflagration SN Ia simulations is the presence of a substantial amount of unburned CO material. The synthetic nebular spectra based on these explosion models (see Kozma et al. 2005 for a recent work on this subject) present strong O I lines, due to the low-velocity unburned material left in the central region. They are in clear dis-

agreement with the observations of nebular spectra of SNe Ia. This shortcoming could be partly cured by a larger amount of flame seeds in the initial conditions (see for example Travaglio et al. 2004, which implement the initial setup of fig. 3.5, right).

Is there any meaningful limit to be put on the number of blobs? García-Senz & Bravo (2005) show that, in their SPH 3D simulation, an increase of the number of ignition points over 30 (keeping the initial amount of burned mass constant) does not influence the explosion observables in a significant way. One should point out, however, that it has not been proven whether this effect is physical or linked to the spatial resolution of their simulation.

It is also obvious that starting a SNIa simulation from an excessively large number of big blobs is just a naive trick. Such an initial setup could ignite almost instantaneously most of the WD core and probably solve the energy and composition problem, but it would leave the questions on the ignition process unanswered. A truly "first principle calculation" has rather to start with the smallest initial fraction of burned material (within the limits imposed by the spatial resolution) in order to study consistently the evolution of the explosion and its features.

4. Numerical tools

4.1. The FLASH code

The simulations which will be shown in the next chapters have been produced using the FLASH code (Fryxell et al. 2000), version 2.3, released in May 2003. This hydrodynamical code was developed with a modular structure in order to study a broad range of astrophysical problems, mainly concerning astrophysical flashes but also covering other fields, like for example cosmology and fluid instabilities. The ASC / Alliance Center for Astrophysical Thermonuclear Flashes at the University of Chicago develops, updates and tests the code, taking care of regular verification and validation on a suite of test problems (Calder et al. 2002).

The FLASH code has been used, among other topics, for the study of SN Ia explosions (Calder et al. 2004, Plewa et al. 2004) and, incidentally, also in a work on the morphology of rising bubbles (Robinson et al. 2004), though in a context which is completely different from this thesis work, namely cooling flows in galaxy clusters.

In the next sections the main features of the code will be reviewed together with the modules which have been selected for the study of the SN Ia ignition problem.

4.2. Handling of the hydrodynamical equations

The approach of the FLASH code for the solution of the Euler equations is based on the finite volume method (LeVeque 1998). The computational domain is divided into grid cells such that, considering a generic variable $q(\mathbf{x}, t)$, its value in the cell i is given by some average of q over the cell. This approach permits the use of the integral form of the Euler equations (cf. eq. 2.1) and, since they express conservation laws, an advantage of the finite volume method is that it ensures conservation in managing the fluxes of the variables over the grid cells.

The problem of defining the flux of a variable q between neighboring cells can be solved as a Riemann shock tube problem at the cell boundaries. This method has been introduced first by Godunov (1959). The version implemented in FLASH is a higher order algorithm of the Godunov scheme, called PPM (piecewise-parabolic method, Colella & Woodward 1984, Woodward & Colella 1984), in which the state variables inside a cell are not piecewise-

constant but are represented as parabolae. The solver in FLASH descends from the PPM implementation of the PROMETHEUS code (Fryxell et al. 1989).

In order to guarantee that sound waves emitted at the cell interfaces do not travel over a path larger than the cell length, a constraint is set on the timestep. It is analogous to the CFL condition for the convergence of an explicit numerical method. The condition for the hydrodynamical timestep Δt reads in the FLASH code:

$$\Delta t < \min\left\{\frac{dx_i}{|u_i| + c_\mathrm{s}}\right\} = C \min\left\{\frac{dx_i}{|u_i| + c_\mathrm{s}}\right\} , \tag{4.1}$$

where dx_i is the cell size along the dimension i, u_i is the related velocity component and c_s is the sound speed in the considered medium. C (< 1) is the Courant number. The actual Δt is the minimum of this quantity, calculated over all grid cells.

Multi-dimensionality is handled by directional splitting, instead of solving a multi-dimensional Riemann problem. It means that at every time update the one-dimensional Riemann solver (and also every other selected physics module) is called twice in every direction. In 2D, for example, the sequence is $x - y$ and, the second time, $y - x$ for ensuring symmetry in the directional splitting.

4.3. Adaptive mesh refinement

In grid-based calculations situations may occur, in which a high spatial resolution is not needed everywhere in the computational domain. In these cases, the computational resources can be optimized by setting a fine grid only in the most relevant part of the domain. The grid mesh should also have the capability of evolving in time together with the problem under examination. The adaptive mesh refinement (AMR) is a suitable approach to this demand. It finds applications in several astrophysical codes (see Norman 2004 for a recent review).

The PARAMESH package (MacNeice et al. 1999) manages in FLASH all the issues related to refinement criteria, flux conservation and distribution of work to processors. A concrete example of the use of AMR will be provided in sect. 5.2. The computational advantage, with respect to an uniform grid, is evident, but one should keep in mind that the gain in resolution is also accompanied by a decrease of the timesteps, according to eq. (4.1).

4.4. Equation of state

Among the equations of state provided with FLASH, the most appropriate for the thermodynamical state of the WD is the Helmholtz EOS, described by Timmes & Swesty (2000).

It includes many contributions from the relevant physics. The total pressure and internal energy can be written as

$$p_{\rm tot} = p_{\rm rad} + p_{\rm ion} + p_{\rm ele} + p_{\rm pos} + p_{\rm coul} \tag{4.2}$$

and

$$e_{\rm int,tot} = e_{\rm rad} + e_{\rm ion} + e_{\rm ele} + e_{\rm pos} + e_{\rm coul} \tag{4.3}$$

where the subscripts at the right-hand side indicate the contributions from radiation, ions, electrons, positrons and Coulomb corrections, respectively. The radiation part is treated as a blackbody in local thermodynamical equilibrium, the ion part as an ideal gas, electrons and positrons in the non-interacting Fermi gas formalism. Moreover, the Coulomb interaction of the ionized nuclei with the electron gas is taken into account. The detailed formulae for each term can be found in Fryxell et al. (2000).

For an understanding of the implementation of the Helmholtz EOS, the expression for the first law of the thermodynamics is recalled:

$$de_{\rm int} = T dS + \frac{p}{\rho^2} d\rho \ . \tag{4.4}$$

It is an exact differential. Following the argument of Timmes & Swesty (2000), an EOS is thermodynamically consistent if, from the eq. (4.4), the three thermodynamic identities

$$p = \rho^2 \left.\frac{\partial e_{\rm int}}{\partial \rho}\right|_T + T \left.\frac{\partial p}{\partial T}\right|_\rho \tag{4.5}$$

$$\left.\frac{\partial e_{\rm int}}{\partial T}\right|_\rho = T \left.\frac{\partial S}{\partial T}\right|_\rho \tag{4.6}$$

$$-\left.\frac{\partial S}{\partial \rho}\right|_T = \frac{1}{\rho^2}\left.\frac{\partial p}{\partial T}\right|_\rho \tag{4.7}$$

are satisfied. This is easily accomplished by using the Helmholtz free energy F, the most suitable thermodynamic potential when the natural variables for the problem are temperature and density:

$$F = e_{\rm int} - TS; \qquad dF = -S dT + \frac{p}{\rho^2} d\rho \ . \tag{4.8}$$

From the previous formula, one can derive the pressure as

$$p = \rho^2 \left.\frac{\partial F}{\partial \rho}\right|_T \tag{4.9}$$

and the entropy as

$$S = -\left.\frac{\partial F}{\partial T}\right|_\rho \ . \tag{4.10}$$

Together with the requirement on the double derivatives,

$$\frac{\partial^2 F}{\partial T\,\partial \rho} = \frac{\partial^2 F}{\partial \rho\,\partial T} \tag{4.11}$$

the last three expressions, substituted in the eqs. (4.5)-(4.7), satisfy the requirement of thermodynamical consistency. In the practical implementation, the Helmholtz free energy for electrons and positrons is stored in tabular form, while the other contributions are calculated from analytical functions. The physical limits of this EOS are $10^{-6} < \rho < 10^{11}\,\mathrm{g\,cm^{-3}}$ and $10^4 < T < 10^{11}\,\mathrm{K}$, well embracing the range of thermodynamical conditions which are explored in this work.

4.5. Nuclear reaction network

The choice of the nuclear reaction network is particularly critical for a hydrocode (see for example Timmes (1999) for a discussion of this problem). It has been estimated that when the number of isotopes goes over ~ 30 the computational cost of evolving their abundances dominate the calculation. For the study of bubble physics in CO WDs, however, a simple reaction network can be a fair approximation since the interest is focused on the nuclear energy generation rather than on the detailed nucleosynthesis. Motivated by the comparative study of Timmes et al. (2000) in this physical framework, the α-chain network `iso7` has been chosen. It consists of a chain of reactions (α,γ) and (γ,α) linking the α-nuclei between ^{4}He and ^{28}Si. From this nucleus the flow towards higher mass numbers is followed with a simplified approach. The reaction network skips directly to ^{56}Ni through an analytic expression. For comparison, a complete α-network requires 13 nuclei from ^{4}He to ^{56}Ni, but the described implementation includes only 7 isotopes.

One can verify that this network is adequate for the hydrostatic C-burning in the WD interior. Indeed, looking at the simulation data which will be presented, it turns out that the maximum abundances of intermediate mass nuclei are always very low compared with the values for ^{12}C and ^{16}O. We find approximately $X(^{20}\mathrm{Ne}) \simeq 0.003$, $X(^{24}\mathrm{Mg}) \simeq 10^{-6}$, $X(^{28}\mathrm{Si}) \simeq 10^{-8}$. Thus the flow towards ^{32}S and beyond can safely be neglected. Concerning this issue Timmes et al. (2000) compare the `iso7` with other larger networks and put a condition for the activation of the channel between ^{28}Si and ^{56}Ni. It is open in the network only if $T > 2.5 \times 10^9\,\mathrm{K}$ and $X(^{12}\mathrm{C}) + X(^{16}\mathrm{O}) > 0.1$. Both conditions are far form being fulfilled in the bubble simulations presented here.

The nuclear burning in FLASH works with a temperature-limited timestep in order to avoid that in some cells the energy generation is comparable with the internal energy. Practically, it expresses the requirement that the timestep has to be smaller than the local nuclear timescale (eq. 3.10). The timestep limiter Δt_{burn} is defined by

$$\Delta t_{\mathrm{burn}} = F\,\frac{T}{\Delta T}\,\Delta t_{\mathrm{burn,old}} \tag{4.12}$$

where F is a numerical parameter, set to 0.01 for optimal performance, ΔT is the temperature difference from one timestep to the next, and $\Delta t_{\mathrm{burn,old}}$ is the previous timestep. In the conditions of hydrostatic C-burning this limiter is always much larger than the hydrodynamical timestep (eq. 4.1), which actually controls the time advancement.

The burning module in FLASH includes also screening effects according to the formulation of Wallace et al. (1982) and neutrino losses (Itoh et al. 1996).

In the current version of FLASH there is no module for the treatment of the flame propagation. The simulations are followed until $T \approx 10^9$ K and are stopped if they reach such temperature, which corresponds to the flame ignition. Since this work is devoted to the study of the progenitor's evolution *before* the runaway is initiated this limitation does not harm the results.

5. Setup of the simulations and preliminary tests

5.1. Goals and method

In general, every numerical simulation is based on a large number of assumptions. This chapter is devoted to the description of the simulation setup and reviews the adopted parameters, choices and approximations. As motivated in chapter 3, in order to study the ignition of SNe Ia the physics of the bubbles will be examined by means of 2D simulations. Instead of studying directly the last phase of convection by a simulation of the whole WD (as will be discussed in appendix A), the work will be focused on a series of simulations of a single bubble whose morphological and thermal evolution will be analyzed later (sect. 6.3).

A broad range of physical conditions for the bubble generation and evolution will be explored by means of a parameter study. It will be performed by varying three relevant quantities over intervals which will be specified:

- The initial bubble temperature. Since too little is known about the temperature profile inside the bubbles (cf. García-Senz & Bravo 2005), the temperature perturbation is initially set to be isothermal in the simulations. This choice, in comparison with a Gaussian bubble profile, helps also in containing spurious numerical dispersions of the bubbles, which will be discussed deeply in sect. 6.3.4.

- The initial bubble diameter.

- The initial distance of the bubble from the WD center. As shown already in sect. 3.4, bubbles are generated in the energy-producing core of the WD. Since their velocity is much smaller than the typical convective velocity (cf. sect. 3.4.1) a likely view is that the bubbles are embedded in the convective motions and carried by them at different distances from the center.

The parameter study has to ask some basic questions on the bubble features. Its aim is to understand if any (physically meaningful) favored combination of the listed parameters exists which leads to the thermonuclear runaway, and what are the related timescales and the relevant physics involved. This analysis, together with the discussion about the implications for the ignition process of SNe Ia, will be carried out in chap. 6.

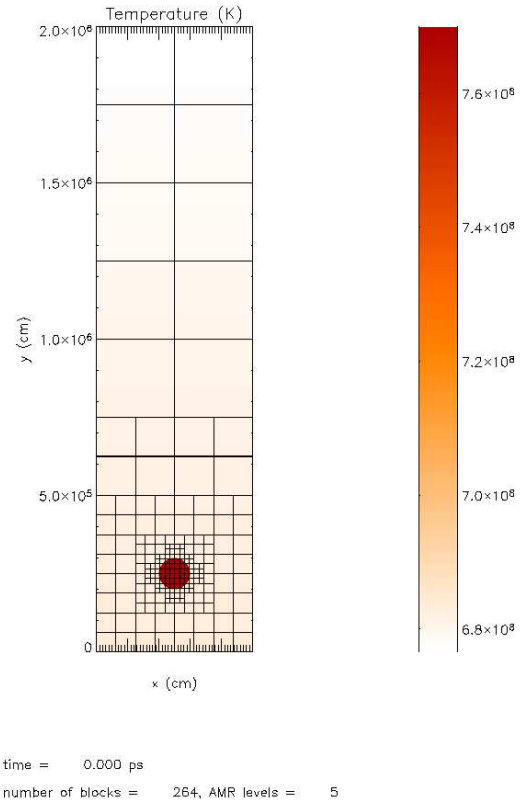

Figure 5.1.: Temperature plot, representing the initial setup of a bubble simulation. The temperature scale is color coded. The grid mesh is superimposed to the plot; each square is defined as a "block" of the AMR structure and contains 8×8 computational cells. The plot refers to a calculation with initial bubble temperature equal to 7.7×10^8 K, bubble diameter 1 km, initial distance from the center 100 km.

5.2. Computational domain and related issues

In the general strategy followed in the simulations, the computational domain encloses only a small part of the WD. In this domain the bubble is set. Since most of the calculations are performed with bubbles of 1 km of diameter, the following description will refer to this case (for different bubble diameters one just has to scale the lengths accordingly).

Figure 5.1 is an example of the appearance of the computational domain at the beginning of a 2D bubble simulation. It will help to visualize the features listed in this section.

First one can notice that the geometry of the simulation shown in fig. 5.1 is Cartesian. Section 5.7 justifies why this choice is adopted in the performed simulations.

The extent of the computational domain is 5×20 km. The bubble is initialized there as an isothermal perturbation in pressure equilibrium with the surrounding matter. The values of the thermodynamical variables in the domain are obtained from a one-dimensional WD

model provided by S. Woosley, with $M_{\rm WD} \approx 1.38 M_\odot$, $R_{\rm WD} \approx 1600\,$km, $T_{\rm c} = 7 \times 10^8\,$K, $\rho_{\rm c} = 2.55 \times 10^9\,{\rm g\,cm^{-3}}$. The extent of the convective zone in the model is about 1000 km.

The computational domain encloses a relatively small part of the WD. Hence a reasonable approach is to neglect the curvature effect and to map the data from the WD model in the plane-parallel approximation in such a way that the values of the physical quantities in the domain at the coordinate y are taken from the quantities in the WD model at the radius $R - y_{\rm b} + y$, where R is the central bubble distance and $y_{\rm b} = 2.5\,$km is the y coordinate of the bubble center in the computational domain. Before being mapped in 2D, the data are slightly modified to ensure the hydrostatic equilibrium, as will be described in sect. 5.3. A detailed geometrical analysis shows that at the distances from the WD center that are chosen in the simulations the curvature effects have the same order of magnitude as the adopted grid resolution, justifying the adopted approximation.

In sect. 5.6 we present tests for the evaluation of the optimal resolution. It is however worth anticipating some considerations, based on fig. 5.1. In this figure, five levels of grid refinement are used. Each square in the grid is a "block", the unit for the handling of AMR in FLASH; each block contains 8×8 grid zones. In the AMR structure, the finest level of refinement corresponds to an effective grid size, along the direction i, given by the formula

$$N_i^{\rm zones} = 2^{l-1}\, N_{{\rm blocks},i}\, N_{\rm zones/block}\ , \tag{5.1}$$

where l is the level of refinement, $N_{{\rm blocks},i}$ is the number of blocks of level 1 set on the direction i and $N_{\rm zones/block}$ is the number of zones per block, which has been set to 8 in our setup, as reported above. In the setup of the simulations performed $N_{\rm blocks,x} = 2$ and $N_{\rm blocks,y} = 8$ were used, such that the effective grid size at the fifth level of refinement is $[256 \times 1024]$, corresponding to a spatial resolution of $2 \times 10^3\,$cm. It is interesting to notice that a uniform grid of this resolution would have 262 144 zones while this AMR grid has initially only 264 blocks $\times\, (8 \times 8) = 16\,896$ zones, most of them located near the bubble.

The boundary conditions adopted in the domain are reflecting in y, while in x they are periodic in Cartesian geometry and reflecting in cylindrical geometry. Test simulations have shown that the size of the computational domain is adequate for following the bubble evolution over the required timescales (a few seconds).

5.3. Hydrostatic equilibrium and mapping of the initial model

In the previous section we have explained how the computational domain is filled with data from a 1D model of a WD. This problem is not trivial. When a 1D model, initially in hydrostatic equilibrium (in the following, HSE), is mapped onto a new grid, interpolations and roundoff errors are introduced in the initial state, pushing the model out of HSE. A common source of error is, for example, the use of two different EOS, when creating and remapping the model. A further ambiguity concerns the convectively unstable models where

a convective velocity field is necessary for the energy transport but is usually neglected in the mapping procedure. These difficulties often result in the development of spurious velocities during the simulations. It has been verified in test simulations that without slight modifications of the WD data, these velocities are of the same order of magnitude as the bubble velocity and thus mask the relevant physical processes.

This drawback can be avoided using a mapping procedure which forces the model into HSE. It is implemented in FLASH and described by Zingale et al. (2002). The procedure works by iterating between the HSE equation (eq. 2.42), which in 1D can be simply written as

$$\frac{dp}{dy} = g\rho \tag{5.2}$$

and the EOS. A technical difficulty is that the finite-volume methods deal with cell-averaged quantities. In solving eq. (5.2) one cannot use for the generic variable f a function $f(z)$ such that $f(z_i) = f_i$. But it is more appropriate to construct a function f which satisfies the condition

$$\frac{1}{\delta z}\int_{z^-}^{z^+} f(z')dz = \langle f\rangle_i \ , \tag{5.3}$$

where δz is the zone size, the integration is performed over the zone length and $\langle f\rangle_i$ is the value of f in the zone i. Zingale et al. (2002) provide a list of polynomial reconstruction functions for f with different orders of approximation. In this work, a quadratic fit for the density was used and a cubic fit for the pressure, thus rewriting eq. (5.2) as

$$\langle p\rangle_{+1} - \langle p\rangle_0 = \frac{g\,(\delta y)}{12}\,(5\langle\rho\rangle_{+1} + 8\langle\rho\rangle_0 - \langle\rho\rangle_{-1}) \tag{5.4}$$

which has to be solved for $\langle p\rangle_{+1}$ and $\langle\rho\rangle_{+1}$. The other subscripts refer to neighboring cells.

In practice, the initial model of the WD is read from the code. The temperature profile is passed without changes,while density and pressure are slightly tweaked by iterative calls of the EOS and the previous equation until a required tolerance is reached. The value of the gravitational acceleration g is provided by the gravity module (sect. 5.4).

If eq. (5.2) is not exactly satisfied, as explained above, spurious velocities arise in the model. A further technical difficulty is that density and pressure are calculated by the hydrodynamic solver and gravity comes from a separate source term module or is “static”, i.e. computed only once from the initial model (a satisfactory approximation in situations where the equilibrium does not evolve noticeably with time, as in the WD problem). The identity in eq. (5.2) has to be maintained by the cancellation of two terms, calculated in two different parts of the code with errors that can be significant. FLASH implements an option which modifies the left and right interface states which are used for the solution of the Riemann problem (cf. sec. 4.2). The pressure that is locally supporting the matter against gravity is subtracted from the pressure field because it is not available for generating waves. This runtime option has been profitably used in the bubble simulations. Together

with the described mapping procedure, it produces background velocities that are negligible if compared with the buoyant velocity.

5.4. Treatment of the gravitational force

The FLASH code can include several gravity modules self-consistently computed from the Poisson equation (eq. 2.13) or externally applied. Since the bubble simulations are performed in a finite part of the WD, the selected gravity module in this setup must belong to the second group, and specifically a spatially constant gravitational force is applied to the computational domain. This choice could seem inconsistent with the density profile of the WD model (from which a gravity profile $g(y)$ can be calculated by eq. 2.42; cf. fig. 6.1). Actually, the computational domain is rather small along the y axis (and the extent of the bubble motion, as it will be shown, is even smaller), so a value for g which is locally constant on the domain differs from $g(y)$ only by a few percent and provides better results for the stability of the flow on the computational domain. The constant values of g are taken from $g(y)$ for $y = R$, where R is the initial bubble distance from the WD center.

5.5. Computational issues

On the point of view of the computational resources the 2D simulations which will be presented in this thesis have been particularly demanding. As it results from eq. (4.1), inserting the values $dx = 2 \times 10^3$ cm, $c_s \approx 10^9\,\mathrm{cm\,s^{-1}}$ and $C = 0.8$ for Cartesian calculations (for stability reasons $C = 0.4$ is used in cylindrical coordinates), the timestep is about 1.6×10^{-6} s. The typical timescale in the simulations is about 2 s, hence the number of required timesteps is very large. The constraint on the timestep is a characteristic limitation on the use of explicit hydrocodes.

The calculations were performed on the the IBM pSeries “Regatta” Supercomputer at the Garching Rechenzentrum of the Max-Planck-Gesellschaft. Most of the simulations have been computed running 64 1.3 GHz Power 4 processors in parallel (technical details at `http://www.rzg.mpg.de/computing/IBM_P/hardware.html`) with five levels of refinement. Each simulation required on average 1500 computational hours. From these numbers it is clear that a 3D study of the bubble problem would not have been affordable with the numerical tools which have been used.

5.6. Resolution test

After the considerations concerning the computational costs of the simulations, it is very important to find an acceptable compromise between a good spatial resolution and the feasibility of a whole parameter study, of many calculations. The effect of changing resolution can be easily quantified, When the spatial resolution is doubled, because of AMR the grid is

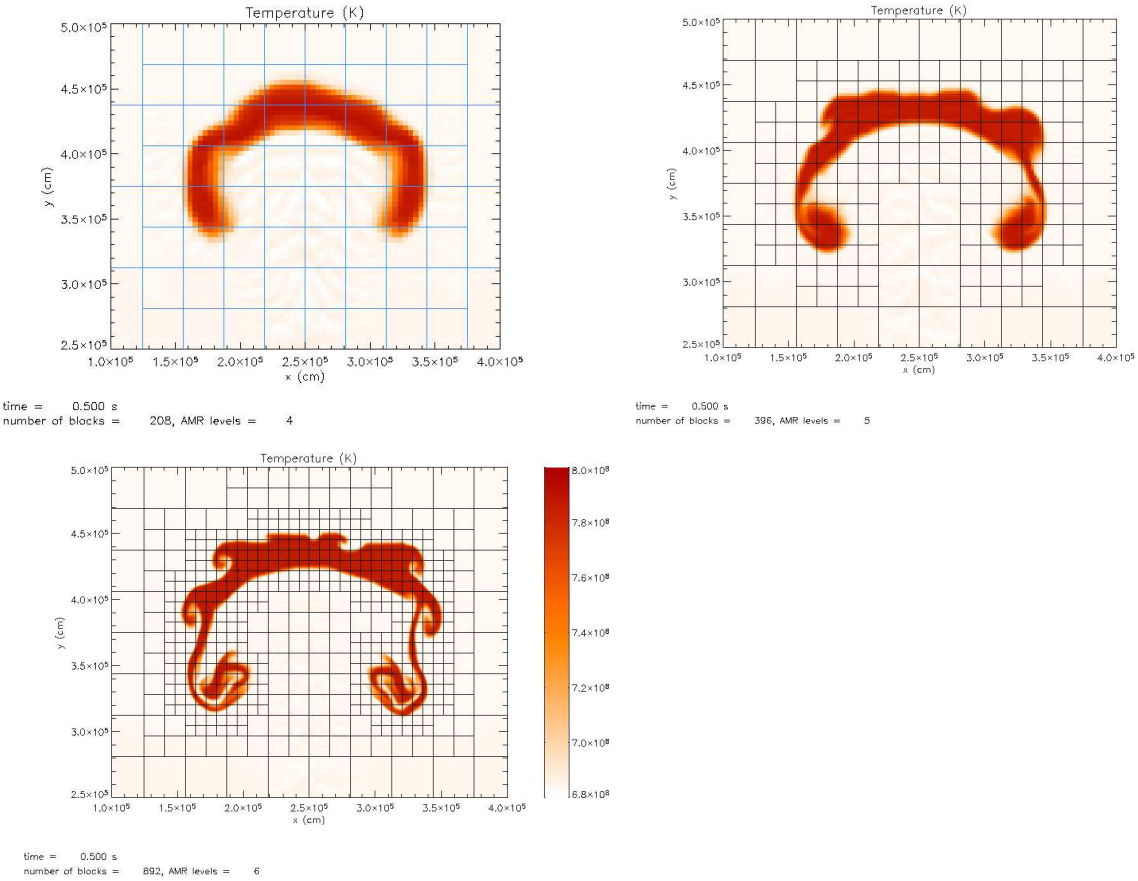

Figure 5.2.: Comparison of three temperature plots of buoyant bubbles, after 0.5 s of simulation, with increasing spatial resolution, shown by the grid mesh. The plots enclose only a small part of the computational domain, centered on the bubble. The choice of the initial parameters is identical in the three cases: temperature 7.7×10^8 K, diameter 1 km, distance from the center 100 km.

refined only on the bubble location. The computational time increases of a factor of almost 4, a factor of 2 for the timestep decrease (eq. 4.1) and about a factor of 2 for the increased number of grid zones. Typical numbers can be found by comparing the number of blocks of the plots with different AMR levels in fig. 5.2. It should be noted that with an equally spaced grid (no AMR), the doubling of the resolution would lead to a factor of 8 increase in the computational time, namely a factor of 4 for the zone number and a factor of 2 for the timestep decrease.

Figure 5.2 shows a comparison of the morphology between different resolutions. A detailed discussion of the features of buoyant bubbles is however postponed to sect. 6.3. The simulation with six levels of refinement looks very well resolved. The bubble shows several structures due to Rayleigh-Taylor and Kelvin-Helmholtz instabilities. The scope of this work is not to follow in such detail the bubble morphology, also because a non-moving

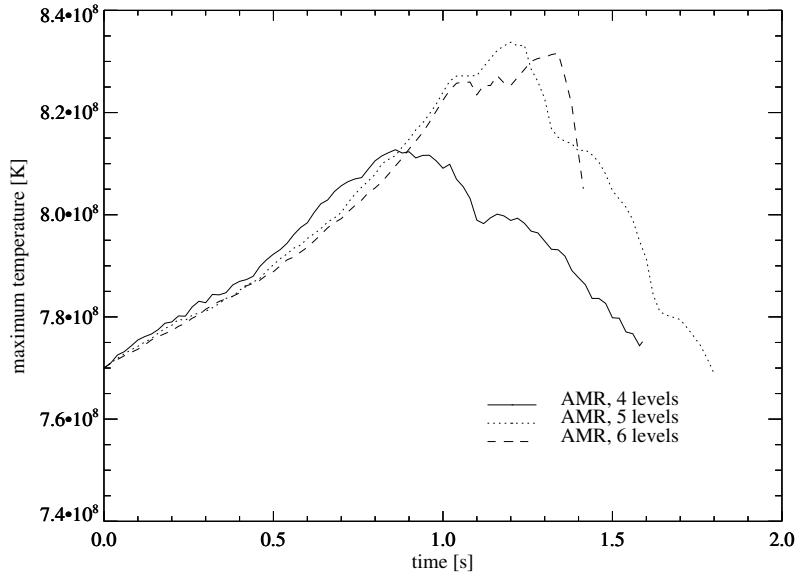

Figure 5.3.: Comparison of the maximum bubble temperature as a function of time in simulations with three different levels of refinement (cf. fig. 5.2). The temperature evolution is very similar in the two highly resolved calculations.

background is only an approximation (see sect. 6.3.5). For this aim, the simulation with six AMR levels is over-resolved, and the ideal resolution has to be chosen among 4 and 5 refinement levels.

The analysis of fig. 5.3 further helps to single out the best compromise. The figure shows the maximum bubble temperature as a function of time for three different resolutions. In the three cases, the temperature increases with the same slope because the burning depends on temperature and not on resolution. Then it reaches a peak and starts declining. This unexpected feature is a spurious effect (cf. sect. 6.3.4). From the discussion of this numerical issue it appears clearly that the earlier temperature decrease of the calculation with four levels of refinement is due to the lack of spatial resolution. Thus, five AMR levels is the refinement adopted in this work, unless differently specified. The discussion in sect. 5.2 refers to this case, and to the spatial resolution associated to it (2×10^3 cm).

5.7. Tests of the geometry

In fig. 5.1, the initial setup of a Cartesian simulation is shown. In principle, this is not the most natural choice of geometry since a bubble is a spherical object and it would be better represented in 2D in cylindrical coordinates, exploiting the axial symmetry. The 3D underlying shape of the object in fig. 5.1 is actually an infinite cylinder pointing in the direction of view. As will be shown below, its morphological evolution is different from

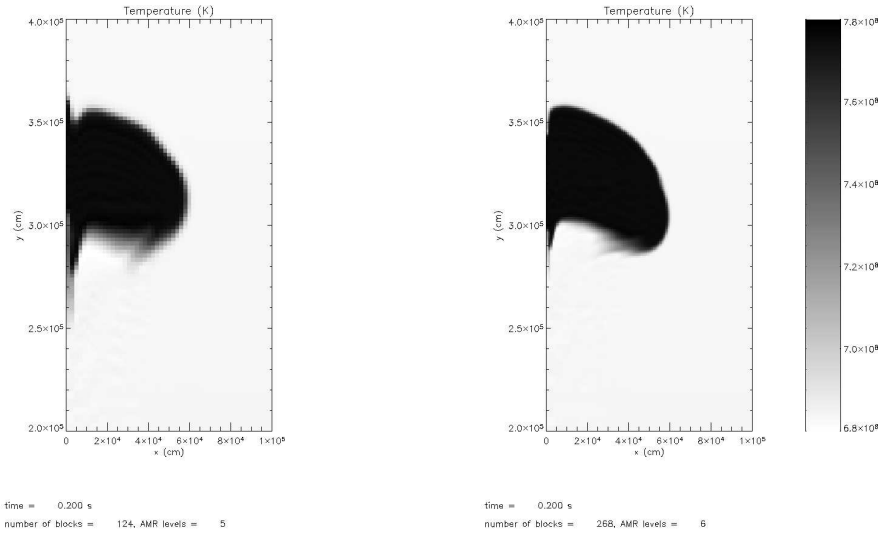

Figure 5.4.: Comparison between the bubble morphology in two cylindrical simulations, with 5 (left) and 6 (right) levels of refinement. In the former, the bubble shape along the symmetry axis is distorted. The effect is minimized by a finer resolution and a smaller Courant number.

the bubble in the cylindrical case. Nevertheless, the choice of the Cartesian geometry is acceptable and even useful, as it will be discussed in this section.

2D simulations in cylindrical geometry present special difficulties with respect to Cartesian coordinates. Figure 5.4 shows that the bubble morphology on the symmetry axis is strongly distorted ("axis jet"), when five levels of refinement are used. The problem is partly fixed by adding a further level of refinement and using a Courant number of 0.4, i.e. paying in terms of computational performance. For consistency, the comparison will be made between two simulations with six levels of refinement, in Cartesian and cylindrical geometry.

Morphological differences are pronounced in the two cases (fig. 5.5 and 5.6). In the cylindrical calculation, the bubble evolves with a thinner shape and develops a torus, well visible at 0.5 s at $y = 4 \times 10^5$ cm. This structure is similarly observed in Robinson et al. (2004). On the other hand, the Cartesian calculation shows evidently hydrodynamical instabilities and, at least in this early phase of the bubble evolution (here it is plotted only to 0.5 s), the overall shape is more compact and less dispersed than in the cylindrical case.

In order to understand the plots in fig. 5.7 one has to make use of the bubble diagnostics that will be introduced in sect. 6.2. The temperature evolution in the two geometries is rather similar (fig. 5.7*a*) at least in the increasing phase (when the numerical dispersion is not acting), because the nuclear burning depends only on temperature and not on geometry. The bubble velocities (fig. 5.7*b*) are different, probably because the two rising objects, in principle, have not the same 3D shape and this leads to different drag forces. In fig. 5.7*c*, the

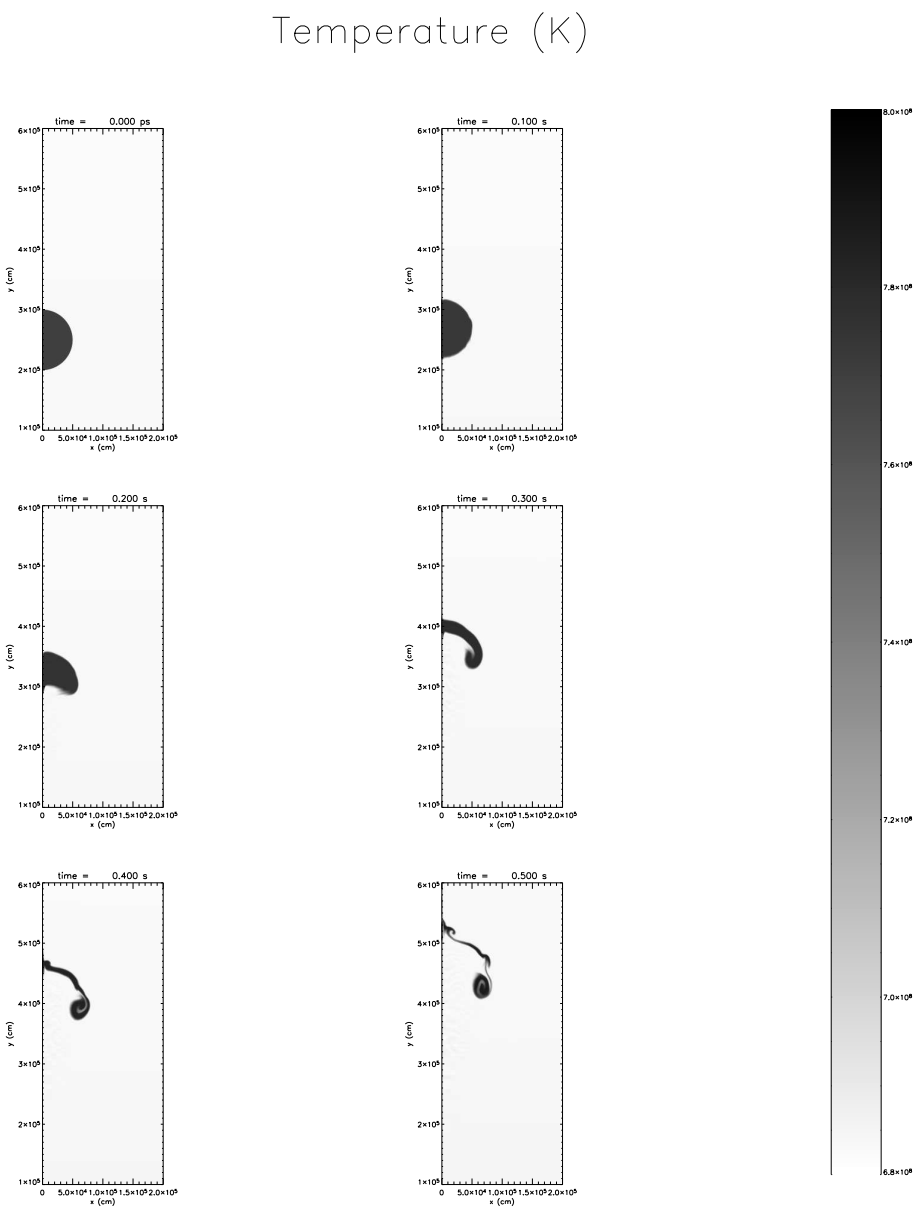

Figure 5.5.: Series of temperature plots showing the evolution of a bubble in a simulation with cylindrical geometry. Initial parameters: temperature 7.7×10^8 K, diameter 1 km, central distance 100 km. Six levels of refinement are used (spatial resolution: 10^3 cm).

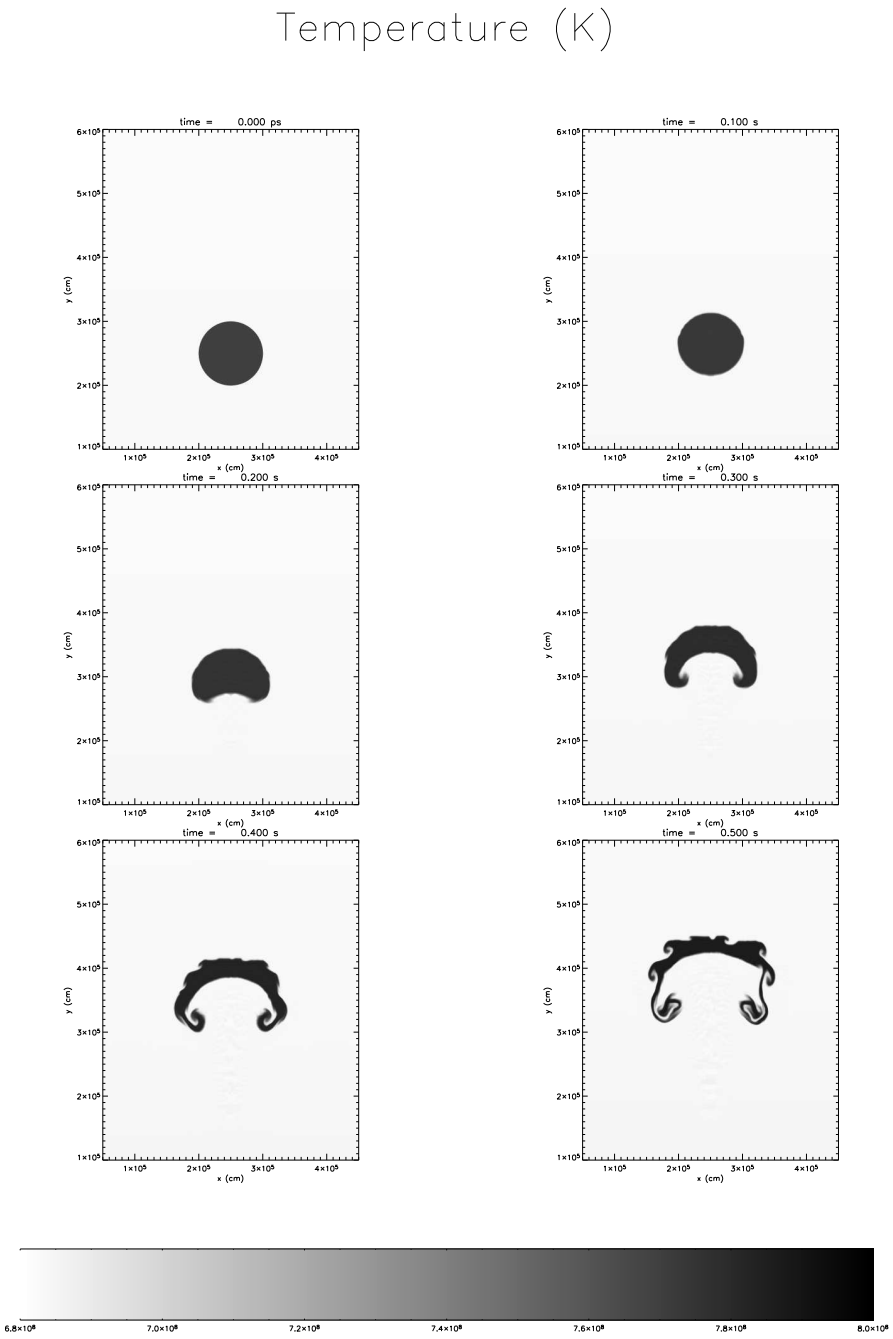

Figure 5.6.: The same of fig. 5.5, but for a simulation with Cartesian geometry.

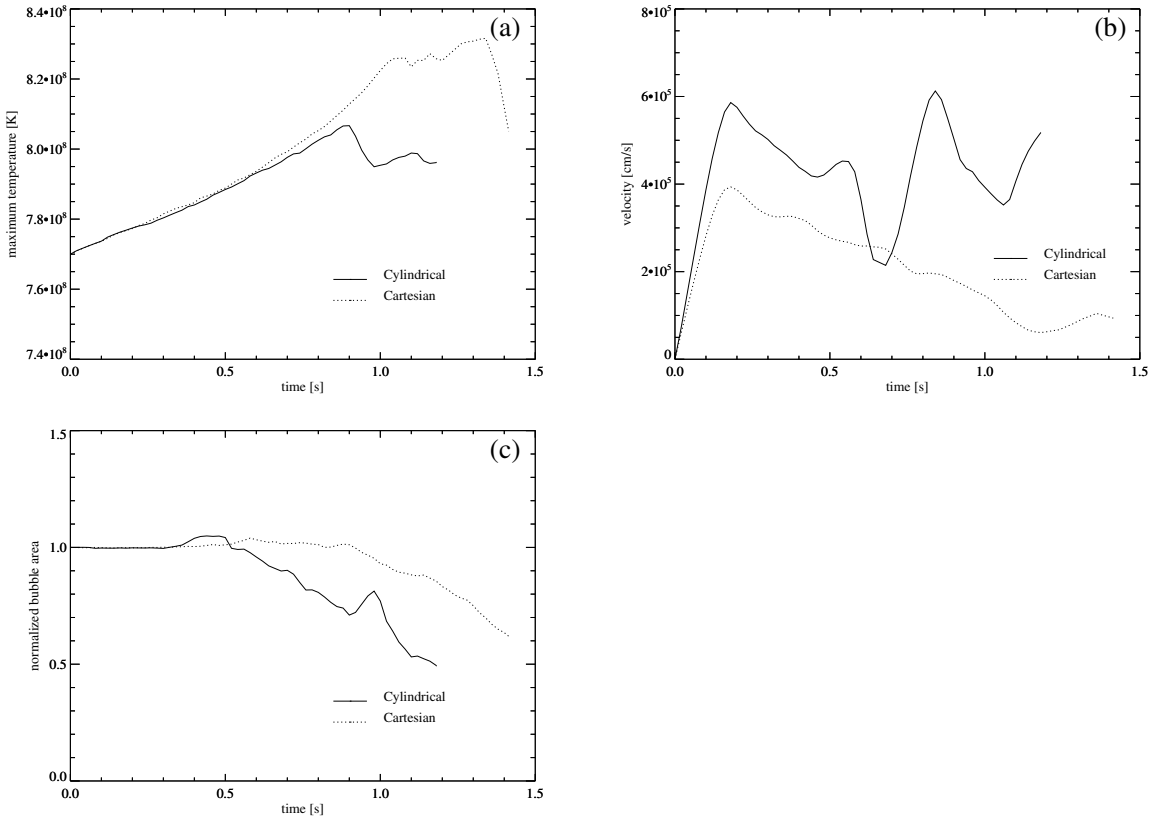

Figure 5.7.: Comparisons of bubble properties as a function of time in simulations with different geometries. *(a)*: maximum bubble temperature. *(b)*: bubble velocity. *(c)*: normalized bubble area.

---

normalized bubble area (see the definition in sect. 6.2) quantifies the effect of the numerical bubble dispersion. The decrease of the area (or of the volume in the cylindrical case) will be discussed elsewhere in detail (sect. 6.3.4). Here the interest is only focused on the comparison between the two geometries that shows that the numerical dispersion affects more the cylindrical calculation.

All the previous arguments lead to choose Cartesian geometry in the bubble simulations:

- The morphological evolutions are different, but in this work the interest is more concentrated in the thermal evolution, which is similar.
- The bubble dispersion is less pronounced in Cartesian geometry. Since this numerical effect should be kept as small as possible (though it does not prevent the discussion of the bubble features, as it will be shown in chap. 6), this is a deciding criterion for the use of this geometry.
- Moreover, Cartesian calculations can be carried out profitably with less spatial reso-

lution and with a larger Courant number than cylindrical ones without suffering any axis effects.

Therefore, this work is based on Cartesian simulations. Additional tests showed that the trends, which will be pointed out for the “Cartesian bubbles”, could be retrieved also in the cylindrical case.

6. Results and discussion

6.1. A list of the performed calculations

The thirteen calculations performed for our parameter study of the bubble physics are listed in table 6.1. They have been carried out within the general setup described in chap. 4 and 5, varying the initial parameters in the following way:

T (bubble temperature): $7.3 - 7.9 \times 10^8$ K.

R (distance from the WD's center): the three values 50, 100, 150 km have been explored.

D (bubble diameter): for the calculation with $T = 7.7 \times 10^8$ K, $R = 100$ km, the three values 0.2, 1, 5 km have been tested.

6.2. Diagnostic quantities

The analysis of the bubble simulations requires to define some quantities which are particularly useful for the interpretation of the results. Some of them have already been used in the discussion of the preliminary tests (chap. 5).

A first difficulty in defining these quantities is the lack of a good criterion about where the bubble is located. This is of course a problem of the Eulerian system of coordinates. Different from the flame propagation problem, here there is no separation, without any ambiguity of definition, between burned and unburned material. In principle, hot material (the bubble is set to be rather hotter than the background) could keep track of the bubble evolution. Unfortunately, the numerical diffusion makes this argument weaker, as it will be shown below. For this reason one cannot make a safe use of "bubble averaged quantities". The description of the thermal evolution of the bubble will be hence done by means of the maximum temperature T.

The bubble's motion is determined mostly by the effective gravitational acceleration (eq. 3.20) which depends on the density profile in the WD and on the temperature contrast between the bubble and its surrounding. For sake of clarity, the calculated profile of the function $g(R)$ is reported in fig. 6.1. It is important to notice that in the zone of the WD where ignition is supposed to take place (R up to $150-200$ km) the absolute value of g is increasing with R. For equal values of $\Delta T/T$ bubbles located at an increasing R experience a growing gravitational acceleration.

R = 50 km *Background = 6.96*	7.3	**7.5**	**7.6**	
R = 100 km *Background = 6.83*	7.3	7.5	**7.7, D = 5 km** 7.7 7.7, D = 0.2 km	**7.9**
R = 150 km *Background = 6.63*	7.3	7.5	7.7	7.9

Table 6.1.: Scheme of the simulations which have been performed for the parameter study. The table reads as follows. In the first column the central distances of the bubbles are given, together with the background temperature of the WD at that distance from the center, in units of 10^8 K. In the other four columns, the simulation are identified by the initial temperature, again in units of 10^8 K. The bubble diameter D is fixed at 1 km unless explicitly specified. Simulations that reach the thermal runaway are in boldface.

A necessary tool for a quantitative evaluation of the numerical diffusion of the bubble is its area. As written above, it is difficult to provide an unambiguous definition of this variable. Test simulations have established that a good criterion is given by the following expression:

$$\mathcal{A}_{\rm bubble} = \sum_{bubble} \mathcal{A}_{\rm zone} \tag{6.1}$$

where the is sum calculated over the zones where $T_{\rm zone} > T_{\rm threshold}$ and the threshold temperature is defined by

$$T_{\rm threshold} = \begin{cases} 0.95 \cdot T_{\rm bubble,ini} & \text{for} \quad T_{\rm bubble,ini} > 7.5 \times 10^8 \text{ K}) \\ 0.96 \cdot T_{\rm bubble,ini} & \text{for} \quad T_{\rm bubble,ini} \leqslant 7.5 \times 10^8 \text{ K}) \end{cases} , \tag{6.2}$$

where $T_{\rm bubble,ini}$ is the initial bubble temperature. The quantity $\mathcal{A}_{\rm zone}$ is geometry dependent. In Cartesian geometry it can be simply identified with the zone area $\mathcal{A}_{\rm zone} = dx \cdot dy$, where dx and dy are the zone sizes in the two directions. In cylindrical geometry, taking into account the underlying axial symmetry,

$$\mathcal{A}_{\rm zone} = \pi \left(x_{\rm r}^2 - x_{\rm l}^2 \right) dy \tag{6.3}$$

where $x_{\rm r}$ and $x_{\rm l}$ are the x coordinates of the right and left zone edge, respectively. $\mathcal{A}_{\rm zone}$ in this case is actually a volume.

As far as the bubble velocity $v_{\rm b}$ is concerned, again it is not clear how to define the motion of an object whose shape changes noticeably during the simulation. A satisfying approach is to define $v_{\rm b}$ as the y-component of the velocity averaged over the zones making part of the bubble "area" according to the previous criterion.

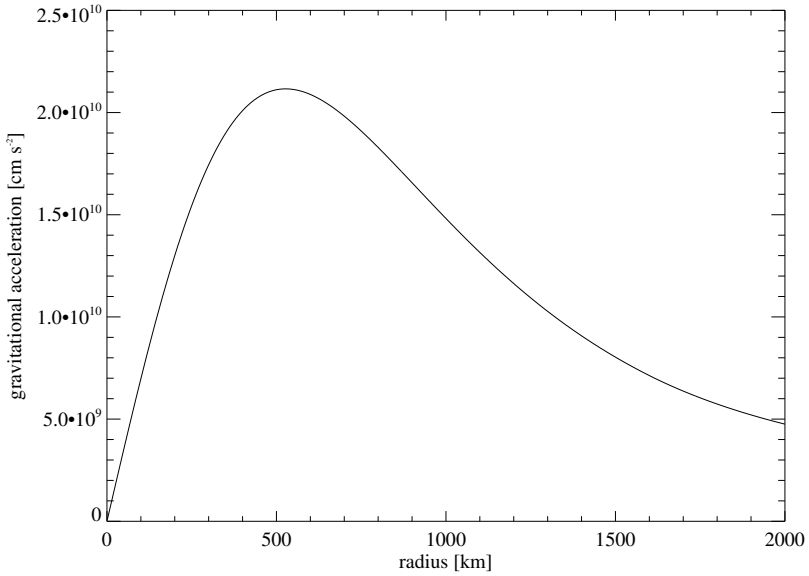

Figure 6.1.: The absolute value of the gravitational acceleration as a function of radius for the 1D WD model used in this work. The acceleration is computed from the density profile of the WD model by using eq. (2.42).

6.3. The physics of the bubble

There is an extended literature on the fluid mechanics of bubbles, both for the used methods and the range of physical parameters in the studied situations. Despite of it, we are not aware of any publication in fluid mechanics, which addresses the peculiarities of the presented setup (degenerate matter, very small density contrasts and nuclear burning), in order to compare the results.

The analysis of the bubble features will hence be focused on astrophysics rather than on fluid mechanics, i.e. on the possible consequences for the ignition process more than on providing a thorough view of the (yet) interesting problem of the bubble evolution. The physical issues which have been theoretically introduced in sect. 3.4.1 will be retrieved in the following parts if needed, adding further details related to the simulations. Most of the discussion will be based on a "reference choice" of the parameters, that is on a simulation with initial temperature $T = 7.7 \times 10^8$ K, initial diameter $D = 1$ km, initial central distance $R = 100$ km. After its detailed evaluation it will be easier to point out the trends which occur by changing the values of the parameters.

6.3.1. Nuclear heating

Hydrostatic carbon burning sets the timescale for the bubble to reach the thermonuclear runaway, the nuclear timescale τ_n (eq. 3.10). It must be stressed that it is the time required

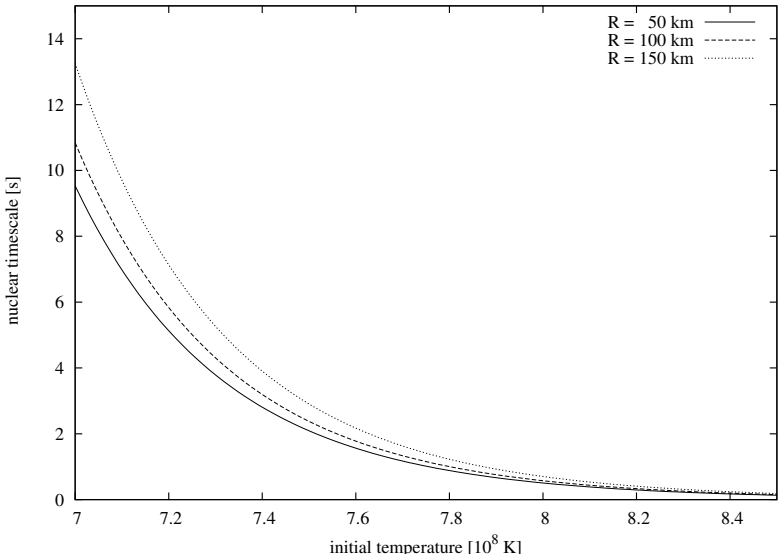

Figure 6.2.: The nuclear timescale is plotted as a function of the bubble temperature according to eq. (6.4). The three lines are for different distances from the WD's center and, thus, different densities.

by an *isolated* region to reach the runaway. This means that, given a WD model with some central temperature, eq. (3.10) does not provide an estimate for the "remaining WD lifetime", because in this case the considered object (the WD center) is not isolated. The heat is carried away from it by the convective motions.

A fit to an analytic expression of τ_n has been found, analogously to eq. 3.10, using the evolutionary timescales of the simulations which reach the runaway (cf. table 6.1) and adding data from further tests. The result is

$$\tau_n \approx 10 \left(\frac{7}{T_8}\right)^{22} \left(\frac{2.5}{\rho_9}\right)^4 \text{ s} \tag{6.4}$$

shown in fig. 6.2. The inferred values of τ_n are in agreement with the derived ones by Woosley et al. (2004).

6.3.2. Adiabatic cooling

According to Woosley et al. (2004), ignition occurs when the integral

$$\int \left[\left(\frac{dT}{dr}\right)_{ad} + \frac{\dot{S}}{C_p v_b}\right] dr \tag{6.5}$$

calculated along the bubble path, diverges. The integral is composed of two terms: the second is linked to the nuclear heating, while the first expresses the adiabatic cooling experienced by the bubble during its rise. An estimate to this term is given by eq. (3.17).

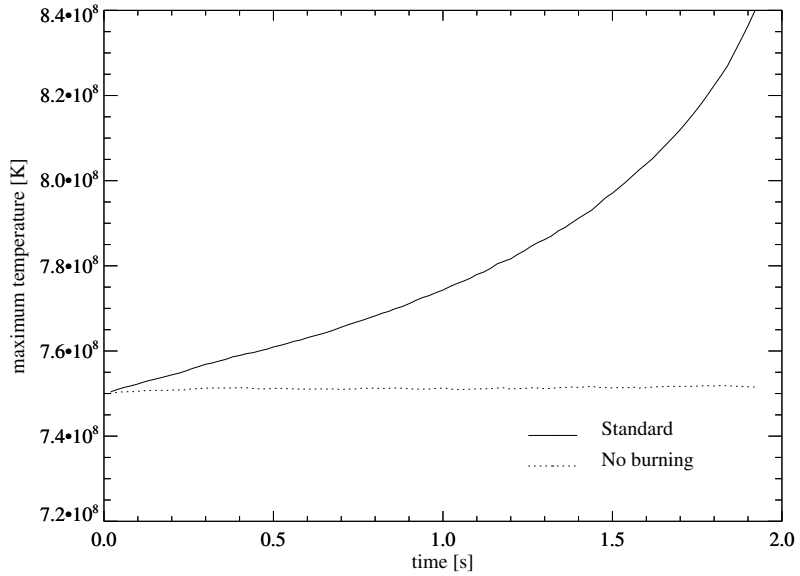

Figure 6.3.: Comparison of the temperature evolution in two simulations. The solid line refers to a calculation whose initial parameters are: $T = 7.5 \times 10^8$ K, $D =$ 1 km, $R = 50$ km. This calculation goes to thermonuclear runaway at $t =$ 2.18 s. Dotted line: Calculation with the same parameters, but with the nuclear burning switched off.

In principle, this effect can be important. Considering the bubble as being embedded in the convective motion, it may travel over a long path comparable with the estimated central distance at ignition, undergoing some cooling. The bubble simulations cannot directly address this physical process. In the described setup the bubble is set at rest and no convective velocities are imprinted in the background. Assuming that in this scheme the bubble travels over a path comparable with its diameter (cf. sect. 6.3.5), multiplying both sides of eq. (3.17) by $r_7 \approx 0.01$ one can realize that adiabatic cooling is negligible in the performed setup. This finding is confirmed by a test simulation (fig. 6.3), similar to the usual setup but with the nuclear burning switched off. The temperature evolution shows that neither heating takes place nor any significant cooling.

6.3.3. Hydrodynamical instabilities

The bubble motion is a special case of the Rayleigh-Taylor instability (in the following, RTI). In a gravitational field with the vector **g** pointing downwards along the y-axis, the hotter and lighter fluid accelerates upwards. For the adopted "reference choice" of the parameters, the morphological evolution of the bubble is presented in fig. 6.4 by a sequence of temperature plots.

In sect. 3.4.1 an analytical expression for the bubble velocity was given, referring to

Layzer (1955). Actually, the problem under investigation in this thesis work is not fully analogous, neither to this reference nor to the other ones cited below in this concern, because the RTI theory has been mainly developed to account for bubbles as growing deformations of planar interfaces between two fluids, and not as finite objects (see, for example, the figures in Glimm & Li 1988 and Li 1996). Nevertheless, especially in the non-linear phase of the RTI, at least the scalings predicted by the theory are confirmed by the results of the simulations, as will be shown in sect. 6.4.

A significant parameter of the problem is the Atwood number At,

$$\mathrm{At} = \frac{\rho_2 - \rho_1}{\rho_2 + \rho_1} \tag{6.6}$$

where ρ_1 and ρ_2 are the bubble and background densities, respectively. The original work of Layzer (1955) is based on the case $\mathrm{At} = 1$ (bubble density negligible with respect to the background). The original form of eq. (3.21) obtained in this case is $v_\mathrm{b} = c_1 \sqrt{g\,D/2}$. This result has been generalized by Taylor (1950) for non-zero density of the lighter fluid (i.e. $\mathrm{At} \neq 1$) with the scaling $g \to \mathrm{At}\, g$:

$$v_\mathrm{b} = c_1 \sqrt{\frac{\mathrm{At}\, g\, D}{2}}\ . \tag{6.7}$$

In our bubble problem, the density contrast is very small because of the degeneracy of the WD matter (see fig. 6.5, left). For $\rho_1 \approx \rho_2$, eq. (3.20) leads to $g_\mathrm{eff} \approx 2\,\mathrm{At}\, g$ which by substitution brings back eq. (6.7) to the form of eq. (3.21), chosen for a direct comparison with eq. (2.52) in sect. 3.4.1.

With a different approach to the limit[1] $\mathrm{At} \to 0$, the expression $v_\mathrm{b} \simeq c_1 \sqrt{2\,\mathrm{At}\, g\, D/4}$ is consistent with the alternative formula for the terminal velocity of a nonlinear, single-mode RTI, proposed by Goncharov (2002) and being valid for an arbitrary density contrast:

$$v_\mathrm{b} = \sqrt{\frac{2\mathrm{At}}{1+\mathrm{At}}\,\frac{g}{Ck}}\ , \tag{6.8}$$

where $k \sim 2\pi/(D/2)$ is the wavenumber of a perturbation of size of order of the bubble radius $D/2$, and C is a numerical constant whose value is 3 in 2D and 1 in 3D. The velocity provided by this last expression is about 1.5 times smaller than the result of eq. (3.21). As pointed out by Abarzhi et al. (2003), eq. (6.8) implies a gravity scaling different from eq. (6.7):

$$g \to g\,\frac{2\mathrm{At}}{1+\mathrm{At}} = g\,\frac{\rho_2 - \rho_1}{\rho_2} = g_\mathrm{eff} \tag{6.9}$$

[1] $\mathrm{At} \approx 4.3 \times 10^{-4}$ with the reference set of initial parameters. It is not clear how to perform an effective estimate of ρ_1 and ρ_2, even at $t = 0$. The densities are not locally constant, both inside and around the bubble. Therefore At is evaluated by taking the density values close to the y-coordinate of the bubble center.

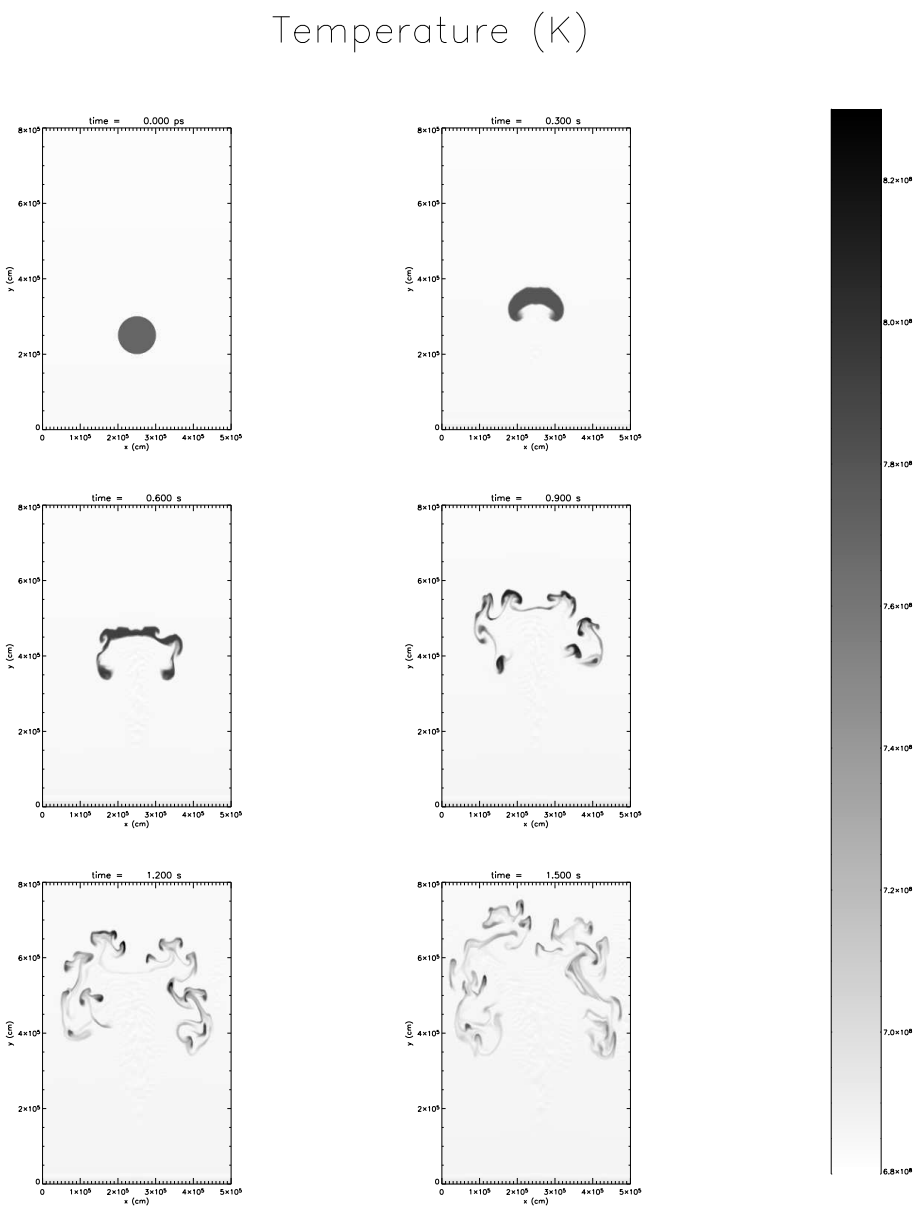

Figure 6.4.: Series of temperature plots, showing the evolution of a bubble in a simulation with the initial parameters $T = 7.7 \times 10^8$ K, $D = 1$ km, $R = 100$ km. Different from fig. 5.6, the presented simulation has five levels of refinement and the bubble evolution is shown till the late, dispersed phase.

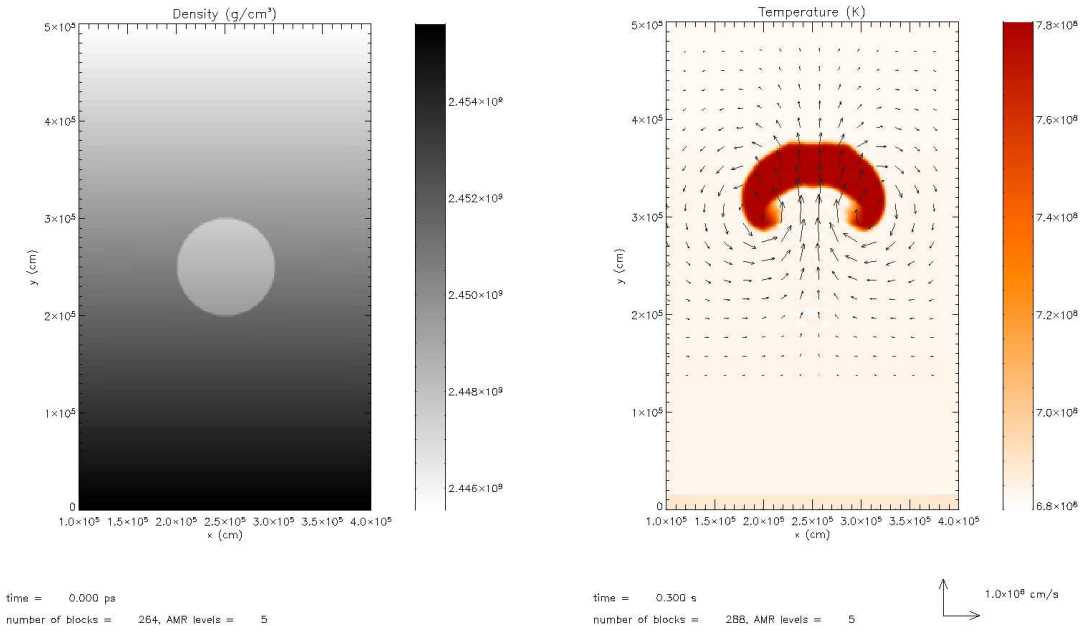

Figure 6.5.: Left: density plot at $t = 0\,\mathrm{s}$, centered on the bubble. The figure refers to the simulation described in fig. 6.4. Right: The velocity field is superimposed to the temperature plot at $t = 0.3\,\mathrm{s}$.

in agreement with eq. (3.20).

From eq. (6.8) one gets, for the reference choice of parameters, $v_\mathrm{b} \simeq 1.3 \times 10^5\,\mathrm{cm\,s^{-1}}$. The comparison with the velocity plot of fig. 5.7 *(b)* shows a trend of $v_\mathrm{b}(t)$ towards this value even if the morphology evolution of the bubble prevents a more quantitative analysis.

The RTI causes the disruption of the bubble, as clearly depicted in fig. 6.4. An approximate estimate for the timescale of this process can be given by

$$\tau_\mathrm{RTI} = \frac{D}{v_\mathrm{b}} \tag{6.10}$$

which, with the reference values of the parameters and the use of eq. (6.8), gives a timescale of about 0.8 s, a sort of "bubble lifetime", to be compared with the morphological behavior shown in fig. 6.4. Besides the RTI one can see the arise of the Kelvin-Helmholtz instability, caused by the shear flow at the sides of the bubble. This is particularly evident at high resolution (cf. fig. 5.2).

Following the same approach as Robinson et al. (2004), one could consider another effect linked to the RTI, namely the role of the vortical motions, induced by buoyancy (fig. 6.5, right), in tearing apart the bubble. The timescale associated to this "rise dispersion" is the

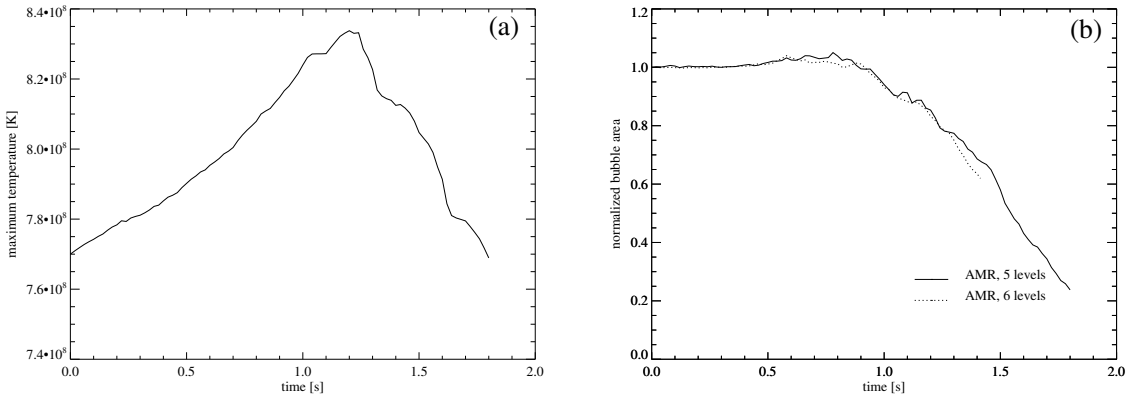

Figure 6.6.: Evolution of diagnostic quantities, in the simulation performed with the reference choice of parameters. *(a)*: maximum bubble temperature. *(b)*: normalized bubble area, with a comparison among simulations with different levels of refinement.

time that it would take for the bubble to travel along a path comparable to its diameter, given the acceleration $g_{\rm eff}$:

$$\tau_{\rm D} = \sqrt{\frac{2D}{g_{\rm eff}}}\,, \tag{6.11}$$

which means, for the reference choice of parameters, $\tau_{\rm D} \simeq 0.2\,{\rm s}$. In the bubble problem $\tau_{\rm RTI} > \tau_{\rm D}$. Different from the physics context of Robinson et al. (2004) (cooling flows in galaxy clusters), here the disruption does not occur on $t \sim \tau_{\rm D}$. This timescale can be thus understood as marking the phase when the bubble loses noticeably its circular shape (cf. also fig. 5.6) while, as already pointed out, a suitable timescale for bubble breakup is provided by $\tau_{\rm RTI}$ (see sect. 6.3.5 for a detailed discussion).

6.3.4. Numerical dispersion

Because of the instabilities, the bubble undergoes a *physical* dispersion, described in the last section. The typical length scale of the bubble pieces decreases in time, and it is not trivial to characterize the details of this process, hindered by the spatial resolution of the simulations.

From a physical point of view, one can expect that the dispersion goes on until the typical length scale of a bubble part is comparable with the minimum size $\lambda_{\rm min}$, introduced in sect. 3.4.1. For pieces whose size is larger than $\lambda_{\rm min}$, the nuclear heating is larger than the heat loss by conduction. These pieces increase their temperature (in this phase, in principle, they can still reach $10^9\,{\rm K}$ and trigger the thermonuclear runaway), until their typical size, by dispersion, decreases to $\lambda_{\rm min}$. Then they begin cooling down. Considering this effect in

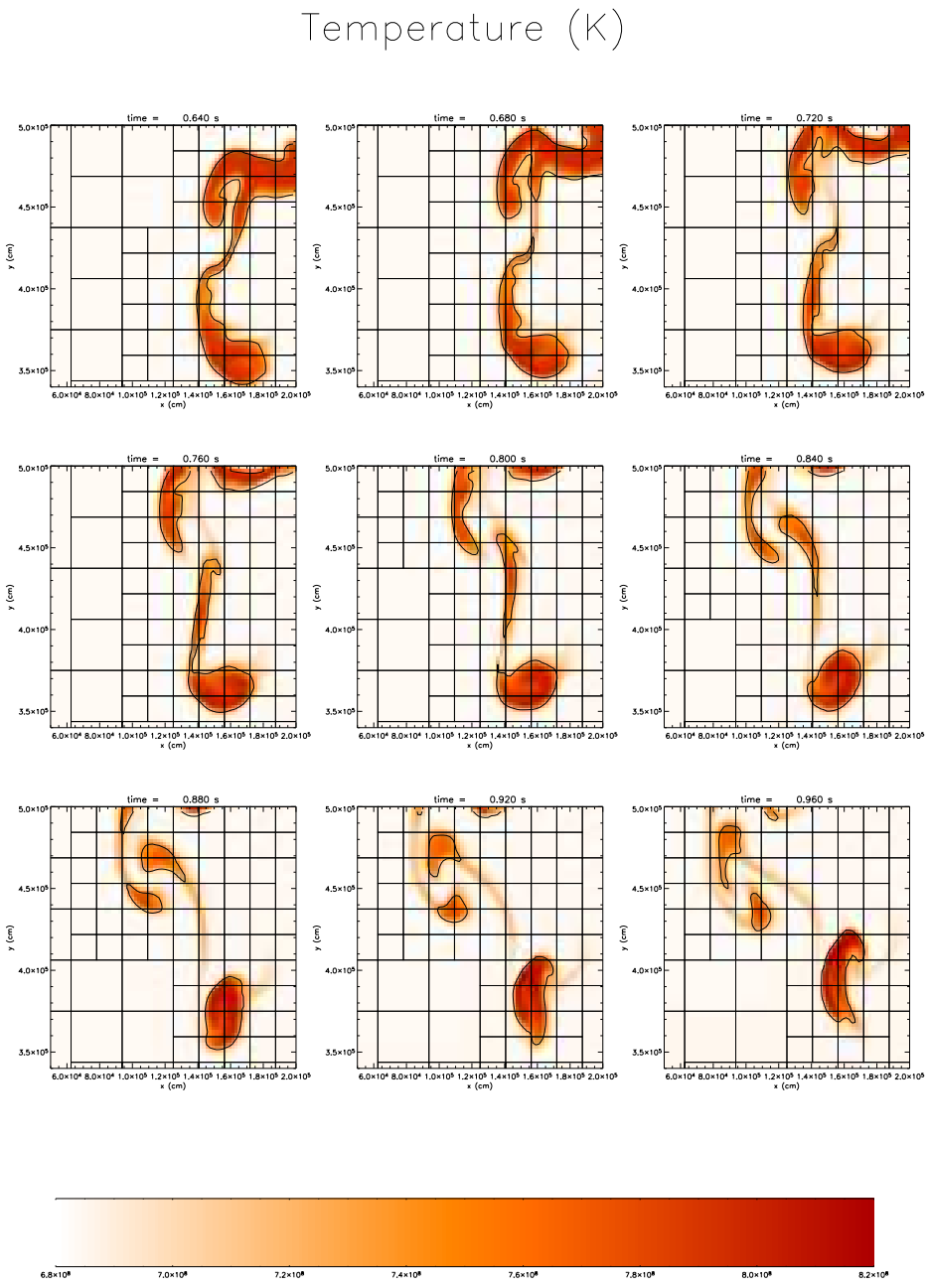

Figure 6.7.: Series of temperature plots referring to the same simulation as fig. 6.4, showing the evolution of a bubble detail. The grid mesh (recalling that a square corresponds to 8×8 computational zones) is shown and the contours in the plots mark the bubble area, according to the definition of sect. 6.2.

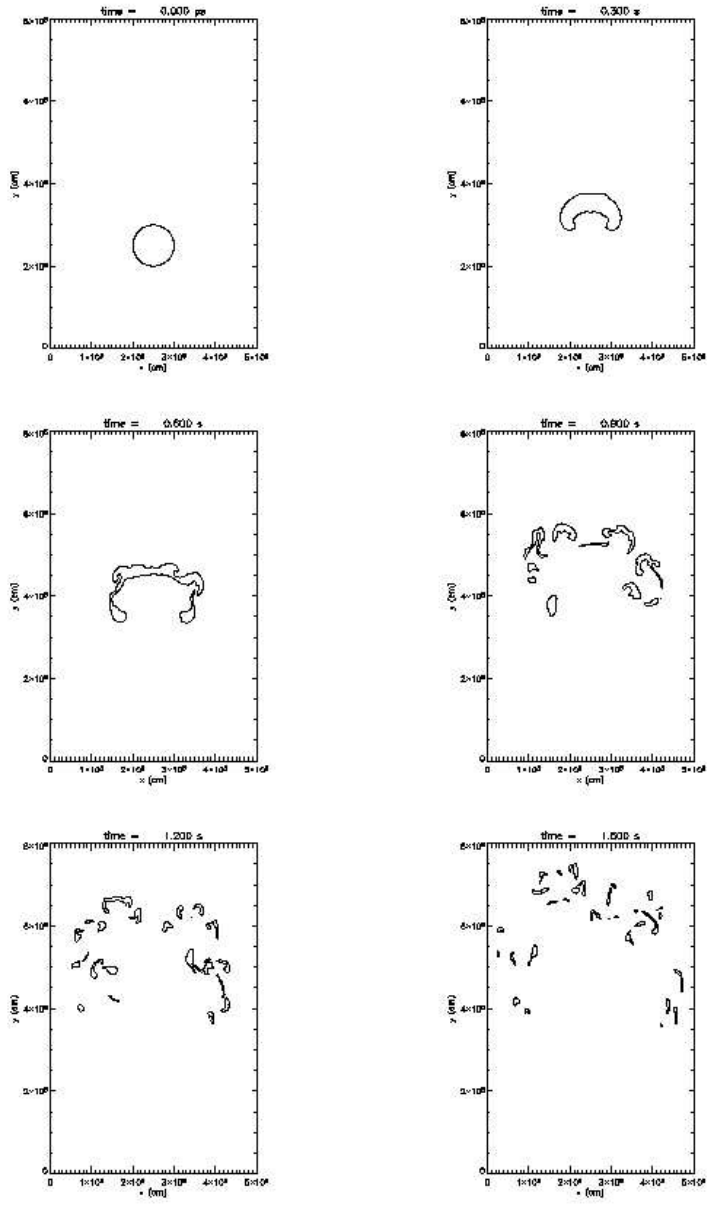

Figure 6.8.: The same simulation as fig. 6.4, but with the contours in the plots indicating the bubble area.

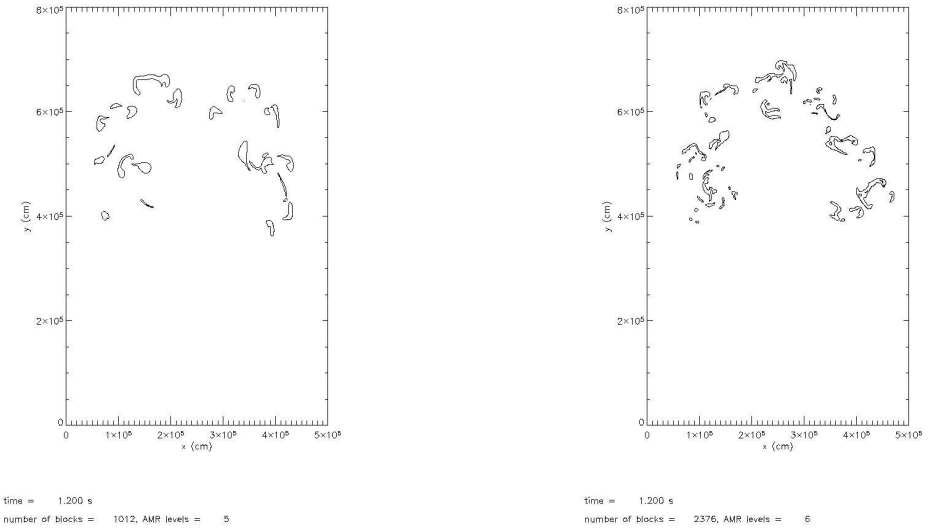

Figure 6.9.: Comparison of the morphology of the bubble area at $t = 1.2$ s. The two contour plots refer to simulations with the reference choice of the initial parameters, but with different levels of refinement.

the bubble globally, the trend of the maximum temperature shown in fig. 6.6, left, can be easily interpreted: the bubble is heated until either the runaway occurs (cf. fig. 6.3) or the dispersion prevails. The decrease of the bubble area (fig. 6.6, right) is logically consequent.

One must notice however that the length scale for the dispersion driven by heat conduction, as estimated from eq. (3.18), is somewhat smaller than 10^2 cm, i.e. much smaller than the spatial resolution of the simulations (2×10^3 cm). $\lambda_{\min}$ is actually so small that a direct simulation to that scale, even with AMR, is not feasible at all computationally. What is actually observed in the bubble simulations is not a physical, but a *numerical* dispersion. Figure 6.7 further helps to clarify this important point. The plots are focused on a small detail, a sort of "bridge" linking the top of the bubble with a lower vortical structure. This detail becomes thinner and, as its width is approximately 2-3 times the spatial resolution, it cools off unphysically. It is thus lost from the bubble area according to the definition in sect. 6.2.

Because of the explicit dependence of the spatial resolution on the length scale, one could suppose that this numerical dispersion is dependent in resolution. Surprisingly, the area evolution shown in fig. 6.6, right, does not show any significant dependence of the bubble area decrease on the level of refinement of the simulation. Probably, this happens because the hydrodynamical instabilities in the more resolved calculation produce structures that are globally more numerous and smaller in size (fig. 6.9). The connection between the numerical dispersion and the temperature decrease explains also the choice of simulating isothermal bubbles. Every other temperature profile would have accelerated the disruption of the coldest bubble parts (and made it more difficult to define the bubble area).

6.3.5. Motion and evolution of the bubble

As shown in the reference calculation (fig. 6.4), and confirmed in all the calculations of this parameter study, the bubbles that have been simulated travel over a path of a few kilometers, comparable with their size. The velocities are of the order of some km s^{-1}. Apparently, from these data it would seem that the bubble evolution occurs mostly in place. Actually this is not true because the bubbles are carried inside the WD by the convective motions, whose velocity is much larger than the buoyant bubble velocity.

In order to sum up the most significant informations which have been introduced in the last section, the following overview points out the main items and the related timescales about the bubble evolution:

- The initial bubble temperature determines the nuclear timescale (eq. 6.4). Physically, this is the upper limit for the duration of the bubble evolution. It is lengthened eventually because of the cooling by adiabatic expansion, but it is not possible to quantify this last contribution from the presented simulations that neglect it.

- The bubble is disrupted during its motion by the RTI approximately on timescales given by eq. (6.10). The dispersion proceeds down to the length scales where the heat conduction is effective in dissipating the energy generated by nuclear burning.

- The discussion of the bubble physics is not complete without an evaluation of the role of the numerical dispersion. It is not possible to quantify exactly the whole duration of the physical dispersion phase described previously because this process can be followed in the simulations only partially until the typical length scale of the bubble substructures are comparable to 2-3 times the spatial resolution.

The competition between nuclear heating and dispersion is the key to understand the outcome of the bubble evolution and, consequently, also to the ignition process of SNe Ia. The analytical studies on the ignition driven by floating bubbles (García-Senz & Woosley 1995, Woosley 2001, Woosley et al. 2004, Wunsch & Woosley 2004) have not explored the bubble dispersion by the RTI. About this subject, an interesting question is to understand when the burning or the dispersion prevails, depending on the initial bubble parameters.

A further definition is useful for clarification. Let $\lambda(t)$ be the typical length scale of the bubble fragments at time t in the simulation. The dispersion process is followed correctly in the simulations until a time t_1, with $\lambda(t_1) = (2-3)\,dx$, where dx is the spatial resolution of the simulation. Physically, the dispersion continues until t_2, with $\lambda(t_2) = \lambda_{\min}$ (eq. 3.18). What is the interval $t_2 - t_1$? What happens to the bubble during this interval?

About the second question it has been stressed that the performed simulations, affected by numerical dispersion, overestimate the cooling linked to the bubble disruption. From a physical point of view one thus expects that the bubble temperature could increase for a longer time than it is shown, for example, in fig. 6.6 *(a)*. The point is then, whether or not $t_2 - t_1$ is sufficient for the bubble to go to runaway.

A theoretical expression for the dispersion evolution $\lambda = \lambda(t)$ cannot have been retrieved from literature. From a qualitative analysis of the bubble morphology in the simulations, a rough estimate says that $t_2 - t_1$ should not be larger than τ_{RTI}.

For a more detailed evaluation of the timescales two further contributions have to be introduced. The first is the turbulence in the background, presented in the following of this section. The second one is the effect of the bubble rise driven by fast convective motions. This will be discussed after the parameter studies of the next section when the problem of the bubble evolution is reprised on the basis of the observed trends.

Background turbulence

In all performed bubble simulations the background state of the WD was assumed to be "quiet", in accordance with the definition of hydrostatic equilibrium. As discussed in sec. 2.2, the convective flow in the WD prior to runaway is turbulent. The integral scale L at which the energy is injected is comparable with the pressure scale height (eq. 2.47), about 450 km (Woosley 2001). The typical velocity at that scale is the convective velocity, estimated to be about $50 - 100\,\mathrm{km\,s^{-1}}$. Assuming a value of $70\,\mathrm{km\,s^{-1}}$, the theory of turbulence predicts through eq. (2.21) that the typical velocity at the length scale of the spatial resolution of the simulations is about $v_{\mathrm{turb}} = 2.5\,\mathrm{km\,s^{-1}}$. The FLASH code implements a stirring module, based on the prescription of Eswaran & Pope (1988), described in the FLASH manual (available at `http://flash.uchicago.edu/website/codesupport/-users_guide/docs/FLASH2.3/flash2.3_ug.pdf`).

The purpose of the following test is not meant to be a quantitative analysis of turbulence, but rather it introduces a divergence-free velocity field in the simulations to study qualitatively the effect of such stirring on the evolution of the bubble. Stirring is very "expensive" on a computational point of view (it increases the computation time by more than 200%). Thus it was not used extensively in our parameter study.

In the test, the parameters of stirring module of the FLASH code were arranged appropriately in order to get typical velocities in the WD background of the same order of magnitude as v_{turb} derived above. Figure 6.10 shows that the stirred background accentuates the bubble dispersion. This is also confirmed by the analysis of the timescales of temperature evolution (fig. 6.11 *(a)*) and area decrease (fig. 6.11 *(b)*). The amount of the decrease of the dispersion timescale is not so important since this test only aimed of showing that a more realistic background has some effect on the bubble evolution. In our example, the timescale of dispersion of the bubble was shortened to a few times 10^{-1} s.

6.4. The parameter study

After having discussed the features of the bubble evolution for a standard calculation, the impact of each parameter on the bubble physics will be evaluated by comparing different simulations performed with varying values of the quantity under consideration.

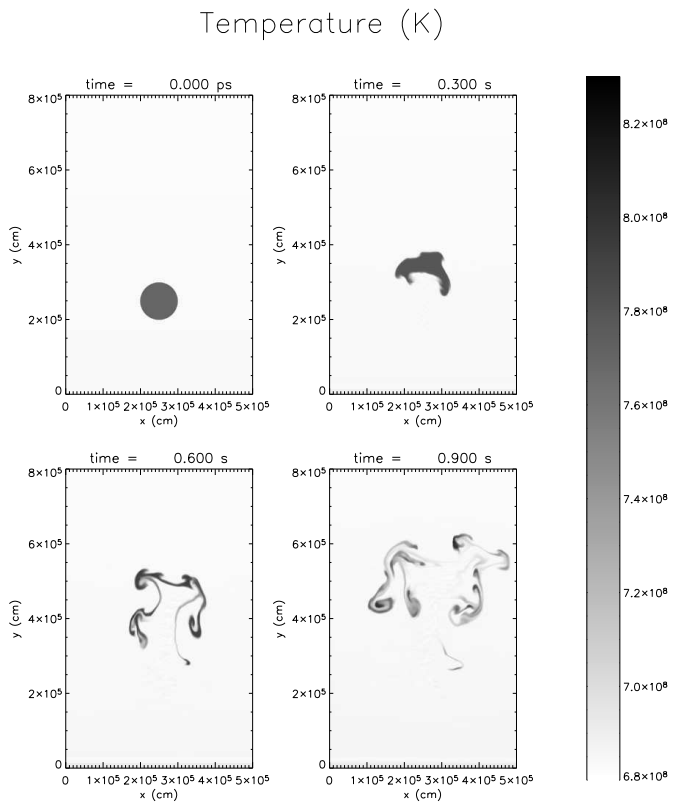

Figure 6.10.: Series of temperature plots, showing the evolution of a bubble in a simulation with stirring. The reference choice of initial parameters is adopted.

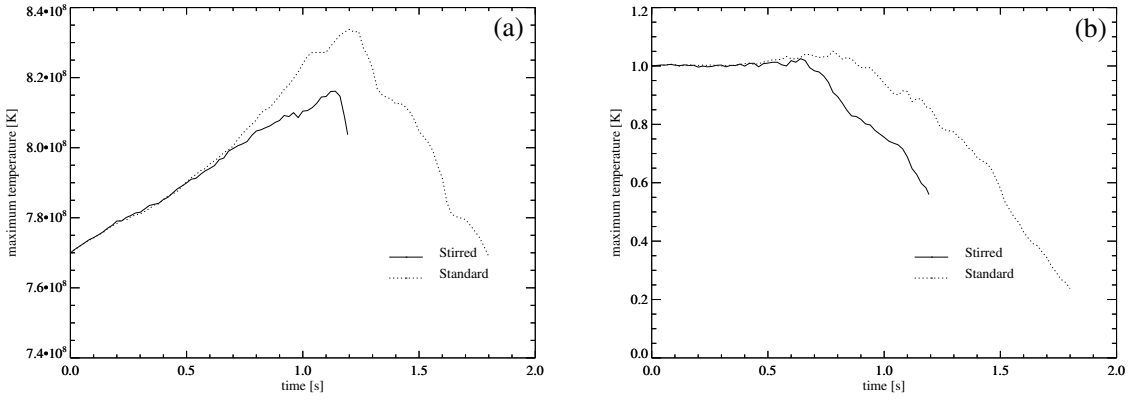

Figure 6.11.: Evolution of maximum bubble temperature *(a)* and normalized bubble area *(b)* in the simulation with stirring. The quantities are plotted in comparison with the analogous time evolution in the case without stirring.

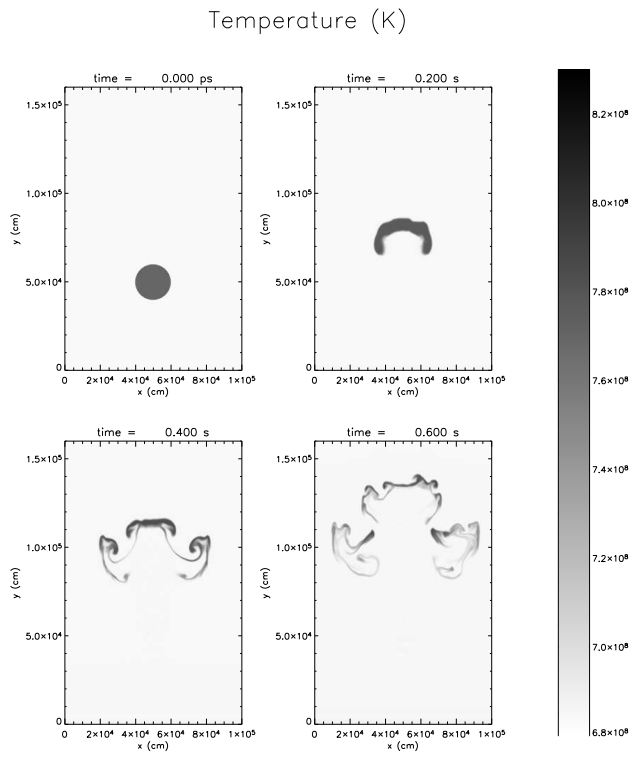

Figure 6.12.: Series of temperature plots, showing the morphological evolution of the bubble in the simulation with $T = 7.7 \times 10^8$ K, $R = 100$ km and $D = 0.2$ km.

6.4.1. The effect of the bubble diameter D

As outlined in table 6.1, the role of different bubble diameters was studied on the base of three calculations, with initial parameters $T = 7.7 \times 10^8$ K and $R = 100$ km. The initial diameter D was varied by a factor of five above and below the reference value, i.e. $D = 0.2$, 1 and 5 km. The extent of the computational domain and the spatial resolution were scaled accordingly in order to resolve the bubble initially by an identical number of zones. Figures 6.12 and 6.13 show the evolution of the calculations with $D = 0.2$ and 5 km respectively, while fig. 6.14 presents a comparison of maximum temperature and normalized bubble area.

According to the discussed bubble physics, the bubble diameter affects the dispersion timescales. Indeed, the RTI timescale (eq. 6.10) scales as $D^{1/2}$ since, from eq. (6.8), $v_b \propto D^{1/2}$ as well. This scaling is nicely confirmed by the comparison of the area evolution in fig. 6.14 *(b)*. Assuming that for the simulation with $D = 1$ km the area-decrease starts approximately at $t = 0.8$ s, one can see that for the bubble with $D = 0.2$ km the analogous decrease starts approximately at $t = 0.8 \cdot (0.2/1)^{1/2} \simeq 0.35$ s.

For the same reason, the bubble with $D = 5$ km has a larger τ_{RTI}. Since the nuclear

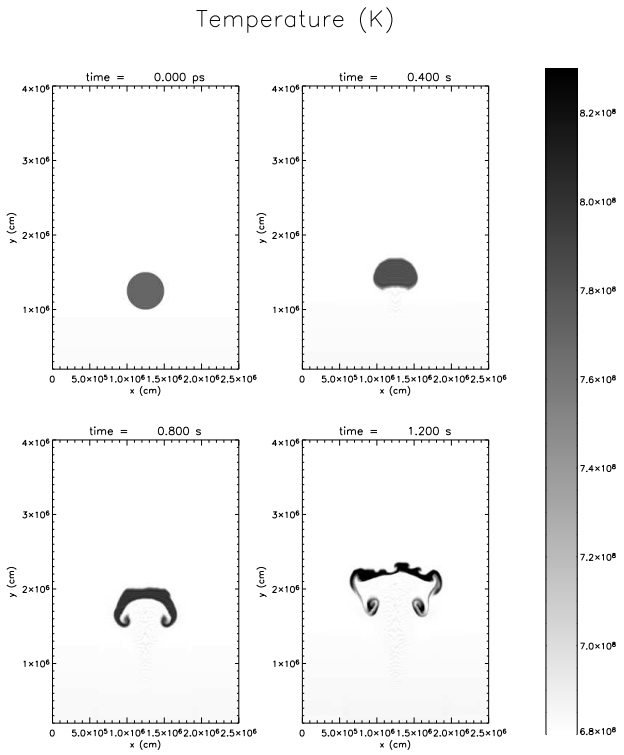

Figure 6.13.: The same as fig. 6.12, but with $D = 5\,\mathrm{km}$. The last plot refers to $t = 1.2\,\mathrm{s}$. Note the difference of timescales with respect to fig. 6.12.

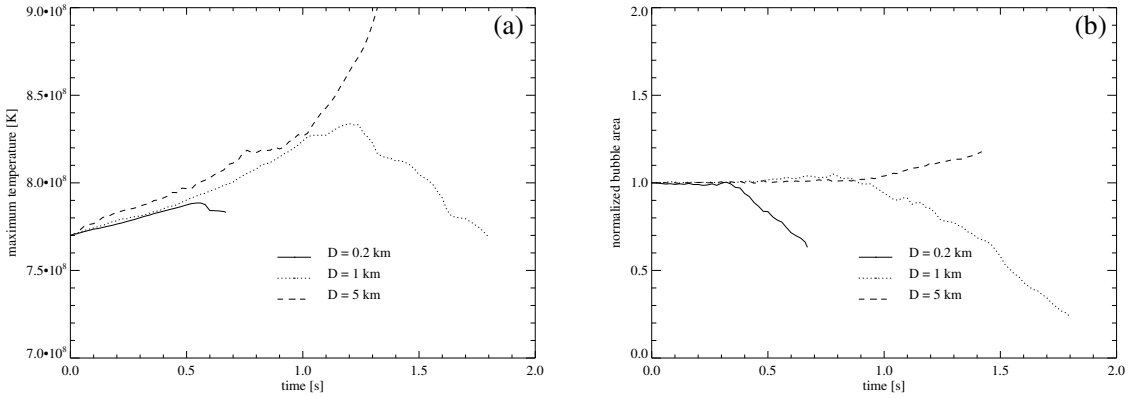

Figure 6.14.: Comparison of the evolution of maximum temperature *(a)* and normalized bubble area *(b)* in simulations with $R = 100\,\mathrm{km}$, $T = 7.7 \times 10^8\,\mathrm{K}$ and D indicated in the legends.

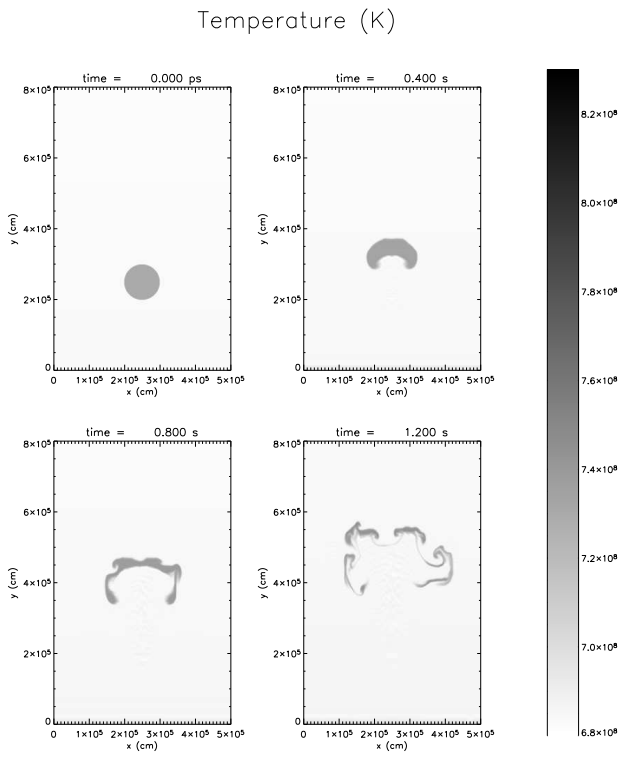

Figure 6.15.: A series of temperature plots showing the morphological evolution of the bubble in the simulation with $T = 7.3 \times 10^8$ K, $R = 100$ km and $D = 1$ km.

timescale does not depend on the bubble diameter, in this case it results $\tau_{\mathrm{RTI}} > \tau_{\mathrm{n}}$, and the bubbles goes to runaway.

From this study, one can conclude that the evolution of bubbles with larger diameter is favored. However, this statement has to be completed with the finding of Woosley et al. (2004), who put an upper limit ($D \lesssim 1$ km) on the bubble diameter because of turbulent dispersion (cf. sect. 3.4.1). This issue will be discussed in sect. 6.5.1.

6.4.2. The effect of the bubble temperature T

Probably the initial temperature T is the most interesting parameter because its role in the bubble physics is manifold. As shown in table 6.1, several values have been tested. For sake of simplicity, a discussion will only be presented for the simulations with $R = 100$ km, $D = 1$ km and T ranging from 7.3 to 7.9×10^8 K, keeping in mind that the inferred trends are valid also for calculations with other central distances. The morphological evolution of the

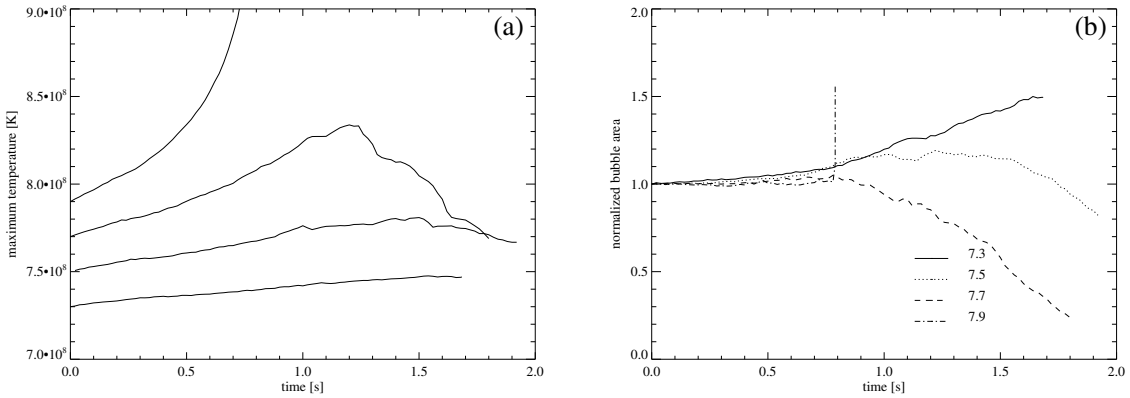

Figure 6.16.: *(a)*: Comparison of temperature evolution in simulations with $R = 100\,\mathrm{km}$, $D = 1\,\mathrm{km}$ and T which can be read on the y axis at $t = 0$. *(b)*: Comparison of the normalized bubble area. The initial bubble temperatures are indicated in the legend, in units of $10^8\,\mathrm{K}$.

bubble in simulations with the extreme values of T is shown in fig. 6.15 and 6.17. Fig. 6.16 presents a comparative analysis of temperature and area.

The nuclear timescale depends on the bubble temperature in a rather steep way (eq. 6.4). Also the dispersion timescale τ_{RTI} depends implicitly on T, approximately via the square root of Atwood number At (cf. eq. 6.8). At varies in the explored temperature range from $2.2{\times}10^{-4}$ ($T = 7.3{\times}10^8\,\mathrm{K}$) to $5.3{\times}10^{-4}$ ($T = 7.9{\times}10^8\,\mathrm{K}$). In simpler terms, the temperature contrast between the bubble and the surrounding material is linked to the density contrast and hence to the effective gravitational acceleration. With equal background temperature (i.e. equal central distance R) hotter bubbles experience larger acceleration and thus faster dispersion. On the other hand, the nuclear timescale decreases even faster with temperature. This indicates the existence of a threshold temperature above which a bubble goes into runaway. At $R = 100\,\mathrm{km}$ the threshold is found to be approximately $T = 7.9 \times 10^8\,\mathrm{K}$.

The comparison between fig. 6.15 and 6.17 shows clearly the different evolutionary timescales of the bubbles. In the case with $T = 7.3 \times 10^8\,\mathrm{K}$ they are so long, that the simulation was stopped before reaching full dispersion. Moreover, it seems unlikely that such a bubble can ignite after $t \simeq 4\,\mathrm{s}$ (cf. fig. 6.2) without being dispersed in the meanwhile, by the RTI or other effects (see sect. 6.5.1).

A confirmation of the expected dependence of the dispersion timescale on $\mathrm{At}^{1/2}$ can be retrieved from the comparison of the temperature evolution of the calculations with $T = 7.7$ and $7.5 \times 10^8\,\mathrm{K}$. The time of maximum temperature τ_{max} indeed depends on the dispersion timescale. Starting from $\tau_{\mathrm{max}}(7.7) \simeq 1.2\,\mathrm{s}$,

$$\tau_{\mathrm{max}}(7.5) \simeq \tau_{\mathrm{max}}(7.7)\left(\frac{\mathrm{At}(7.7)}{\mathrm{At}(7.5)}\right)^{1/2} \simeq 1.2 \cdot \left(\frac{4.3\times10^{-4}}{3.3\times10^{-4}}\right)^{1/2} \approx 1.4\,\mathrm{s}\,, \tag{6.12}$$

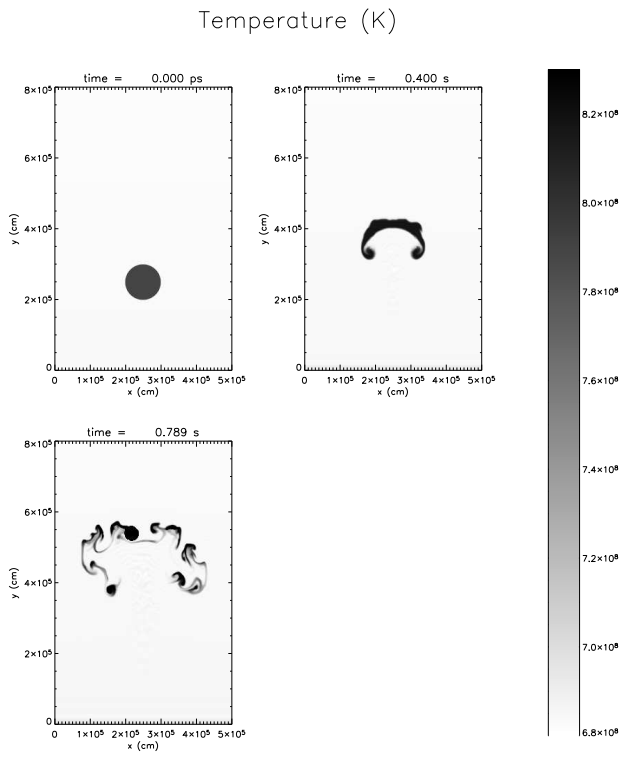

Figure 6.17.: The same as fig. 6.15, but with $T = 7.9 \times 10^8$ K. The hot spot at $t = 0.789$ s indicates that the thermonuclear runaway was reached in the simulation.

as one can read from fig. 6.16 *(a)*, consistent with the large temperature peak of the calculation with $T = 7.5 \times 10^8$ K.

We preferred to perform this estimate on the evolution of temperature, rather than on the area. The latter is more difficult to be interpreted because of the tendency to a moderate expansion of the coldest bubbles. In the WD the pressure is decreasing outwards, so a rising bubble has to adjust its internal pressure by expansion. This effect is evident only in the simulations with the lowest temperatures, where the bubbles disperse slowly. In the hottest bubbles the expansion is probably masked by the faster disruption and is not visible.

6.4.3. The effect of the central distance R

While the parameter T was shown to be the most interesting one for the bubble physics, the central distance R is probably most relevant for the ignition theory of SNe Ia.

As already explained in sect. 3.4, placing a bubble at some distance R from the WD's center and letting it rise, is a useful approximation only, because the convective velocity is

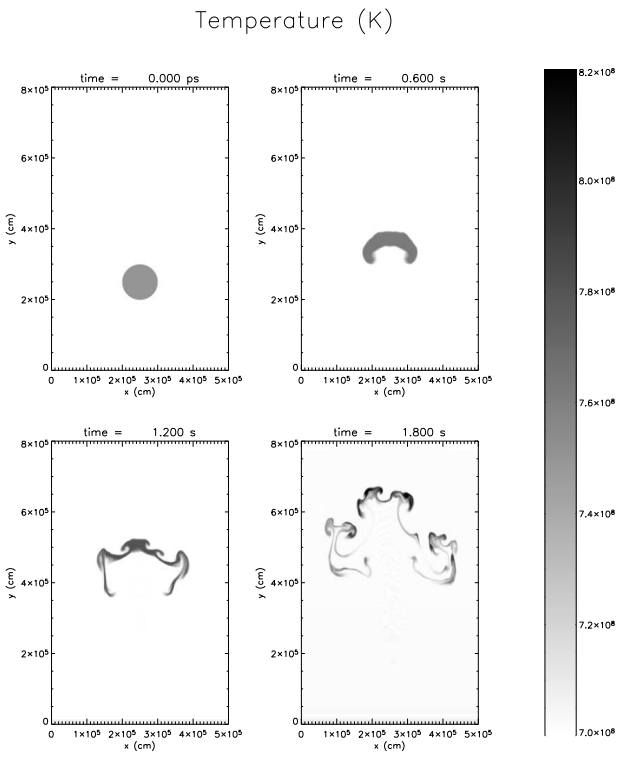

Figure 6.18.: Series of temperature plots showing the morphological evolution of the bubble in the simulation with $T = 7.5 \times 10^8$ K, $D = 1$ km and $R = 50$ km. The thermonuclear runaway is reached at $t = 2.182$ s.

always much larger than the simulated buoyant velocity. Nevertheless, a study of bubbles at different R can provide interesting hints on the evolution of these objects during their rise, while they are embedded in the convective motions and can reach central distances which are in the explored range. The analysis was performed by comparing three simulations with the initial parameters $T = 7.5 \times 10^8$ K, $D = 1$ km and R equal to 50, 100 and 150 km.

The increase of R in the calculations affects the effective gravitational acceleration for two reasons. First, the modulus of the acceleration $g(R)$ increases with R in the considered range of distances as shown in fig. 6.1. Second, the temperature profile of the WD is decreasing (the background temperatures at various R are given in table 6.1). So at equal bubble temperature, the temperature (and density) contrast is increasing with R. This implies that the effective gravitational acceleration increases outwards, too.

This effect is evident dramatically in the comparison between the timescales of the two extreme cases, $R = 50$ (fig. 6.18) and 150 km (fig. 6.19), and from the analysis of fig. 6.20. The simulation with $R = 50$ km goes to thermonuclear runaway. Its area evolution shows an

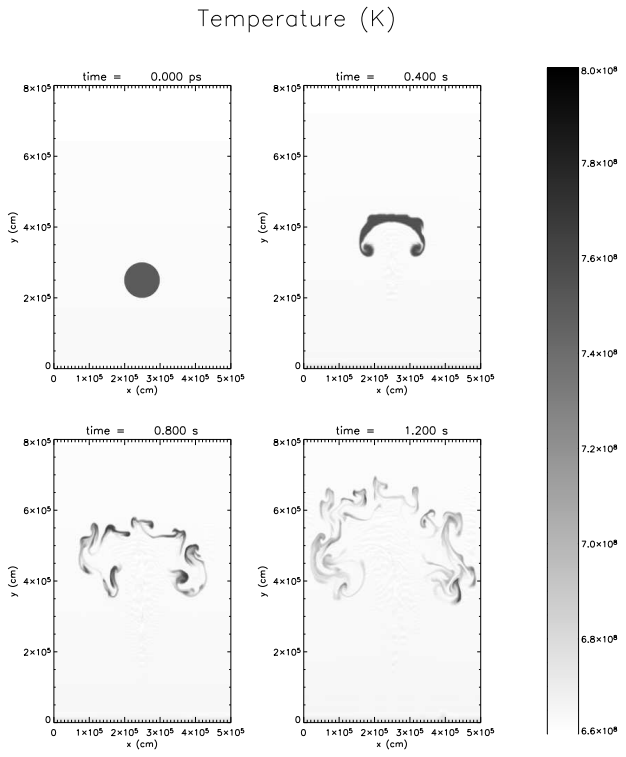

Figure 6.19.: The same as fig. 6.18, but with $R = 150$ km. Note the different timescales of the two simulations.

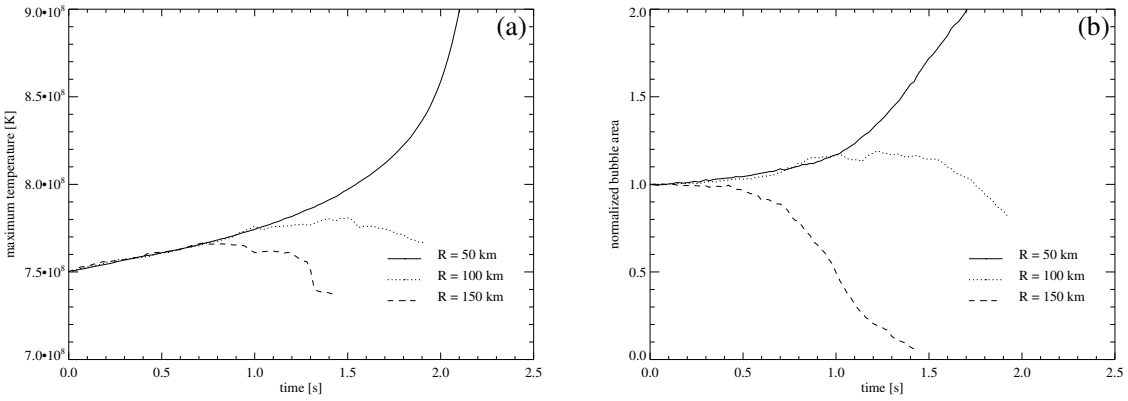

Figure 6.20.: Comparison of the evolution of maximum temperature *(a)* and normalized bubble area *(b)* in simulations with $T = 7.5{\times}10^8$ K, $D = 1$ km and R indicated in the legends.

expansion (partly due to a problem of the definition of "bubble area" when the temperature contrast between the bubble and the background is relatively small). On the other hand, as predicted the dispersion timescales of the other simulations are noticeably shorter as R increases.

The role of the increasing g_{eff} is relevant also for the value of threshold temperature at which the bubbles at different R go into runaway. As shown in table 6.1, the bubble at $T = 7.5 \times 10^8$ K reaches the ignition temperature during the simulation with $R = 50$ km, but with $R = 150$ km even the bubble at $T = 7.9 \times 10^8$ K is dispersed before reaching the runaway.

6.5. Discussion

6.5.1. Summary and closing remarks on the physics of rising burning bubbles

One of the most striking differences between the performed simulations here and the first analytic study on bubble evolution by García-Senz & Woosley (1995) is that the latter does not take into account the dispersion of the bubbles. Consequently, in their work the bubble velocity and the path covered during its rise are very large (cf. sect. 3.4.2). Neglecting the bubble dispersion, this can be explained easily from the physics of buoyancy. The more the bubble moves outwards, the larger is the temperature contrast and thus the effective gravitational acceleration. Moreover, the rise times are rather long, up to about 25 seconds. Also in the present study the bubbles are supposed to move outwards with velocities up to 100 km s^{-1}, important for the definition of the extent of the burning zone, but these velocities can only be obtained through motions driven by convection, not as a rise due to buoyancy. The extent of the ignition zone will be discussed in the next section.

The discussion about the bubble motion at sect. 6.3.5 can be extended here with the results from the parameter study. The most important findings are:

- From considerations about dispersion, large values of the bubble diameter D are favored for the runaway. Combining this result with the upper limit on D derived by Woosley et al. (2004), the conclusion is that the favored values of D are of the order of 1 km. This can be compared with the size distribution shown in fig. 3.3 (García-Senz & Bravo 2005). The distribution which arises from the present discussion would not appear flat, but rather peaked around the bubble radius $R_{\mathrm{b}} = 5 \times 10^4$ cm;

- Again because of the dispersion, the runaway is most likely reached at smaller values of R. It is not possible to deduce a precise constraint, but from the simulations it seems that the runaway is very difficult to occur at $R \geqslant 150$ km for reasonable initial values of T.

To sum up the effects of the various parameters, it turns out that the dispersion timescale is shorter with increasing R and with decreasing D. The role of temperature is more subtle,

because an increasing T shortens both $\tau_{\rm RTI}$ and, even more, $\tau_{\rm n}$. The interplay among these two phenomena sets a threshold initial temperature for the runaway increasing with R (given equal values of D).

The value of this threshold is connected to another question, left open in sect. 6.3.5. Is the numerical dispersion timescale, estimated by the simulations, comparable with the physical (not directly measurable) one? It is important to clarify this point in order to understand whether and how numerical shortcomings affect the physical description of the problem. The possible role of the turbulent background in this context has been already discussed. Other hints on this issue come from the following observations:

1. While the bubble is rising, carried by the convective flow, it experiences growing acceleration and increasingly faster dispersion, as it was shown for a sequence of simulations with increasing R. The physical dispersion timescale is thus smaller than it is inferred at fixed R.

2. During this fast motion adiabatic cooling can lengthen the nuclear timescale, making the runaway more difficult to reach.

Although the numerical dispersion prevents to fully follow the physical dispersion timescale, the above-mentioned factors can shorten the latter. Because of them, the physical timescale goes down and it could be equal to, or even slightly shorter than the numerical one, but it cannot be explored quantitatively with our computational scheme. The nuclear timescale for bubbles experiencing successful runaway is at most about 2 s. In principle, a low bubble temperature could provide a longer timescale but it is not clear if such a bubble could evolve long enough to reach the runaway without being dispersed by turbulent motions (see for example the test with $T = 7.3 \times 10^8$ K, sect. 6.4.2).

In this final discussion of the bubble physics, the importance of the background temperature must be emphasized. Together with the bubble temperature it determines the temperature contrast, thus affecting the effective gravitational acceleration. In an interesting test a simulation was done with the reference set of parameters, but with an increased background temperature (7.2×10^8 K, instead of $\sim 6.8 \times 10^8$ K). This background state, obtained by just changing the adiabatic temperature profile with a constant value of T, is not completely consistent but, because of the degeneracy of the matter, the WD structure does not depend strongly on its thermal features.

The bubble evolution in this test (fig. 6.21) had a different outcome from the standard simulation (cf. fig. 6.4). As predicted, the hotter background slows down the dispersion, and the simulation reaches the thermonuclear runaway after 1.405 s. Since a moderate increase of the background temperature has such an influence on the bubble features, this test indicates firmly how crucial the accurate WD modeling is for the ignition theory.

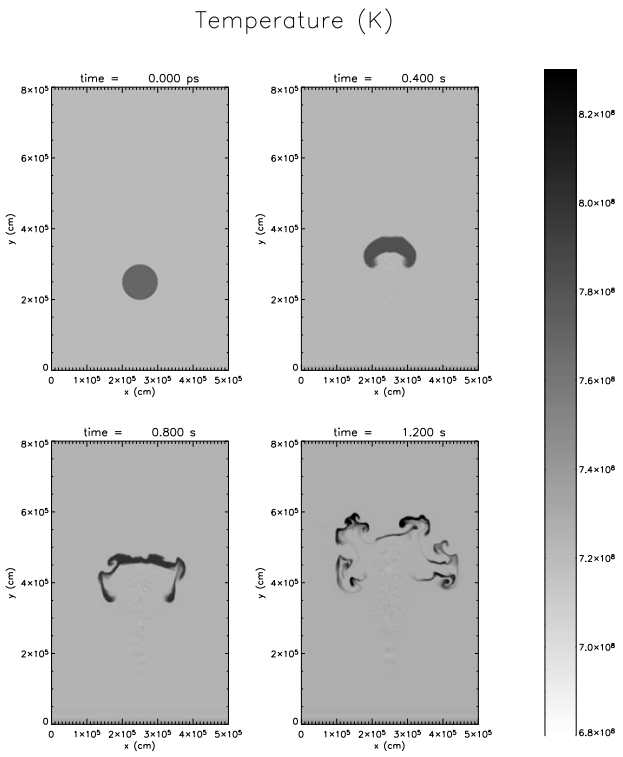

Figure 6.21.: Sequence of temperature plots, showing the evolution of a simulation with the reference set of initial parameters, but with the background temperature of 7.2×10^8 K. The gray scale is the same as in fig. 6.4 to ease the comparison. The simulation goes to thermonuclear runaway at $t = 1.405$ s.

6.5.2. Implications for the theory of ignition of SNe Ia

In the following sections, the study of the bubble physics will be profitably used as an indirect approach to the main task of this work, the problem of progenitor modeling and initial conditions in SNe Ia explosions.

Local features of the ignition process

The parameter study of the effect of the central distance of the bubble suggests that the ignition is favored at small values of R. The runaway at $R \geqslant 150$ km seems unlikely. This result refers to simulations, performed by using a WD model with a central temperature of 7×10^8 K. Analytical studies on ignition (Woosley et al. 2004, Wunsch & Woosley 2004) show that the central temperature at ignition is possibly larger, in the range $7.6 - 7.9 \times 10^8$ K. There are several hints, also in the present work, indicating that ignition is unlikely

in the considered model, and easier for a higher background temperature. The test shown in fig. 6.21 is an example. For equal bubble temperature a smaller temperature contrast to the background makes the dispersion slower.

A consequence is that the bubble ignition zone, explored by means of the parameter R, can be larger than the estimate from our parameter study (~ 100 km). A rough evaluation of the extent of this zone can be based on bubble lifetimes and convective velocities. Taking the (rather extreme) values of 2 s and 100 km s^{-1}, respectively, one finds 200 km, to be added to the extent of the energy-producing core (of the order of 100 km). This gives $R \simeq 300$ km. This central distance for ignition is very large, if compared with literature. A safer estimate of R comes from bubble lifetimes of about 1 s, according to next section, thus probably $R \simeq 200$ km, consistent with García-Senz & Woosley (1995), Woosley et al. (2004) and Wunsch & Woosley (2004).

It is clear that the adopted approach for the study of the ignition does not allow any conjecture about the departures from central symmetry of the ignition conditions. This issue has to be studied with other numerical tools. A promising way seems to be the use of 3D anelastic simulations, adopted by Kuhlen et al. (2003) in the study of convective flows in massive stars. Preliminary results of this technique, applied to SN Ia progenitors, have been presented by Woosley (2004). In any case the present work contributes to acknowledge the importance of the progenitor evolution for the initial conditions of the SN Ia explosion. The convective pattern plays a crucial role in the ignition process. The initial flame location depends mostly on the displacement of the bubbles, which are carried inside the WD by the convective motions.

The number of ignition points and the duration of the ignition process

In the presented parameter study, several values of the initial temperature have been tested without making assumptions concerning the probability distribution function (PDF) of the temperature fluctuations. Woosley et al. (2004) investigate this problem and indicate two possible PDFs, depending on details on the convective mixing in the WD core. The PDF is supposed to be either exponential or Gaussian. Without trying a choice among these two models, this section aims of inserting the results of the single-bubble evolution in a more complex background, going beyond the mere location of the ignition process, by the knowledge of the duration of the ignition phase.

This question is directly connected with the estimate of the initial number of igniting points, as is shown in Woosley et al. (2004). In their work, the e-folding time of the ignition points is found to be comparable with the time it takes during the explosion to quench the ignition by expansion (about 0.1 s). An analysis of this scenario is not directly achievable from the performed parameter study, but nonetheless some useful hints can be obtained.

Here a thought experiment of two different ignition scenarios is useful. In the first case, let a hot bubble ($T \gtrsim 7.5 \times 10^8$ K) be in the core of a WD with central temperature $T_c \simeq 7.0 \times 10^8$ K. The estimated nuclear timescale is about 2 s. If this bubble is on the "hot tail" of the temperature PDF, one can assume that the probability of generating other bubbles

with this T (or hotter) within τ_n is not large, while colder bubbles would not have time to reach the runaway temperature. In this scenario, the ignition would occur in one (or a few) igniting points. However, considering that the dispersion in more effective for bubbles of a large temperature contrast with the background, such kind of ignition scenario is likely to fail. If the explosion is not initiated, the WD goes on increasing its central temperature.

The other scenario is directly connected with the previous idea. In this second idealized setup, the WD has a larger central temperature, $T_c \gtrsim 7.5 \times 10^8$ K, and the temperature fluctuations are relatively mild with respect to the background. Under these hypotheses, the estimated τ_n of the bubbles is about 1 s, a value compatible with multi-spot ignition, as it was discussed above. Moreover, these perturbations are not supposed to be very hot with respect to the background. The probability for such bubbles to be generated, according to whatever PDF, should be large, allowing the presence of very many of them in the WD core.

Based on the presented simulations of the single bubble evolution and on the cited analytical studies on the progenitor features, from these arguments the multi-point scenario seems favored as an ignition model for the SN Ia explosion.

Self-regulation of the ignition process and diversity

As already pointed out at the end of sect. 1.7, a successful model for SNe Ia should explain both the homogeneity of the class and, hopefully as a function of one or few parameters, the range of observed diversity of the observational features (sect. 1.3). The present study demonstrates that the role of the ignition process, as sketched in the last section, goes more in the former direction.

The explanation again comes from the exam of the second scenario described above. According to the PDFs (no matter which one), there is some probability for the occurrence of one (or a few) relatively hot bubble among the the mild temperature fluctuations. In principle, it could go into runaway before the colder ones, resulting in an ignition in one or very few points. But the dispersion contributes to some self-regulation of this effect, disrupting and cooling down effectively the hottest bubbles. On this grounds, one can state that a large range of possible ignition conditions is not impossible but rather unlikely, because it is not favored by the bubble physics. Of course, this is valid *on equal convective pattern*. The diversities in the convective flow are potentially able to affect noticeably the ignition conditions, and their role in producing the observed range of diversity in SNe Ia has not yet been explored.

Comparison with existing ignition models

As far as WD central temperature, bubble temperature and radius of the ignition zone are concerned, the results inferred on the ignition process essentially are in agreement with the findings of Woosley et al. (2004) and Wunsch & Woosley (2004). The present study and the cited works have in common part of the theoretical background, but the results are based on different analyses (in our case, the physics of rising bubbles).

The interesting ignition scenario proposed by Wunsch & Woosley (2004) in the case of isotropic convective flows (ignition points in a shell around $R \approx 100\,\mathrm{km}$) could not be investigated by means of the performed parameter study. One should however notice that, because of the enhanced probability for the bubbles to go to runaway at smaller R, this initial setup may be not too different from a (somewhat partially) filled sphere.

6.6. SN Ia simulations: some outlooks and proposals

Our study supports the multi-spot ignition model. The flame seeds come from buoyant bubbles with an initial diameter of about 1 km. The proposed bubble distribution is consistent with the initial states assumed in most 3D simulation of SNe Ia explosions, the "multi-spot scenario".

On the basis of this work, the singly-ignited initial model proposed by Calder et al. (2004) and further analyzed by Plewa et al. (2004) could be interpreted as an ignition model coming from a single-bubble runaway. As discussed in sect. 6.5.2, this kind of ignition is not favored by probability arguments. Though it is not supposed to be typical, it would be interesting to further explore the outcome of such a model in order to understand whether it can still be regarded as leading to a SN Ia explosion.

In the works studying multi-point ignition, the diameter of the flame seeds (and consequently their number) is set by the spatial resolution of the simulation. In Röpke & Hillebrandt (2005b) this diameter is 7.0 km, and future 3D simulations, performed with enhanced computational resources, will allow to position smaller and smaller flame structures in the initial stage of the explosion. However, a gap has to be be filled in the ignition theory, covering the phase between the bubble evolution to the runaway and the early flame propagation. In other words, in the interval from the initiation of the runaway in a bubble, until the flame front has reached a size that the large scale simulations of explosion can catch, a small scale study is currently lacking. A similar question has been partly addressed by García-Senz & Bravo (2005).

Such a proposed test will probably open to a new problem. Will the displacement of increasingly smaller (and more numerous) spherical flame seeds in the initial conditions be a valid strategy for the future simulations? At some stage the spatial resolution will not help to improve the results anymore if it is not coupled with robust ideas of the link between the progenitor evolution and the early explosion phase. Future SN simulations should also take into account the short ($\sim 0.1\,\mathrm{s}$) temporal evolution of the ignition process, and its interplay with the ongoing explosion.

A. An alternative approach to the ignition problem and related issues

The study of an astrophysical problem by means of a multi-dimensional hydrodynamical simulation is an interesting and complex subject. Particularly challenging is the choice of a numerical tool, suited for modeling the problem under investigation. This choice involves several issues, for example the evaluation of the time to be dedicatet to a project, the exploitation of local expertise and resources, the feasibility of developing software for the the task. For this Ph.D. project, the best compromise between all these issues was to use FLASH, a well tested and modular code, in order to take advantage of the AMR and the implemented burning routine. Of course, the first question in these cases is whether a modular code, suited by definition to deal with a large range of astrophysical problems, is also appropriate for being used in a new context.

This is a typical verification problem, according to the definition of Calder et al. (2002). Even a reliable hydrocode has to be carefully tested when it is used for unexplored physical conditions to understand if it can accurately represent the physics of a model. This verification was also necessary in the study of an approach to SN Ia ignition, different from the one described in the rest of this thesis work, as it will be explained in the following.

A.1. Description and setup

Instead of studying the ignition physics by means of small-scale bubble simulations, as it was done in this thesis work, a more direct and intuitive approach is to perform a simulation of the whole WD. Actually, this has been the first approach tried in this Ph.D. project. Here it will be analyzed more from a numerical, than from a physical point of view. Indeed, the subsequent studies done for the bubble evolution have shown that this first attempt (even without the numerical problems described below) would not have been able to catch the whole complexity of the ignition process and the length scales required.

In order to follow the last convective phase of a WD, the 1D model is mapped on a 2D grid (fig. A.1). The main concern in such a mapping procedure (Zingale et al. 2002) is to guarantee the HSE of the model on times which are comparable with the convective turnover timescale ($\sim 15\,\mathrm{s}$). This stability analysis is crucial in the pre-explosive evolution.

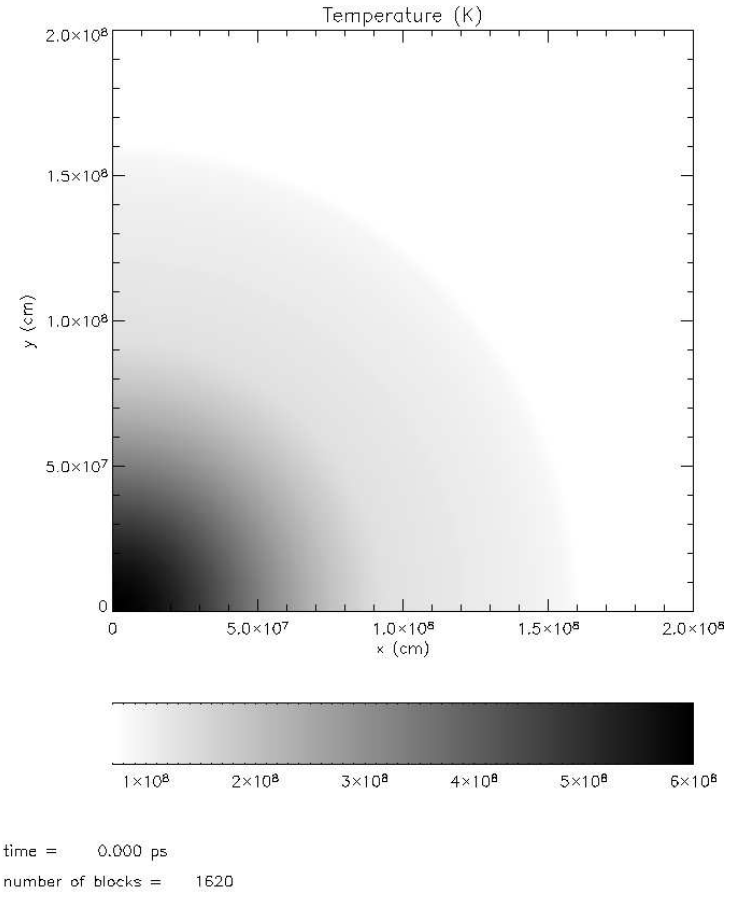

Figure A.1.: Temperature plot of the initial state of the calculations described in sect. A.1.

It would not be so important for example, in 2D and 3D simulations of SNe Ia because in that framework the WD is disrupted on much shorter timescales.

The WD model used in this test was provided by S. Woosley. It is similar to the convective 1D model described in sect. 5.2, but with a central temperature of $T_c = 6\times10^8$ K and central density $\rho_c = 2.67\times10^9\,\mathrm{g\,cm^{-3}}$. For simplifying the numerics, nuclear burning and AMR were not used. The WD was mapped on a grid with 512^2 zones with a spatial resolution $dx = 3.9\times10^5$ cm. The simulation was performed in cylindrical geometry. Only a quadrant in 2D is represented, exploiting the rotational symmetry around the y-axis and the equatorial symmetry along x. Both static gravity (read from a pre-computed function $g(R)$) and Poisson self-gravity were tested.

The WD model was processed to ensure HSE as discussed in sect. 5.3, both slighly modifying the 1D model and modifying the states of the Riemann problem. Despite of this, first 1D simulations showed the need of further reducing the spurious velocities. For this reason, before starting the real simulation for about 50 physical seconds a damping procedure was applied in order to reduce the internal velocities effectively. This procedure involved two

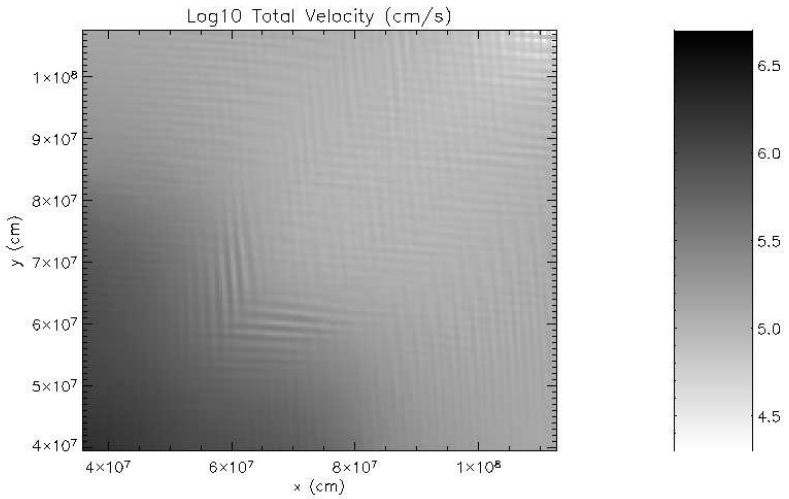

Figure A.2.: Detail of a velocity plot, showing a small part of the WD, under the conditions described in sect. A.2.

steps. The first one, described in Arnett (1994), is actually a smoothing more than a damping. It removes kinetic energy according to the 1D formula (several generalizations in 2D have been tested):

$$u_i^{\text{corrected}} = u_i - C\,(2u_i - u_{i-1} - u_{i+1})\,, \tag{A.1}$$

where the corrected velocity is calculated at the cell i and the formula involves also the uncorrected velocity values in the neighboring cells. C is a numerical parameter. In a second step the velocities are damped by a factor 0.01 and the kinetic energy is consequently modified.

A.2. The numerical problem

At the end of the damping phase, the typical velocity inside the WD is about $10^3\,\mathrm{cm\,s^{-1}}$, thus virtually the WD is stable. As soon as the damping is switched off, the velocity in the computational domain starts to increase again. When the velocity reaches about $10^7\,\mathrm{cm\,s^{-1}}$ the simulation becomes unstable, the temperature in the WD increases unphysically (note that no burning routine was implemented) and the calculation fails. This happens after about 10 physical seconds of the simulation without damping, corresponding to about 25 000 timesteps.

Several tests have shown that:

- This problem does not depend on the geometry of the simulation. A Cartesian 2D calculation (even though it is not consistent with the 3D geometry of a sphere) failed, too.

- It does not depend on resolution.
- it does not depend on the WD model. A test was performed with a fully radiative model far from thermonuclear runaway, but with the same outcome.
- It does not depend on the choice of the boundaries of the computational domain, also because the calculation does not fail in that part of the domain.
- It does not depend on the procedures for putting the model in HSE.

The properties of the velocity field inside the WD are particularly interesting (fig. A.2). The velocities have a strange, stripe-shaped pattern.

A.3. Interpretation of the problem

This test has shown that the FLASH code is not able to deal with the problem under consideration. It is not possible to keep the WD in HSE for the required timescale. There may be several reasons for this failure. The simplest one would be a bug in some part of the code which shows up only in the extreme degenerate conditions of the WD modeling. In particular, the interaction of the EOS with the rest of the code should be carefully scrutinized.

In fig. A.2 the pattern of the velocity field is parallel to the coordinate axes. It suggests that some problem in the low Mach number flows could come from the directional splitting (sec. 4.2).

A more malicious issue could be related to the Godunov scheme itself. Guillard & Murrone (2004) discuss the difficulty of this scheme in handling the low Mach number flows (such as this failed test). The problem is related to the behavior of the solutions of the Euler equations (eqs. 2.4-2.6). In general, the limit of the compressible Euler equations to low Mach numbers is not equal to the solution of the incompressible Euler equations. Given $q(\mathbf{x}, t)$ the solutions of the compressible model, it is

$$q(\mathbf{x}, t) \rightarrow q_{\text{slow}}(\mathbf{x}, t) + q_{\text{osc}}(\mathbf{x}, t/M) + \text{HOT} \tag{A.2}$$

where M is the Mach number, $q_{\text{slow}}(\mathbf{x}, t)$ is the solution of the incompressible Euler equations, $q_{\text{osc}}(\mathbf{x}, t/M)$ is an acoustic term which depends on the fast time variable t/M, and HOT are higher order terms. For special classes of initial conditions, the acoustic term is not present at leading order, and the limit to low Mach numbers holds. Unfortunately, the initial state of the Riemann state is a discontinuity and is not included in this family of "well-prepared" initial conditions. The interface pressure computed by the Riemann solver contains fluctuations of order 1 in the Mach number, even if the initial state contains fluctuations which scale as M^2.

A remedy to this drawback can come from the use of some preconditioning of the initial states, modifying the numerical fluxes in order to improve the accuracy at low M. This

technique was applied successfully to the Roe schemes (Guillard & Viozat 1999). Guillard & Murrone (2004) show that the preconditioning cures the problem also for Godunov schemes, but in this case a formal theoretical justification is currently lacking.

It remains to be understood why this numerical problem does not affect the 2D simulations of the bubble evolution, shown in the rest of this thesis. Probably, the reason has to do with the fact that in that case the HSE is not as crucial as in the failed full-star model. Moreover, in the bubble simulations gravity is acting only along the y-axis and not in the radial direction. This makes it easier for maintaining HSE.

B. Nomenclature

A list of the most often used symbols and abbreviations is given below. The standard nomenclature and units have been used in a consistent way throughout the different chapters as much as possible.

Common abbreviations and indices

$\odot$	solar
ad	adiabatic
AMR	Adaptive Mesh Refinement
c	central
eff	effective
HSE	Hydrostatic Equilibrium
PDF	Probability Distribution Function
RTI	Rayleigh-Taylor Instability
SN	Supernova
(CO) WD	(Carbon-Oxygen) White Dwarf

Greek

δ_{p}	logarithmic derivative of density with respect to temperature at constant pressure
κ	thermal conductivity
λ	length scale of a bubble piece
λ_{min}	minimum bubble size
λ_{turb}	maximum bubble size
μ	coefficient of the shear viscosity
ρ	density
τ	timescale
τ_{n}	nuclear timescale
τ_{RTI}	growth timescale of the Rayleigh-Taylor instability
ω	growth rate of a perturbation

Uppercase Latin

Simulation parameters:	
D	bubble diameter
R	distance from the WD center
T	temperature
At	Atwood number
$\mathcal{A}_{\mathrm{bubble}}$	bubble area
C_{p}	specific heat at constant pressure
G	gravitational constant
H_{p}	pressure scale height
L	integral length scale
M	mass
M_{Ch}	Chandrasekhar mass
Re	Reynolds number
$\dot{S}$	energy generation rate
$\mathbf{X}$	composition
X_i	mass fraction of a species i

Lowercase Latin

c_{s}	sound speed
dx_i	cell size along the direction i
e_{int}	specific internal energy
e_{tot}	specific total energy
$\mathbf{g}$, g	gravitational acceleration
$\mathbf{k}$, k	wavenumber
l	characteristic length scale
l_{f}	flame width
l_{g}	Gibson length scale
m_{e}	electron mass
p	pressure
$\mathbf{u}$	fluid velocity
v_{b}	bubble velocity
$\overline{v}_{\mathrm{c}}$	average convective velocity

Bibliography

Abarzhi, S. I., Glimm, J., & Lin, A. 2003, Physics of Fluids, 15, 2190 [ADS]

Arnett, W. D. 1969, AP&SS, 5, 180 [ADS]

—. 1971, ApJ, 169, 113 [ADS]

—. 1982, ApJ, 253, 785 [ADS]

—. 1994, ApJ, 427, 932 [ADS]

—. 1996, Supernovae and nucleosynthesis. an investigation of the history of matter, from the Big Bang to the present (Princeton series in astrophysics, Princeton, NJ: Princeton University Press) [ADS]

Arnett, W. D., Branch, D., & Wheeler, J. C. 1985, Nature, 314, 337 [ADS]

Arnett, W. D., Truran, J. W., & Woosley, S. E. 1971, ApJ, 165, 87 [ADS]

Baade, W. & Minkowski, R. 1954, ApJ, 119, 206 [ADS]

Baade, W. & Zwicky, F. 1934, Proceedings of the National Academy of Science, 20, 254 [ADS]

Baron, E., Lentz, E. J., & Hauschildt, P. H. 2003, ApJ, 588, L29 [ADS]

Baron, E., Nugent, P. E., Branch, D., & Hauschildt, P. H. 2004, ApJ, 616, L91 [ADS]

Bell, J. B., Day, M. S., Rendleman, C. A., Woosley, S. E., & Zingale, M. 2004a, ApJ, 606, 1029 [ADS]

—. 2004b, ApJ, 608, 883 [ADS]

Benz, W., Cameron, A. G. W., Press, W. H., & Bowers, R. L. 1990, ApJ, 348, 647 [ADS]

Blinnikov, S. & Sorokina, E. 2004, AP&SS, 290, 13 [ADS]

Branch, D. 1998, ARA&A, 36, 17 [ADS]

Branch, D., Fisher, A., & Nugent, P. 1993, AJ, 106, 2383 [ADS]

Branch, D., Romanishin, W., & Baron, E. 1996, ApJ, 465, 73 [ADS]

Bravo, E. & García-Senz, D. 1999, MNRAS, 307, 984 [ADS]

Bravo, E., Tornambé, A., Dominguez, I., & Isern, J. 1996, A&A, 306, 811 [ADS]

Bruenn, S. W. 1973, ApJ, 183, L125 [ADS]

Calder, A. C., Fryxell, B., Plewa, T., Rosner, R., Dursi, L. J., Weirs, V. G., Dupont, T., Robey, H. F., Kane, J. O., Remington, B. A., Drake, R. P., Dimonte, G., Zingale, M., Timmes, F. X., Olson, K., Ricker, P., MacNeice, P., & Tufo, H. M. 2002, ApJS, 143, 201 [ADS]

Calder, A. C., Plewa, T., Vladimirova, N., Lamb, D. Q., & Truran, J. W. 2004, astro-ph/0405162, submitted to the ApJ Lett. [ADS]

Cappellaro, E., Evans, R., & Turatto, M. 1999, A&A, 351, 459 [ADS]

Chandrasekhar, S. 1957, An introduction to the study of stellar structure. ([New York] Dover Publications) [ADS]

—. 1961, Hydrodynamic and hydromagnetic stability (International Series of Monographs on Physics, Oxford: Clarendon) [ADS]

Chorin, A. J. & Marsden, J. E. 1979, A mathematical introduction to fluid mechnanics (Universitext, New York: Springer) [ADS]

Clayton, D. D. 1983, Principles of stellar evolution and nucleosynthesis (Chicago: University of Chicago Press, 1983) [ADS]

Colella, P. & Woodward, P. 1984, J. Comp. Phys., 54, 174 [LINK]

Colgate, S. A. & McKee, C. 1969, ApJ, 157, 623 [ADS]

Contardo, G., Leibundgut, B., & Vacca, W. D. 2000, A&A, 359, 876 [ADS]

Couch, R. G. & Arnett, W. D. 1975, ApJ, 196, 791 [ADS]

Cussons, R., Langanke, K., & Liolios, T. 2002, European Physical Journal A, 15, 291 [ADS]

Damköhler, G. 1939, Jahrb. Deut. Luftfahrtforsch., 113

Davies, R. M. & Taylor, G. I. 1950, Proc. R. Soc. London A, 200, 375

Della Valle, M. & Livio, M. 1994, ApJ, 423, L31 [ADS]

Eswaran, V. & Pope, S. B. 1988, Physics of Fluids, 31, 506 [ADS]

Filippenko, A. V. 1997a, ARA&A, 35, 309 [ADS]

Filippenko, A. V. 1997b, in NATO ASIC Proc. 486: Thermonuclear Supernovae, 1 [ADS]

Fryxell, B., Müller, E., & Arnett, D. 1989, Hydrodynamics and Nuclear Burning. MPA Rep. 449; Garching: MPA

Fryxell, B., Olson, K., Ricker, P., Timmes, F. X., Zingale, M., Lamb, D. Q., MacNeice, P., Rosner, R., Truran, J. W., & Tufo, H. 2000, ApJS, 131, 273 [ADS]

Gamezo, V. N., Khokhlov, A. M., & Oran, E. S. 2004, Phys. Rev. Lett., 92, 211102 [ADS]

Gamezo, V. N., Khokhlov, A. M., Oran, E. S., Chtchelkanova, A. Y., & Rosenberg, R. O. 2003, Science, 299, 77 [ADS]

Gamow, G. & Schoenberg, M. 1941, Physical Review, 59, 539 [ADS]

García-Senz, D. & Bravo, E. 2005, A&A, 430, 585 [ADS]

García-Senz, D. & Woosley, S. E. 1995, ApJ, 454, 895 [ADS]

Garnavich, P. M., Jha, S., Challis, P., Clocchiatti, A., Diercks, A., Filippenko, A. V., Gilliland, R. L., Hogan, C. J., Kirshner, R. P., Leibundgut, B., Phillips, M. M., Reiss, D., Riess, A. G., Schmidt, B. P., Schommer, R. A., Smith, R. C., Spyromilio, J., Stubbs, C., Suntzeff, N. B., Tonry, J., & Carroll, S. M. 1998, ApJ, 509, 74 [ADS]

Ghirlanda, G., Ghisellini, G., Lazzati, D., & Firmani, C. 2004, ApJ, 613, L13 [ADS]

Gibson, B. K., Stetson, P. B., Freedman, W. L., Mould, J. R., Kennicutt, R. C., Huchra, J. P., Sakai, S., Graham, J. A., Fassett, C. I., Kelson, D. D., Ferrarese, L., Hughes, S. M. G., Illingworth, G. D., Macri, L. M., Madore, B. F., Sebo, K. M., & Silbermann, N. A. 2000, ApJ, 529, 723 [ADS]

Glimm, J. & Li, X. L. 1988, Physics of Fluids, 31, 2077 [ADS]

Godunov, S. K. 1959, Matematicheskii Sbornik, 47, 271

Goncharov, V. N. 2002, Physical Review Letters, 88, 134502 [ADS]

Goriely, S., José, J., Hernanz, M., Rayet, M., & Arnould, M. 2002, A&A, 383, L27 [ADS]

Guillard, H. & Murrone, A. 2004, Computers & Fluids, 33, 655 [LINK]

Guillard, H. & Viozat, C. 1999, Computers & Fluids, 28, 63 [LINK]

Gutierrez, J., Garcia-Berro, E., Iben, I. J., Isern, J., Labay, J., & Canal, R. 1996, ApJ, 459, 701 [ADS]

Hachisu, I. & Kato, M. 2003, ApJ, 590, 445 [ADS]

Han, Z. & Podsiadlowski, P. 2004, MNRAS, 350, 1301 [ADS]

Hansen, C. J. & Kawaler, S. D. 1994, Stellar Interiors. Physical Principles, Structure, and Evolution. (Springer-Verlag Berlin Heidelberg New York. Also Astronomy and Astrophysics Library) [ADS]

Hartwig, E. 1885, Astronomische Nachrichten, 112, 355 [ADS]

Hillebrandt, W. & Niemeyer, J. C. 2000, ARA&A, 38, 191 [ADS]

Höflich, P. 2004, astro-ph/0409170, in: Supernovae as Cosmological Lighthouses Padua, June 16 - 19, 2004, eds. Turatto et al., ASP Conference Series [ADS]

Höflich, P. & Khokhlov, A. 1996, ApJ, 457, 500 [ADS]

Höflich, P. & Stein, J. 2002, ApJ, 568, 779 [ADS]

Howell, D. A., Höflich, P., Wang, L., & Wheeler, J. C. 2001, ApJ, 556, 302 [ADS]

Hoyle, F. & Fowler, W. A. 1960, ApJ, 132, 565 [ADS]

Iben, I. 1982, ApJ, 259, 244 [ADS]

Iben, I. & Tutukov, A. V. 1984, ApJS, 54, 335 [ADS]

—. 1985, ApJS, 58, 661 [ADS]

Itoh, N., Hayashi, H., Nishikawa, A., & Kohyama, Y. 1996, ApJS, 102, 411 [ADS]

Itoh, N., Tomizawa, N., Wanajo, S., & Nozawa, S. 2003, ApJ, 586, 1436 [ADS]

Iwamoto, K., Brachwitz, F., Nomoto, K., Kishimoto, N., Umeda, H., Hix, W. R., & Thielemann, F. 1999, ApJS, 125, 439 [ADS]

Kadanoff, L. P. 2001, Phys. Today, 54, 34 [ADS]

Kahabka, P. & van den Heuvel, E. P. J. 1997, ARA&A, 35, 69 [ADS]

Kasen, D., Nugent, P., Wang, L., Howell, D. A., Wheeler, J. C., Höflich, P., Baade, D., Baron, E., & Hauschildt, P. H. 2003, ApJ, 593, 788 [ADS]

Kasen, D. & Plewa, T. 2005, ApJ, 622, L41 [ADS]

Khokhlov, A. M. 1991a, A&A, 245, L25 [ADS]

—. 1991b, A&A, 246, 383 [ADS]

—. 1993, ApJ, 419, L77 [ADS]

—. 2000, astro-ph/0008463 [ADS]

Kippenhahn, R. & Weigert, A. 1994, Stellar Structure and Evolution (Springer-Verlag Berlin Heidelberg New York. Also Astronomy and Astrophysics Library) [ADS]

Kozma, C., Fransson, C., Hillebrandt, W., Travaglio, C., Sollerman, J., Reinecke, M., Röpke, F. K., & Spyromilio, J. 2005, astro-ph/0504317, submitted to A&A[ADS]

Kuhlen, M., Woosley, W. E., & Glatzmaier, G. A. 2003, in ASP Conf. Ser. 293: 3D Stellar Evolution, 147 [ADS]

Landau, L. D. & Lifshitz, E. M. 1995, Fluid mechanics (Course of theoretical physics, Oxford: Pergamon Press) [ADS]

Layzer, D. 1955, ApJ, 122, 1 [ADS]

Leibundgut, B. 1998, in Supernovae and cosmology (Astronomisches Institut, Universität Basel, ed. L. Labhardt, B. Binggeli and R. Buser), 61 [ADS]

Leibundgut, B. 2000, A&AR, 10, 179 [ADS]

—. 2001, ARA&A, 39, 67 [ADS]

Lesaffre, P., Podsiadlowski, P., & Tout, C. A. 2005, MNRAS, 356, 131 [ADS]

LeVeque, R. J. 1998, in Saas-Fee Advanced Course 27: Computational Methods for Astrophysical Fluid Flow, 1 [ADS]

Li, X. L. 1996, Phys. Fluids, 8, 336 [ADS]

Livio, M. 2000, in Type Ia Supernovae, Theory and Cosmology. Edited by J. C. Niemeyer and J. W. Truran. Published by Cambridge University Press, 33 [ADS]

Livne, E. 1993, ApJ, 406, L17 [ADS]

Livne, E. & Arnett, D. 1995, ApJ, 452, 62 [ADS]

Lundmark, K. 1920, Svenska Vetenkapsakad. Handl., 60, 8

MacNeice, P., Olson, K. M., Mobarry, C., de Fainchtein, R., & Packer, C. 1999, NASA Tech. Rep. CR-1999-209483

Mannucci, F., Della Valle, M., Panagia, N., Cappellaro, E., Cresci, G., Maiolino, R., Petrosian, A., & Turatto, M. 2005, A&A, 433, 807 [ADS]

Minkowski, R. 1940, PASP, 52, 206 [ADS]

Mitton, S. 1978, The Crab Nebula (New York : Scribner, 1979, c1978. 1st U.S. ed.) [ADS]

Mochkovitch, R. 1996, A&A, 311, 152 [ADS]

Napiwotzki, R., Yungelson, L., Nelemans, G., Marsh, T. R., Leibundgut, B., Renzini, R., Homeier, D., Koester, D., Moehler, S., Christlieb, N., Reimers, D., Drechsel, H., Heber, U., Karl, C., & Pauli, E.-M. 2004, in Astronomical Society of the Pacific Conference Series, 402–410 [ADS]

Niemeyer, J. C. 1999, ApJ, 523, L57 [ADS]

Niemeyer, J. C. & Hillebrandt, W. 1995, ApJ, 452, 769 [ADS]

Niemeyer, J. C., Hillebrandt, W., & Woosley, S. E. 1996, ApJ, 471, 903 [ADS]

Nomoto, K. 1980, Space Science Reviews, 27, 563 [ADS]

—. 1982, ApJ, 253, 798 [ADS]

Nomoto, K. & Iben, I. 1985, ApJ, 297, 531 [ADS]

Nomoto, K. & Kondo, Y. 1991, ApJ, 367, L19 [ADS]

Nomoto, K. & Sugimoto, D. 1977, PASJ, 29, 765 [ADS]

Nomoto, K., Sugimoto, D., & Neo, S. 1976, AP&SS, 39, L37 [ADS]

Nomoto, K., Thielemann, F.-K., & Yokoi, K. 1984, ApJ, 286, 644 [ADS]

Norman, M. L. 2004, astro-ph/0402230, in "Adaptive Mesh Refinement - Theory and Applications", Eds. T. Plewa, T. Linde & V. G. Weirs, Springer Lecture Notes in Computational Science and Engineering, 41, 2004 [ADS]

Ogata, S., Iyetomi, H., & Ichimaru, S. 1991, ApJ, 372, 259 [ADS]

Oppenheimer, J. R. & Volkoff, G. M. 1939, Physical Review, 55, 374 [ADS]

Osher, S. & Sethian, J. A. 1988, J. Comp. Phys., 79, 12 [LINK]

Paczyński, B. 1972, Astroph. Letters, 11, 53 [ADS]

Padmanabhan, T. 2000, Theoretical astrophysics. Vol.1: Astrophysical processes (Cambridge University Press) [ADS]

—. 2001, Theoretical Astrophysics, Volume 2: Stars and Stellar Systems (Cambridge University Press) [ADS]

Pauldrach, A. W. A., Duschinger, M., Mazzali, P. A., Puls, J., Lennon, M., & Miller, D. L. 1996, A&A, 312, 525 [ADS]

Perlmutter, S., Aldering, G., Goldhaber, G., Knop, R. A., Nugent, P., Castro, P. G., Deustua, S., Fabbro, S., Goobar, A., Groom, D. E., Hook, I. M., Kim, A. G., Kim, M. Y., Lee, J. C., Nunes, N. J., Pain, R., Pennypacker, C. R., Quimby, R., Lidman, C., Ellis, R. S., Irwin, M., McMahon, R. G., Ruiz-Lapuente, P., Walton, N., Schaefer, B., Boyle, B. J., Filippenko, A. V., Matheson, T., Fruchter, A. S., Panagia, N., Newberg, H. J. M., & Couch, W. J. 1999, ApJ, 517, 565 [ADS]

Peters, N. 1999, Journal of Fluid Mechanics, 384, 107 [ADS]

Phillips, M. M. 1993, ApJ, 413, L105 [ADS]

Piersanti, L., Gagliardi, S., Iben, I. J., & Tornambé, A. 2003, ApJ, 598, 1229 [ADS]

Plewa, T., Calder, A. C., & Lamb, D. Q. 2004, ApJ, 612, L37 [ADS]

Popper, D. M. 1937, PASP, 49, 283 [ADS]

Pskovskii, I. P. 1977, Soviet Astronomy, 21, 675 [ADS]

Rasio, F. A. & Shapiro, S. L. 1995, ApJ, 438, 887 [ADS]

Read, K. I. 1984, Physica D, 12, 45 [ADS]

Reinecke, M., Hillebrandt, W., & Niemeyer, J. C. 1999, A&A, 347, 739 [ADS]

—. 2002a, A&A, 386, 936 [ADS]

—. 2002b, A&A, 391, 1167 [ADS]

Reinecke, M., Hillebrandt, W., Niemeyer, J. C., Klein, R., & Gröbl, A. 1999, A&A, 347, 724 [ADS]

Riess, A. G., Filippenko, A. V., Challis, P., Clocchiatti, A., Diercks, A., Garnavich, P. M., Gilliland, R. L., Hogan, C. J., Jha, S., Kirshner, R. P., Leibundgut, B., Phillips, M. M., Reiss, D., Schmidt, B. P., Schommer, R. A., Smith, R. C., Spyromilio, J., Stubbs, C., Suntzeff, N. B., & Tonry, J. 1998, AJ, 116, 1009 [ADS]

Riess, A. G., Filippenko, A. V., Li, W., Treffers, R. R., Schmidt, B. P., Qiu, Y., Hu, J., Armstrong, M., Faranda, C., Thouvenot, E., & Buil, C. 1999, AJ, 118, 2675 [ADS]

Robinson, K., Dursi, L. J., Ricker, P. M., Rosner, R., Calder, A. C., Zingale, M., Truran, J. W., Linde, T., Caceres, A., Fryxell, B., Olson, K., Riley, K., Siegel, A., & Vladimirova, N. 2004, ApJ, 601, 621 [ADS]

Röpke, F. K. 2005, A&A, 432, 969 [ADS]

Röpke, F. K. & Hillebrandt, W. 2004, A&A, 420, L1 [ADS]

—. 2005a, A&A, 429, L29 [ADS]

—. 2005b, A&A, 431, 635 [ADS]

Röpke, F. K., Hillebrandt, W., & Niemeyer, J. C. 2004a, A&A, 420, 411 [ADS]

—. 2004b, A&A, 421, 783 [ADS]

Ruiz-Lapuente, P. 2004, AP&SS, 290, 43 [ADS]

Ruiz-Lapuente, P., Canal, R., & Burkert, A. 1997, in NATO ASIC Proc. 486: Thermonuclear Supernovae, 205 [ADS]

Ruiz-Lapuente, P., Comeron, F., Méndez, J., Canal, R., Smartt, S. J., Filippenko, A. V., Kurucz, R. L., Chornock, R., Foley, R. J., Stanishev, V., & Ibata, R. 2004, Nature, 431, 1069 [ADS]

Saha, A., Sandage, A., Tammann, G. A., Labhardt, L., Macchetto, F. D., & Panagia, N. 1999, ApJ, 522, 802 [ADS]

Schmidt, W., Hillebrandt, W., & Niemeyer, J. C. 2004, astro-ph/0406083, submitted to J. Fluid Mech. [ADS]

Sharp, D. H. 1984, Physica D, 12, 3 [ADS]

Smiljanovski, V., Moser, V., & Klein, R. 1997, Combustion Theory and Modelling, 1, 183 [LINK]

Smith, D. 2004, Notes on the Rayleigh-Taylor instability; available on the Web at `http://grad32.as.utexas.edu/~dave/rayleigh-taylor-notes.pdf` [LINK]

Stein, J., Barkat, Z., & Wheeler, J. C. 1999, ApJ, 523, 381 [ADS]

Stephenson, F. R. & Clark, D. H. 1976, Scientific American, 234, 100 [ADS]

Stephenson, F. R. & Green, D. A. 2002, Historical supernovae and their remnants, by F. Richard Stephenson and David A. Green. International series in astronomy and astrophysics, vol. 5. Oxford: Clarendon Press [ADS]

Sussman, M., Smereka, P., & Osher, S. 1994, J. Comp. Phys., 114, 146 [LINK]

Taylor, G. 1950, Proc. R. Soc. London Ser. A, 201, 192

Thielemann, F.-K., Nomoto, K., & Yokoi, K. 1986, A&A, 158, 17 [ADS]

Thorstensen, J. R., Fesen, R. A., & van den Bergh, S. 2001, AJ, 122, 297 [ADS]

Timmes, F. X. 1999, ApJS, 124, 241 [ADS]

Timmes, F. X., Hoffman, R. D., & Woosley, S. E. 2000, ApJS, 129, 377 [ADS]

Timmes, F. X. & Swesty, F. D. 2000, ApJS, 126, 501 [ADS]

Timmes, F. X. & Woosley, S. E. 1992, ApJ, 396, 649 [ADS]

Travaglio, C., Hillebrandt, W., Reinecke, M., & Thielemann, F.-K. 2004, A&A, 425, 1029 [ADS]

Truran, J. W., Arnett, W. D., & Cameron, A. G. W. 1967, Canadian Journal of Physics, 45, 2315 [ADS]

Turatto, M. 2003, Lecture Notes in Physics, Berlin Springer Verlag, 598, 21 [ADS]

Turatto, M., Cappellaro, E., & Benetti, S. 1994, AJ, 108, 202 [ADS]

Umeda, H., Nomoto, K., Yamaoka, H., & Wanajo, S. 1999, ApJ, 513, 861 [ADS]

van den Bergh, S. 1990, PASP, 102, 1318 [ADS]

Wagoner, R. V. 1969, ApJS, 18, 247 [ADS]

Wallace, R. K., Woosley, S. E., & Weaver, T. A. 1982, ApJ, 258, 696 [ADS]

Wang, L., Baade, D., Höflich, P., Khokhlov, A., Wheeler, J. C., Kasen, D., Nugent, P. E., Perlmutter, S., Fransson, C., & Lundqvist, P. 2003, ApJ, 591, 1110 [ADS]

Wang, L., Wheeler, J. C., & Hoeflich, P. 1997, ApJ, 476, L27 [ADS]

Webbink, R. F. 1984, ApJ, 277, 355 [ADS]

Wilson, J. R. & Mayle, R. W. 1988, Phys. Reports, 163, 63 [ADS]

Winget, D. E., Sullivan, D. J., Metcalfe, T. S., Kawaler, S. D., & Montgomery, M. H. 2004, ApJ, 602, L109 [ADS]

Woodward, P. & Colella, P. 1984, J. Comp. Phys., 54, 115 [LINK]

Woosley, S. E. 1990, in Supernovae, XIII, ed. A. G. Petschek (Springer-Verlag Berlin Heidelberg New York. Also Astronomy and Astrophysics Library), 182–210 [ADS]

Woosley, S. E. 2001, Nucl. Phys. A, 688, 9 [ADS]

—. 2004, talk presented at the 12^{th} Workshop on "Nuclear Astrophysics", Ringberg Castle near Tegernsee, Germany, March 22 - 27, 2004; available on the Web at `http://www.mpa-garching.mpg.de/hydro/NucAstro/PDF/woosley.pdf` [LINK]

Woosley, S. E. & Eastman, R. G. 1997, in NATO ASIC Proc. 486: Thermonuclear Supernovae, 821 [ADS]

Woosley, S. E. & Weaver, T. A. 1986, ARA&A, 24, 205 [ADS]

Woosley, S. E. & Weaver, T. A. 1994a, in Supernovae, NATO Advanced Science Institutes (ASI) Series C: Mathematical and Physical Sciences, Proceedings of the 54th Ecole d'ete de physique theorique, session LIV, held in Les Houches, Haute-Savoie, France 31 July-1 September 1990, Amsterdam, New York: North-Holland, edited by Bludman, S. A.; Mochkovitch, R.; Zinn-Justin, J., 63 [ADS]

—. 1994b, ApJ, 423, 371 [ADS]

Woosley, S. E., Wunsch, S., & Kuhlen, M. 2004, ApJ, 607, 921 [ADS]

Wunsch, S. & Woosley, S. E. 2004, ApJ, 616, 1102 [ADS]

Yoon, S.-C. & Langer, N. 2003, A&A, 412, L53 [ADS]

—. 2004, A&A, 419, 623 [ADS]

—. 2005, A&A, 435, 967 [ADS]

Yoon, S.-C., Langer, N., & Scheithauer, S. 2004, A&A, 425, 217 [ADS]

Zingale, M., Dursi, L. J., ZuHone, J., Calder, A. C., Fryxell, B., Plewa, T., Truran, J. W., Caceres, A., Olson, K. amd Ricker, P. M., Riley, K., Rosner, R., Siegel, A., Timmes, F. X., & Vladimirova, N. 2002, ApJS, 143, 539 [ADS]

Zwicky, F. 1938, ApJ, 88, 522 [ADS]

Zwicky, F. 1965, Supernovae (Stellar Structure - Stars and Stellar Systems: Compendium of Astronomy and Astrophysics, Vol. VIII, edited by Lawrence H. Aller and Dean B. McLaughlin. University of Chicago Press), 367–424 [ADS]

Zwicky, F., Berger, J., Gates, H. S., & Rudnicki, K. 1963, PASP, 75, 236 [ADS]

Acknowledgements

Working at MPA during the past three years has had a great influence on much of my life, both academically and personally. First of all, I want to thank Wolfgang Hillebrandt who proposed to me this Ph.D. project: *grazie* for your enlightening guidance and, even more, because I have learned from you an effective and open-minded way to approach scientific research.

An important contribution to this work was given by Marcus Brüggen (International University Bremen). *Grazie* for your (often daily) patient help, and for sharing with me your expertise on FLASH.

This research project has been carried out within the framework of the European Research Training Network (RTN) on *The Physics of Type Ia Supernova Explosions*. This active and efficient collaboration between several European science institutions gave me the opportunity to have a thorough viewpoint on the many problems associated with SNe Ia, both on theoretical and observational issues. The meetings of the RTN gave me the chance to have many interesting discussions, especially with the Oxford-Cambridge node (Philipp Podsiadlowski, Christopher Tout and Pierre Lesaffre). The results of this thesis were first presented and discussed, with useful improvements, at the RTN meeting in Cambridge during December 2004.

Both my research activities and general scientific background profited much from my stay at the MPA, in a fruitful environment which encourages interactions between scientists of different interests. I am very grateful to the present and past members of the MPA's Hydrodynamics group, in particular Fritz Röpke, Martin Reinecke, Wolfram Schmidt and Jens Niemeyer. Thank you all for the instructive discussions on the physics of SNe Ia and for your assistance in solving many technical issues with my simulations.

In my work with the FLASH code, I have had useful interactions with the people at the ASC / Alliances Center for Astrophysical Thermonuclear Flashes in Chicago: special thanks to Tomek Plewa for helpful suggestions with regards to theoretical and numerical problems. During May 2004, I attended a FLASH workshop where I met and received invaluable help from many members of the FLASH Center, thank you all.

Finally, I want to acknowledge Jim Truran for interesting discussions. Special thanks to Stan Woosley for providing the 1D models of the white dwarf used in this study, and for helpful explanations on ignition physics.